Applications of Synchrotron-Based X-ray Microprobes

Paul M. Bertsch* and Douglas B. Hunter

Advanced Analytical Center for Environmental Sciences, Savannah River Ecology Laboratory, The University of Georgia, Drawer E, Aiken, South Carolina 29802

Received September 20, 2000

Contents

I. Introduction

The past decade has witnessed significant advances in technologies related to X-ray spectroscopic techniques, both as a result of advances in X-ray optics, focusing devices, and detectors and because of greater availability of high-brilliance synchrotron facilities worldwide. The result is that synchrotron-based X-ray absorption fine structure spectroscopy (XAFS) has become a mainstream technique in a number of scientific disciplines and is providing molecular-level information not previously available using other techniques. The XAFS spectrum is typically separated into the X-ray absorption near-edge structure (XANES), also known as the near-edge extended X-ray absorption fine structure (NEXAFS) region, and the extended X-ray absorption fine structure (EXAFS) region. The XANES or NEXAFS spectrum is represented by the energy region just below to ∼50 eV above the absorption edge and serves as a site-specific probe of local charge state, coordination, and magnetic moment of the central absorber. Above this energy, the extended fine structure, characteristic of an EXAFS spectrum, is manifested as oscillations in the absorption cross section arising from constructive and destructive interference of the outgoing photoelectric wave and the incoming photoelectric wave

* To whom correspondence should be addressed. Phone: (803) 725-5637. Fax: (803) 725-3309. E-mail: bertsch@srel.edu.

Paul M. Bertsch is a Professor of Soil Physical Chemistry and Mineralogy and Director of the Savannah River Ecology Laboratory of The University of Georgia. His research is focused on delineating the molecular form of contaminants (chemical speciation) in complex environmental samples and relating this to transportability and bioavailability. He is a participating research team member of the X-26A, microprobe beamline at the National Synchrotron Light Source, and a design team member of Sector 13, the Geo/Soil/Enviro CARS Collaborative Access Team, at the Advanced Photon Source. He served as Vice Chair of the Board of Governors of the Consortium for Advance Radiation Sources at the University of Chicago from 1994−1999.

Douglas B. Hunter received a B.S. degree in Chemical Physics in 1985 from the University of Toronto and his M.S. and Ph.D. degrees in Botany from the Unversity of Vermont in 1987 and 1991, respectively. He worked at the Savannah River Ecology Laboratory of The University of Georgia developing new spectroscopic applications in the environmental sciences, where much of his time was devoted to developing applications of synchrotron-based X-ray techniques at the National Synchrotron Light Source and Advanced Photon Source. He is currently a Principal Scientist at the Savannah River Technology Center.

10.1021/cr990070s CCC: $36.00
Published on Web 06/13/2001

backscattered from neighboring atoms. The EXAFS spectrum provides information on the number, identity, and distance (±0.02 Å) of neighboring atoms. The ability to probe matter to determine the chemical state of a system at high spatial resolution with high elemental sensitivity has been important to a number of fields, including the earth and environmental sciences, biosciences, colloid and surface science, and materials science, among others. The need for such data at high spatial resolution is a result of the heterogeneous nature of samples commonly examined in these disciplines and the importance of understanding how elemental and molecular distributions influence heterogeneous chemical reactivity or, conversely, how chemical reactivity influences heterogeneous elemental and molecular distributions. Traditional spectroscopic measurements of complex samples provide volume-averaged data that obscures important spatially variable chemical information. The ability to probe homogeneous or less heterogeneous domains within complex samples at high spatial resolution with minimal sample preparation provides an opportunity for more detailed molecular-level characterization.

While there exists a variety of microanalytical techniques that have long been used in these disciplines, synchrotron-based spatially resolved X-ray fluorescence spectroscopy (SXRF) and XAFS spectroscopy are emerging as important methods that complement characterization by traditional techniques as well as by other emerging methods, such as spatially resolved luminescence, FTIR, and Raman spectroscopy. The reasons for this are the elemental specificity, low detection limits, nondestructive nature of the measurement, the ability, in many instances, to examine samples in situ, and the ability to extract information on valence states and on specific bonding environments or molecular forms of target elements in complex matrixes. In this review we define in situ measurements as measurements made under ambient conditions (298 K and 1 atm) and in the presence of water.

X-ray fluorescence (XRF) has been long used as a technique for determining elemental concentrations in a variety of matrixes.[1−18] Synchrotron-based XRF (SXRF) techniques have decreased the detection limits by several orders of magnitude over conventional XRF techniques, in the 50−100 ng g^{-1} range for many elements at third-generation synchrotron facilities.[16,18,19] Additionally, the enhanced brilliance of modern synchrotron facilities and advances in focusing optics allow for spatial resolution in the 0.5−1 μm range for hard X-rays (>3 keV) and ~50 nm for soft X-rays (<1 keV). Spatially resolved SXRF imaging has become a critical complimentary technique that is a prerequisite for conducting spatially resolved XAFS spectroscopy for samples with heterogeneous distributions of target elements. Because spatially resolved SXRF is a relatively rapid method, it can be used to efficiently examine complex samples to determine if there are heterogeneous elemental distributions on a spatial scale that are resolvable by the technique. Generation of elemental distribution maps can then be used to identify localized regions of target elements with rather straightforward determination of their concentrations.[2,5,20] Mineral phase associations and chemical speciation of target elements can also be inferred based on elemental associations elucidated in elemental maps.[21] Recent advances in the simulation of X-ray fluorescence spectra have greatly improved the predictability of photon−matter interactions for high-energy, linearly polarized monochromatic and polychromatic radiation typically available at modern synchrotron facilities.[19,22−25] These advances in data analyses, along with specific consideration of particle topology, are greatly enhancing instrument calibration, allowing for optimization of detection geometry for specific samples and, therefore, improving quantitative analysis of complex samples.[26−28] On the basis of elemental distribution data generated by SXRF, spatially resolved XAFS experiments can be efficiently devised. XAFS spectroscopic interrogation of regions with elevated localized concentrations of target elements can then be conducted to extract information on valence states, symmetry, electronic states, and the identity, number, as well as bond lengths of neighboring atoms. Often the bulk concentrations of target elements within a sample are well below the detection limits of conventional XRF and XAFS spectroscopic techniques. If the element is localized within the sample, however, the concentration within the localized volume can be many orders of magnitude greater than the bulk concentration, and this is often coupled to a decreased background as a result of lower than average concentrations of other common heavier elements, such as Fe, in the localized volume element. Thus, localization of elements in complex samples and the ability to analyze the localized volume often results in concentrations that are well within the detection limits of a synchrotron-based X-ray microprobe. Also, the ability to probe discrete domains containing a target element in a complex mosaic often limits the population of coordination environments, thus simplifying the XAFS data and facilitating data analysis for complex natural or synthetic composite samples having spatially variable composition. In much the same way, soft X-ray microscopy, which utilizes spectral features indicative of molecular structure of the dominant absorbing atoms for contrast, is often coupled with spatially resolved XANES to derive detailed information on elemental and molecular distributions in complex media.[29]

There are a number of advantages of micro-SXRF over other commonly employed microprobe techniques.[4,5,10,17,30] While electron microprobe techniques offer outstanding spatial resolution, they suffer from relatively poor sensitivity (especially for transition and heavier elements), require a UHV environment, and can result in appreciably greater beam damage to the sample. Likewise, particle-induced X-ray emission (PIXE), although achieving comparable spatial resolution with SXRF, is not as sensitive for heavier elements and can impart beam damage to the sample.

Advantages of SXRF over the more widely employed electron microprobe techniques include superior detection limits for (sub μg g^{-1}) most elements,

especially $Z \geq 20$, the ability to analyze nonconducting materials in situ and without coating, and the nondestructive nature of the measurement. The benefits are even more dramatic for XAFS spectroscopy compared to electron energy loss spectroscopy (EELS) since valence states, which are of primary concern in most investigations, can be influenced within the electron beam and because the energy dose required for radiation damage induced by electrons is an order of magnitude or more lower than for X-rays. Several comprehensive reviews that discuss the advantages and disadvantages of various microanalytical techniques have been published in recent years.[10,13,14,17,18,30,31]

This review will focus on the complementary spatially resolved SXRF imaging and XAFS spectroscopic techniques as well as X-ray microscopy and spectromicroscopy for examining elemental and molecular distributions and molecular forms of elements in complex samples. While there have been substantial advances in laboratory-based X-ray instruments over the past decade,[30,32−38] our review will focus on synchrotron-based spatially resolved XRF and XAFS methods and on X-ray microscopy and spectromicroscopy, which have witnessed enormous advances and offer the greatest potential for characterizing the most demanding samples. It is useful at this point to introduce some terminology regarding various synchrotron-based X-ray sources for those not familiar with these large multiuser facilities. The *first-generation* synchrotron facilities were originally constructed as particle accelerators for the high-energy physics community to conduct experiments on the fundamental properties of matter. Soon after the commissioning of these large first-generation particle accelerators, it was realized that large quantities of electromagnetic radiation, including X-rays, were produced. The production of this radiation results from the process of steering the particles, which are traveling near the speed of light, in a nearly circular orbit within the storage ring where the particles are decelerated upon interaction with the bending magnets occupying the arched sections of the storage ring.[21,39] This secondary electromagnetic radiation (synchrotron radiation), having a very broad energy range (<1 eV to 100 keV) and a brightness ($\sim 10^{14}$ photons s^{-1} 0.1% bandwidth^{-1} mrad^{-2}) 10^5-10^6 times greater than conventional laboratory sources available at the time, was soon recognized to be an outstanding source for X-ray-based techniques. Shortly thereafter, synchrotron facilities were designed and constructed specifically for the purpose of providing intense X-ray sources for experimentalists, and these are referred to as *second-generation* synchrotron facilities.[21,39] Soon after the commissioning of the second-generation synchrotron facilities, it was discovered that special magnetic devices could be inserted into the straight sections of the storage rings to produce X-rays having a brightness up to 10^{18} photons s^{-1} (0.1% band width)$^{-1}$ mrad^{-2}! Thus, the *third-generation* synchrotron facilities have been built and commissioned in recent years to take advantage of emerging technologies utilizing superconducting insertion devices. The third-generation sources, in addition to having unprecedented brightness, display remarkable brilliance, which is defined as the brightness per source area, i.e., photons s^{-1} (0.1% band width)$^{-1}$ mrad^{-2} mm^{-2}. It is this tremendous increase in brilliance that has ushered in a new era for X-ray microprobes, since it is the source area or the area in space defined by the trajectory of the particle beam that defines the dimensions of the focal spot on the sample when using X-ray focusing optics.

Note that many investigators refer to synchrotron-based spatially resolved X-ray microprobe methods as micro-SXRF and micro-XAFS spectroscopy. While soft X-ray microprobes at synchrotron facilities worldwide have routinely achieved submicrometer to nanometer spatial resolution for many years, it is only recently that ca. micrometer to submicrometer spatial resolution has become routine for hard X-rays. Thus, many hard X-ray 'microprobes' have traditionally been limited to a spatial resolution between 2 and 50 μm or even 100 to several hundred μm for XAFS analysis. While we prefer the more generic terms spatially resolved XRF and XAFS spectroscopy for this reason, we will adopt the more widely accepted terms micro-SXRF and micro-XAFS in this review, recognizing that not all applications strictly meet this criteria. The distinction between microspectroscopy and spectromicroscopy should be defined as well. In the former, a spectrum is collected with a microbeam for a specific volume element or region of interest defined by an optical, phase, or chemical contrast image or on an elemental map generated via SXRF spectroscopy. Whereas for the latter, full spectra or diagnostic features at specific energies are collected at each pixel and then used to generate an image based on spatially variable chemical differences in the sample.

In this review we will briefly describe generic beamline configurations and experimental strategies for conducting spatially resolved SXRF and XAFS spectroscopy, soft X-ray microscopy, and spectromicroscopy as well as the advantages and disadvantages to the various approaches. Finally, we will describe applications of these techniques to a variety of fields, including earth and environmental sciences, biosciences, and materials sciences, where heterogeneous elemental or molecular distributions and chemical speciation are common important features and where there has been a significant increase in the utilization of spatially resolved SXRF and X-ray imaging along with microspectroscopy and spectromicroscopy over the past decade.

II. Experimental Configuration and Strategies for X-ray Microscopy, Micro-SXRF Imaging, Micro-XAFS, and Spectromicroscopy

The experimental strategies for conducting X-ray microscopy, micro-SXRF, and micro-XAFS spectroscopy are all similar in many respects. A sample is typically mounted on a motorized stage equipped with stepping motors and piezoelectric positioners and then translated in the x and y directions through the beam path. Most X-ray microprobe beamlines also have visible or electron microscope imaging

capabilities, so that interesting features on a sample can be easily identified and interrogated by micro-SXRF, micro-XAFS, or by X-ray microscopy. Elemental concentrations or chemically specific information is then collected at each pixel to generate elemental distribution maps, micro-XAFS, or spectromicroscopic images using a variety of contrast mechanisms, including those based on electronic structure, molecular structure, and magnetic circular dichroism (MCD).[40,41] Detection of coherently scattered X-rays has also been used in X-ray microscopy to generate dark-field images of samples labeled with colloidal gold to provide much higher contrast of small features.[42]

Differences in configuration and hardware of X-ray microprobes and X-ray microscopes are typically between beamlines operating in the hard and soft X-ray energy regimes, since at lower energies there are a number of challenges related to the nature of the sample and to detecting emitted electrons or transmitted or fluorescence X-rays, particularly when it is important to have the sample remain in a hydrated state. The purpose of the following discussion is to introduce the generic components of hard and soft X-ray beamlines and to introduce experimental strategies as well as the challenges involved in examining complex samples using these techniques.

A. Colliminating X-rays for Microprobes and Microscopes

Since the wavelength range of X-rays is on the order of 10^3-10^4 smaller than visible light, much finer spatial resolution is achievable as a result of the limits imposed by effects of diffraction associated with optical imaging. Although scientists appreciated this early after the discovery of X-rays in 1895 by Rontgen, the advent of X-ray microspectroscopy has only seen significant growth over the past two decades. The two major developments driving this are the high brilliance of second- and third-generation synchrotron X-ray sources and the revolution in X-ray optics that has been ongoing since the 1980s. As discussed previously, the source brilliance ultimately determines the intensity of a X-ray microprobe. In this discussion, we will briefly introduce the primary strategies and optics used in X-ray microprobes at synchrotron facilities. We direct interested readers to comprehensive treatments of the design, development, and application of focusing devices for X-ray microprobes and microscopes at synchrotron facilities worldwide.[2,4,30,32−35,38,42−93]

The earliest approach to producing a small X-ray beam for use in X-ray microprobes at synchrotron facilities was to simply collimate the beam with a slit or pinhole assembly, albeit there were a number of reports where focusing optics were employed, yet not routinely.[59] This approach provides ~5 μm lateral resolution for white light SXRF elemental detection and imaging applications, but generally it does not provide sufficient flux for most applications requiring micro-XAFS spectroscopic analysis, especially in the extended X-ray absorption fine structure (EXAFS) region of the spectrum. One of the first X-ray microprobes employed a fixed primary beam defining aperture followed by a focusing mirror and then a four-jaw adjustable secondary aperture, used either alone or in combination with a laser-drilled pinhole assembly located in close proximity to the sample. The challenge of this approach is optimal alignment of the beam to project the central most intense and most highly polarized portion of the synchrotron radiation profile on the sample. An alternate approach that has not found widespread utility is to insert a focusing optical element beyond the pinhole to refocus the diverging beam. These designs successfully produce X-ray beams in the 2−10 μm range.[59] At second-generation synchrotron X-ray sources, there is enough flux using slit or pinhole collimation to generate elemental maps with polychromatic X-rays by SXRF; however, micro-XAFS analysis employing slit and pinhole collimation and monochromatic light is severely limited at low elemental concentrations. The ability to focus X-rays to generate the necessary flux for monochromatic micro-XAFS analysis started in the 1980s and became more common on microprobe beamlines in the 1990s.

In recent years, advances in X-ray optics have provided the capabilities for focusing hard X-rays to near micrometer spot sizes and soft X-rays to ~50 nm, with sufficient flux for conducting micro-XAFS spectroscopy. When examining the literature on X-ray microprobes, it is important to separate theoretical capabilities, achievable resolution, and routine operation using various strategies for producing small X-ray beams. While a number of techniques for focusing hard and soft X-rays were demonstrated to be feasible over a decade ago, it is only in the past five years that hard X-ray microprobes using advanced focusing optics have become *routinely* operational. An outstanding historical review of the development of techniques for generating X-ray microbeams has recently been published.[59] The refractive index of most materials for X-rays is very close to unity, making refractive optics an ineffective strategy for focusing X-rays. Thus, interference devices such as crystals, reflection from smooth surfaces, multilayers, and zone plates are typically employed to focus X-rays. Recent comprehensive reviews cover the details of the various X-ray focusing optics,[10,59,94] and it is not our intention to repeat this information here. We will only briefly outline approaches more commonly used to focus X-rays for X-ray microprobes and discuss their capabilities, such as the current achievable spatial resolution, band width, and working distance.

Various types of both reflection and diffraction X-ray focusing devices have been developed and successfully deployed at second- and third-generation synchrotron facilities worldwide.[59,87,94] Grazing incidence mirrors in various configurations and geometries, Bragg reflection from natural crystals and multilayer mirrors, capillary optics, Fresnel lenses, and Bragg−Fresnel optical devices have all been used to focus X-rays, and the advantages and disadvantages of these various reflective and diffractive optics have been outlined in detail.[94] In the soft X-ray range,

the diffractive zone plate optics have demonstrated remarkable spatial resolution (~20 nm) and versatility because of the energy range available and the relatively long working distances (~10 cm).[94−97] Zone plates have primarily been used in soft X-ray applications, particularly in the "water window" 240−540 eV between O and C K edges. More recently, Fresnel zone plates have also been used for focusing hard X-rays and spot sizes as small as 0.5 μm have been achieved at the APS.[98−100] The major disadvantage of zone plates is that they are chromatic, which means that the focal length varies with energy. This provides significant challenges for their use in XAFS spectroscopy, particularly in the EXAFS region, since the zone plate has to be synchronously translated along with the monochromator to maintain focus on a given spot (vide infra).

The reflection optics that have been most widely deployed on microprobe beamlines worldwide include bent crystals, grazing incidence (including multilayer) mirrors in various geometries including Schwarzschild, Kirkpatrick−Baez (K−B), and Wolter.[30,78,79,87,94,101−105] Many of these reflective focusing devices have been successfully deployed routinely at synchrotron facilities and have achieved submicrometer spatial resolution. There are important considerations for specific applications. For example, while multilayer mirrors have provided outstanding spatial resolution in the hard X-ray range (≤0.5 μm), they operate over a limited band width and, thus, are not suitable for XAFS spectroscopic investigations. Double-elliptical mirrors in the Kirkpatrick−Baez (K−B) geometry[87,106−108] continue to emerge as being among the most versatile focusing optics for routine operation of hard X-ray microprobes where spatially resolved XRF, XAFS, and diffraction experiments are all desireable.[59,94] The advantage of the K−B focusing device is the outstanding spatial resolution (1−10 μm at second-generation sources and submicrometer at third-generation sources),[87,94,106,108] the large working distance (~10 cm), and the large energy range over which it operates (white light). Additionally, the double-elliptical K−B mirror focusing device is achromatic, meaning that the focal length is independent of energy, which is important in terms of spatially resolved XAFS spectroscopy. Another area of active research for focusing hard X-rays are Bragg−Fresnel reflection optical devices. The lower energy cut off associated with Fresnel zone plates imparted both by the limits of currently achievable aspect ratios and the penetration of X-rays into the zone plate can be circumvented by employing the zone plates in reflection rather than the transmission mode. These Bragg−Fresnel lenses that are currently being developed on third-generation synchrotron sources have achieved a focal spot of ~0.5 μm.[67,94,109,110] Currently, both circular and elliptical Bragg−Fresnel lenses work over a narrow range of X-ray energies, although research on linear Bragg−Fresnel lenses is ongoing where the incident angle can be scanned with X-ray energy. There is still the problem of the focal length changing with energy in this geometry. Other developments include placing two linear Bragg−Fresnel lenses placed in K−B geometry, which can potentially focus to a spot.[111,112]

Capillary optics are another strategy for focusing X-rays that has received much attention.[10,59,64,94,113] Capillary optical devices utilize total internal reflection for focusing X-rays. The major advantage of tapered glass capillaries over X-ray optics based on diffraction is their ability to concentrate wide-band polychromatic as well as monochromatic X-rays. However, capillaries are nonimaging devices which can yield the highest intensity spots from low-divergence beams from synchrotron radiation sources. Capillaries have an additional advantage in that the size of the concentrated beam is not dependent on the coherence of the X-rays as it is with zone plates. Outstanding spatial resolution (0.05 μm) has been reported utilizing capillary optics at synchrotron facilities.[10,52,59,64,94,113,114] The major disadvantage is that multiple reflections inside the capillary tube leads to large divergence of the X-rays as they exit the capillary, necessitating that the sample be placed within 10−100 beam diameters of the capillary, meaning that the working distance is typically <100 μm. Such short working distances provide challenges in working with irregular samples as well as in conducting XAFS experiments where it may be difficult to measure the incident intensity (I_o) between the exit of the capillary and the sample. This can be potentially circumvented by using the single-reflection focusing mode, which permits much greater working distances. To date, such systems have not yet achieved submicrometer resolution. A very comprehensive discussion and comparison of capabilities of coherent X-ray optics for hard X-ray sources has recently appeared.[115]

B. X-ray Microscopy and Spectromicroscopy in the Soft X-ray Regime

Soft X-rays are typically operationally defined has having energies greater than ca. 100 eV to ca. 1−2 keV. Many reviews of soft X-ray microscopes at synchrotron facilities worldwide have recently appeared.[26,32,40,41,43−45,47,50,51,57,60,65,68,70−74,79,89,91,96,97,116−121] Attenuation of soft X-rays in air and water becomes an increasing problem with decreasing energy, with the penetration distance in air being only 0.4−4 mm. This dictates that samples be investigated under dry or semi-dry (less than 2 μm thick water film) conditions, typically in a He atmosphere or under vacuum. Placing the sample in a He environment increases the effective penetration distance to 20−100 mm.[96]

Soft X-rays in the energy range between the C and O K edges (284.2 and 543.1 eV) have a typical absorption length in water of 2−10 μm, since less than ~540 eV water is almost an order of magnitude less absorbing than organic compounds. This energy range is termed the "water window", and working within this window permits the investigation of hydrated, intact, unstained biological or organic specimens (vide infra) since C is highly absorbing in this energy range while O is not. For studies in the biological and environmental sciences, where it is often desirable or a requirement that samples be

examined in a hydrated state, samples are typically mounted between thin (100−140 nm thick) silicon nitride windows and bathed in a stream of He gas to minimize absorption by air.[117,122] A new specimen chamber for examining hydrated samples, suspensions, and liquids by scanning transmission X-ray microscopy (STXM) has recently been reported.[122] The cell, which allows for rapid sample loading, is sealed by O-rings and has been shown to maintain stable hydration for up to 8 h. It was demonstrated to be useful for imaging and for conducting micro-XANES at the C K edge at a ∼100 nm spatial resolution.

The earliest soft X-ray microscopes at synchrotron facilities primarily used detection of secondary electrons with standard electrostatic optics to generate images, akin to a photoelectron emission microscope (PEEM) with an ultraviolet excitation source.[44,65,79] In this case, intensity variations in the resulting images are due to a combination of chemical effects and topology. The advantages of using a synchrotron radiation source are that the higher photon energies allow valence bands and core levels to be probed and that a sample can be examined as a function of incident energy. Thus, more recent soft X-ray microscopes have exploited this capability to use chemical contrast for imaging as well as for conducting micro-XAFS and spectromicroscopy.[44] The synchrotron-based version of the more conventional PEEM is often referred to as X-ray PEEM (XPEEM) or as an X-ray secondary electron microscope (XSEM). The primary kinds of core-level spectroscopy typically conducted with soft X-ray microscopes have been X-ray photoemission spectroscopy (XPS) and XAFS spectroscopy. XPS is an extremely surface-sensitive technique probing only ∼1 nm into the surface and, thus, is applicable to the examination of pristine surfaces or for providing information on surface contaminants.[123] XAFS spectroscopy can either be a "near-surface" sensitive technique (∼10 nm) when using electron yield (EY) detection or a bulk technique (∼100 nm) when fluorescence or transmission detection is employed.[123] In the case of fluorescence detection, special sample preparation is not required, whereas XAFS spectroscopy in the soft X-ray energy range using transmission detection requires specially prepared ultrathin sections (≤100−200 nm). Both XPS and XAFS spectroscopy with EY detection typically require a vacuum environment, whereas XAFS spectroscopy employing the fluorescence or transmission mode of detection can be conducted on partially or fully hydrated samples. Figure 1 summarizes the typical spatial and energy resolution achieved with synchrotron-based soft X-ray spectromicroscopes relative to related techniques.

Most soft X-ray microscopes have one of the same general layouts shown schematically in Figure 2. As mentioned previously, a monochromator placed in the path of the synchrotron radiation permits scanning over a broad X-ray energy range. Almost all soft X-ray spectromicroscopes utilize zone plate optical elements to focus the beam on the sample. The sample can be positioned and translated through the beam in 2-D using a stage device with coarse me-

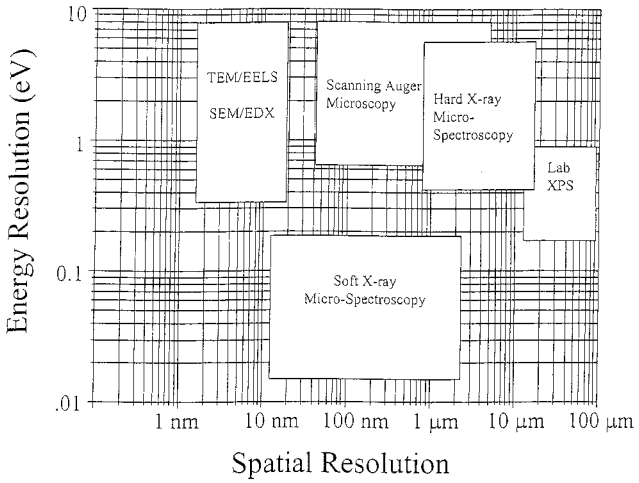

Figure 1. Spatial and spectral resolution regimes for synchrotron-generated soft and hard X-rays compared to some related techniques. (Adapted from ref 123. Copyright 1999 John Wiley & Sons.)

chanical stepping motors for 0.1 μm to millimeter positioning combined with piezoelectric positioners for fine motion control (1−100 nm movement) to generate an image.[118] If the sample thickness is known, elemental determination can be inferred by differential absorption. Element-specific imaging can also be performed by collecting data at monochromator settings above and below the absorption edge energy of an element of interest.

Since soft X-rays are commonly focused with chromatic (i.e., energy dependent focal length) zone plate optical elements, there are a number of challenges related to conducting spectroscopy. The zone plate lens must be translated longitudinally along with the monochromator to maintain a focused beam on the sample. In absorption spectroscopy, where the monochromator is scanned at one location on the sample, instrument wobble limits the effective spatial resolution and typically the zone plate is defocused to prevent radiation damage to the sample. Since many samples of biological and environmental interest have high carbon content, the issue of radiation damage to the sample is of concern.[96] Another challenge is the short working distance that is characteristic of high-resolution zone plates, typically several hundred micrometers. While spatial resolution on the order of 30−50 nm has been reported under ideal conditions, a spatial resolution of 100−300 nm is typically achieved without exceptional alignment or vibration isolation difficulties.

Modes of detection are dependent on the imaging or spectroscopic technique employed. XPEEM typically uses electron optics to focus photoelectrons as a function of energy onto a microchannel plate to amplify the signal. Subsequent visualization of the electrons is generated with a phosphor YAG screen and CCD camera.[41] XPS is a photoemission method that typically relies on multichannel detection with a hemispherical sector analyzer (HSA). X-ray detection (fluorescence and transmission) is typically made by photodiodes, CCD detectors, or gas proportional counters (Figure 2).

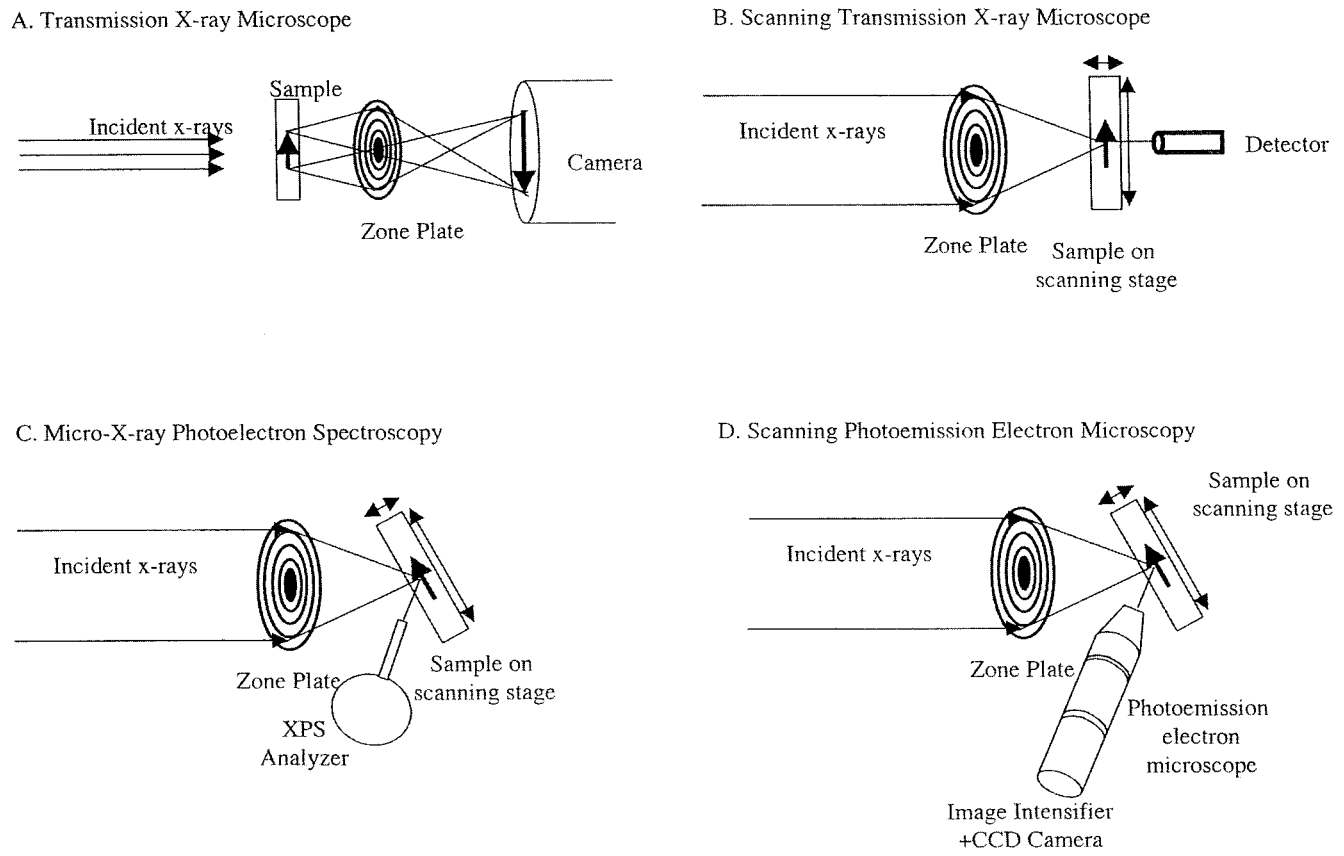

Figure 2. Schematic of soft X-ray spectromicroscopy arrangements utilizing zone plates.

C. Hard X-ray Regime

Higher energy X-rays probe deeper into samples with fewer problems associated with attenuation of fluorescence X-rays in the air path. A schematic of the dedicated hard X-ray microprobe bending magnet beamline, X-26A at the NSLS, is depicted in Figure 4 and can serve as a generic example of a hard X-ray microprobe. Similarly configured hard X-ray microprobes are operating at second- and third-generation synchrotron facilities worldwide.[1,2,4,5,9,30,53−56,66,67,75,81,94,100,105,106,124−130] Hard X-ray microprobes utilizing white light (continuum) provide the ability to conduct rapid nondestructive trace element microanalysis on a wide range of samples with little sample preparation. Detection limits for elements $Z > 20$ by SXRF at many second-generation synchrotron sources is in the low μg g^{-1} to high ng g^{-1} range with a factor of 10 improvement being realized at third-generation sources. Spatial resolution for SXRF analysis using hard X-ray microprobes at second-generation sources is typically in the $\sim$10 μm range with an order of magnitude improvement becoming more routine at third-generation sources. Furthermore, monoenergetic X-rays produced by a monochromator placed in the beam path allow for micro-XAFS to also be conducted on diverse samples.

As the X-ray energy increases, the achievable energy and spatial resolution decrease (Figure 3). This poses less stringent requirements for the sample atmosphere, air path length, sample translation stage, sample thickness, and moisture content compared to soft X-ray microprobes. The configuration of hard X-ray microprobes is conceptually similar to soft X-ray microscopes: a primary aperture is generally followed by a monochromator for energy tuning and then by focusing optics. While a number of focusing optics are used to create microbeams on hard X-ray microprobes, the double-elliptical Kirkpatrick−Baez (K−B) focusing mirrors remain the most popular and versatile.[94] In contrast to zone plates, K−B mirror systems are achromatic, meaning that the beam position is independent of incident energy. Additionally, K−B mirrors operate over a very broad energy range, provide a relatively large working distance between the mirror assembly and the sample, and reject higher energy harmonics, an important feature for micro-XAFS applications. Capillary optical elements have also been employed as focusing devices on a number of hard X-ray microprobes.[6,10,64,94,100,114] As discussed previously, while capillary microfocusing devices provide outstanding spatial resolution over a wide energy range, they present challenges related to very short working distances required between the exit of the optical element and the sample. Furthermore, while several hard X-ray microprobes successfully utilize capillary optics for SXRF analysis, the challenges related to conducting micro-XAFS with capillaries have yet to be surmounted.

Samples are typically mounted on a mechanical stage outfitted with computer-controlled microstepping motors that translate the sample in the *x*/*y* directions for sample positioning. Depending on the sample composition and X-ray energy, penetration of X-rays can be micrometers to millimeters and fluo-

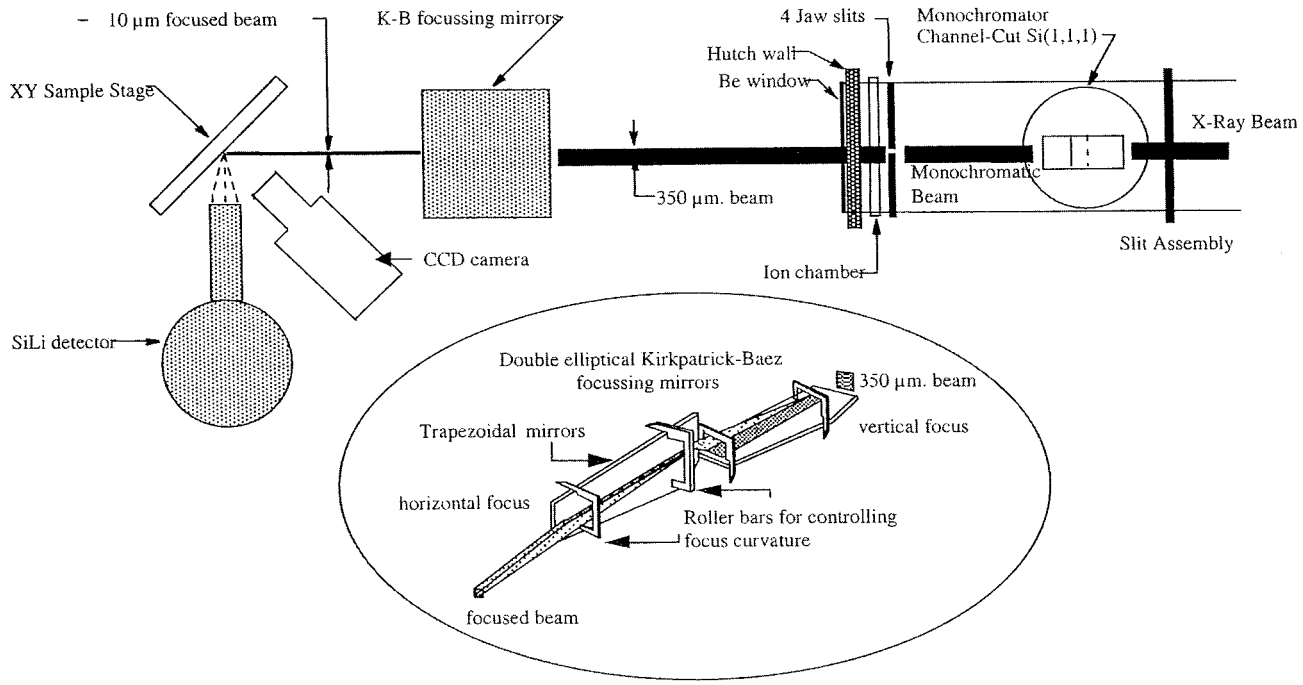

Figure 3. Schematic of hard X-ray microprobe.

rescence X-rays are detected from a depth of a few to hundreds of micrometers. Thus, in addition to lateral resolution, variation of samples in the third dimension must be considered when examining thick samples. Typical microprobe geometries have the sample canted 45° to the incident beam, allowing the sample to be visualized with an optical microscope fitted with a long working distance objective positioned at the focal point of the focusing optical element. The microscope is also outfitted with a TV attachment, and the whole apparatus is mounted normal to the sample stage to view the sample surface. To minimize background from Compton scattering, X-ray detectors are typically placed in the plane of the storage ring and at 90° to the incident beam.

There are a number of detectors that are typically utilized for hard X-ray microprobes, including energy-dispersive detectors (including multielement solid-state detectors) and wavelength-dispersive spectrometers. Wavelength-dispersive spectrometers afford greater energy resolution (~10 eV) at the cost of time and sensitivity. Energy-dispersive detectors, such as Si(Li) or intrinsic Ge detectors, provide rapid full spectral determination with low background but at lower energy resolution (~150 eV). Elemental distribution maps of samples are usually generated by collecting the total counts in individual peaks in spectra at each pixel as a sample is translated through the beam path. Following the generation of the elemental maps, areas of localized elemental concentrations of interest can then be examined by micro-XAFS spectroscopy. As with soft X-ray spectromicroscopy, distinctive features in an XAFS spectrum can be used to provide chemical state imaging. An application using phase contrast imaging, where collimated monochromatic hard X-ray radiation was passed through a sample onto a scintillation screen imaged by a video camera and microscope objective to produce a visible image with 5 μm resolution, has also recently been reported.[100]

Little has been published pertaining to experimental difficulties of conducting micro-XAFS spectroscopy. Most micro-XAFS spectroscopy is measured in fluorescence mode, and as focused beam sizes as well as sample thicknesses move below 1 μm, difficulties of self-absorption become unimportant. However, if the sample size is greater than about 10 μm in thickness and the concentration of the target element is high, then self-absorption effects within the volume excited by the incident X-rays can become an issue for XANES and EXAFS measurements. Although self-absorption has been effectively minimized by using small exit-angle conditions and by numerical correction,[48] it remains a major consideration for micro-EXAFS spectroscopy of relatively thick samples or samples with relatively high concentrations of the target element. An additional challenge relates to the third dimension of a sample, i.e., sample depth, particularly when working in the hard X-ray regime. Thus, even when achieving a specific lateral resolution, the sample thickness and features buried in the sample must be considered when interpreting 2-D elemental or chemical state maps generated by X-ray microprobes.

Another challenge for micro-EXAFS analysis is in small deviations of the beam position. If the region of analysis and chemical heterogeneity on the sample is of the same spatial scale as the probe beam, then small deviations in beam position on the sample can dramatically effect the EXAFS measurements. The primary reason for this is that the EXAFS signal is typically less than 1% of the total signal. A simple calculation for a 10 μm beam, assuming a Guassian beam profile, indicates that drift in the beam position on the order of 150 nm is sufficient to account for a 1% change in the signal intensity, thus effecting the EXAFS measurements. Such dimensions are on the

order of thermal expansion/contraction even with subtle temperature variations and also as a result poor vibration isolation. One strategy to circumvent this problem is to ensure that the measured area is homogeneous on a scale larger than the probe beam size along with the spread introduced by thermal expansion/contraction and vibration-induced movement (probe area). This requires preliminary intensive micro-SXRF and micro-XAFS mapping in the vicinity of important features on a sample to ensure that spatial homogeneity is larger than the probe area.

Sample thickness effects can also influence micro-XAFS measurements in the transmission mode. Once again, the sample ideally should have homogeneous thickness relative to the size of the probe area. This is not necessarily trivial. If the sample is comprised of individual grains or particles, they should ideally be 2 orders of magnitude smaller than the probe area such as to minimize packing irregularities to less than the EXAFS signal. Since mechanical grinding can typically only produce grains about 10 μm in size, micro-XAFS in the transmission mode is limited to samples that are comprised of grains or particles in the 10−100 nm size range.

III. Applications of Synchrotron-Based Micro-SXRF, Micro-XAFS, and Spectromicroscopy

Applications of spatially resolved SXRF and XAFS spectroscopy and spectromicroscopy to complex natural and synthesized materials has witnessed tremendous growth over the past decade, mirroring technical advances in X-ray focusing optics, detectors, and processing capabilities as well as the availability of extremely brilliant third-generation synchrotron X-ray sources. Many of the applications published in the period from 1990 to1994 were primarily incorporated in papers largely focused on technical aspects related to the construction and commissioning of X-ray microprobes and X-ray absorption microscopes worldwide. Although many papers with applications appearing since that time have also been more focused on the technology related to spatially resolved X-ray microscopy and spectromicroscopy, recent publications have been centered on specific applications, demonstrating that the techniques are maturing and becoming more widely available to the scientific community. Arguably, there have been few advances in analytical and spectroscopic instrumentation that have catalyzed interactions across traditional disciplinary boundaries as have synchrotron-based X-ray techniques. For example, it is becoming increasingly routine to have teams of scientists comprised of individuals from several disciplines, including physics, chemistry and materials science, biosciences and medicine, geology, earth and environmental sciences, and agricultural sciences. While there are some differences related to the scientific questions being addressed and/or the nature of the materials being examined, the experimental challenges are often quite similar as are the type of data required.

It is clear that over the next decade scientists in all of these disciplines will be able to exploit the tremendous advances in synchrotron X-ray beamline technologies and facilities to address problems that were, until recently, considered intractable. For example, in the earth and environmental sciences, information generated by synchrotron-based X-ray techniques over the past several years is contributing significantly to redefining paradigms of abiotic- and biotic-mediated redox and phase transformation reactions (chemical speciation transformations).

In the following discussion we will review studies that require spatially resolved SXRF and XAFS spectroscopy and spectromicroscopy to address questions related to the spatial heterogeneity of elemental and molecular distributions and their chemical state in a variety of complex samples. We have organized the discussion according to more traditional disciplinary themes, even though there are obvious similarities and significant overlap in many of the applications in terms of the type of information extracted. While we have attempted to make the review as comprehensive as possible, our expertise is in the earth and environmental sciences and this bias is undoubtedly evident. Many of the applications in the earth and environmental sciences deal with complex natural materials characterization, surface-controlled reactions, and interrogating biological samples, all of which are directly applicable to the applications in the disciplines. Furthermore, many of the more novel applications in materials and biosciences that are emerging typically involve soft X-ray microscopes. Development of soft X-ray microscopes for examining samples in situ has involved significant technical challenges that are still being optimized.[92]

A. Earth and Environmental Sciences

1. Geochemistry and Cosmochemistry

Trace element concentrations, partitioning between phases, and distributions in rock-forming minerals and mineral assemblages and in ore bodies provide important information required to understand the conditions under which they formed or were transformed. In addition, trace element distributions and zonation patterns provide important clues regarding the source and travel path of mineralizing fluids, while the geochemistry of fluid inclusions provides direct information on the mineralizing fluids, which serve as records of paleo-hydrothermal processes.[13,131−147] Similarly, elemental distributions and zonation patterns in meteorites, micrometeorites, and interplanetary dust particles (IDPs) also reveal important clues concerning their sources and age as well as insights into the processes occurring at the earliest stages of the solar system.[5,8,141,148−159] Spatially resolved SXRF has emerged as the method of choice for the determination of trace element concentrations in micrometeorites for many years because of the analytical sensitivity and also because the measurement is nondestructive which is critical for examining quantity-limited samples.[8] For the past decade, spatially resolved SXRF analyses of various rock and mineral samples, fluid inclusions, and meteorites have complemented information collected by EMPA and PIXE to probe elemental distribution patterns to infer reaction histories, chemical equilibrium

among and between mineral and vapor phases, kinetically controlled crystal growth patterns, and surface structural controls on trace element incorporation patterns. In fact, geoscientists at The University of Chicago, Chicago, IL, working with physicists from Brookhaven National Lab, Upton, NY, were largely responsible for the commissioning and operation of X-26A at the National Synchrotron Light Source (NSLS), the first dedicated SXRF beamline at a hard X-ray synchrotron facility,[2,4,5,8,124,131] and many of the early reports of SXRF and micro-XAFS at other synchrotron facilities were conducted on geological samples.[160,161] A series of studies examining trace element distribution patterns in calcites,[142] apatites,[136,144] and silicates[137] by spatially resolved SXRF has provided evidence for a surface chemical control on trace element incorporation during crystallization. Differential incorporation of trace elements between structurally distinct growth steps along nonequivalent crystal faces suggests the importance of nonequilibrium processes controlling trace element incorporation that may also have significant implications for sorption/desorption reactions.

A very important recent development that is greatly expanding applications to geochemistry and cosmochemistry is the ability to combine SXRF elemental distribution data with spatially resolved XAFS spectroscopy to extract chemical information on heterogeneously distributed trace elements in minerals, mineral inclusions, and meteorites. Since the pioneering studies demonstrating the feasibility of conducting XAFS spectroscopy in regions less than 20 μm in diameter,[48,160] important applications have appeared in the literature.[5,126,143,162−167] Valence states of transition metals in minerals and inclusions can provide important information on the oxidation−reduction state and homogeneity in source rocks, and prior to the availability of spatially resolved XAFS, there existed no other techniques for unambiguously determining valence states of heterogeneously distributed trace elements in minerals. Sutton et al.[162] determined the valence states of Cr in 200 μm regions within olivine and pyroxene grains from lunar basalt. Using the energies and magnitudes of preedge features, the edge position, and the main peak in the XANES spectra, Cr in 0, II, III, IV, and VI valence states could be differentiated. The main features identified in the Cr K-edge XANES derivative spectra were preedge peaks associated with the 1s → 3d and 1s → 4s electron transitions, a peak associated with the energy at half-maximum, and a peak associated with the edge crest. Both of the preedge features associated with localized electronic transitions are forbidden, suggesting that coordination symmetry imparts allowed character resulting from orbital mixing. As demonstrated previously for bulk mineral phases,[162] energies of the four main features demonstrated a general monotonic increase with oxidation state for a series of Cr-containing phases with known valence states. This relationship was then used to infer valence states of Cr in silicates of the lunar basalt. The results demonstrated that Cr in olivine grains within the basalt was primarily divalent, whereas Cr in pyroxene grains was primarily trivalent, implying that the parent magma was highly reduced, being dominated by Cr(II) at the time of crystallization.

A similar approach has been used to determine Fe valence states in a variety of iron-bearing minerals where the energy shift in the preedge feature, also representing a 1s → 3d electron transition, is exploited[5,126,163,164,166−168] to determine Fe(III)/Fe_{Total} and, thus, ferric/ferrous ratios. For well characterized standard materials and homogeneous phases, the XANES method compares well with Mossbauer spectroscopic and wet chemical analyses. The advantage of the spatially resolved XANES method is the ability to examine Fe(II)/F(III) ratios related to localized redox-controlled compositional zoning in minerals. In one such study, variations of Fe valence states in an olivine were examined at a 10 μm scale, where it was demonstrated that the mineral was comprised of an oxidized rim surrounding a reduced core, suggesting postcrystallization oxidation or a change in prevailing redox conditions during crystal growth.[167] The redox status of olivine inclusions in diamonds from the Earth's upper mantle was examined by spatially resolved Cr K-edge XANES spectroscopy.[5] The results indicate that Cr exists in a range of valence states depending on the source of the different diamonds, suggesting the existence of different redox conditions in diamond-forming regions within the Earth.

Spatially resolved SXRF and Zn K-edge XAFS measurements on fluid inclusions in quartz have recently been collected in regions as small as 12 μm using the dedicated hard X-ray microprobe at beamline X-26A at the National Synchrotron Light Source (NSLS).[143,165,169] The initial studies employed an 8:1 Pt-coated Al ellipsoidal focusing mirror with slit collimation downstream of the mirror to define a ~50 μm beam. Elemental distribution maps generated with SXRF at ~12 μm using a pinhole collimator revealed localized regions of Zn in the inclusion fluid and that Zn is not an important component of daughter crystals present[165] (Figure 4). Analysis of the EXAFS data generated at 25 °C suggests that $ZnCl_4^{2-}$ is the dominant complex in the inclusion fluids even though micro-SXRF revealed the presence of Br^- (Figures 4 and 5). A more recent study examined Zn coordination environments within similar inclusions over a temperature range of 25 to 430 °C.[169] The mean Zn−Cl bond distance was determined to be 2.31 ± 0.01 Å at 25 °C and is found to decrease linearly with temperature to 2.26 ± 0.02 Å at 430 °C even though the XAFS data analysis suggests that the tetrachloro Zn complex dominates over the entire temperature range. This observation is in contrast to calculated Zn speciation that predicts a preponderance of the dichloro Zn complex at higher temperatures. The explanation given for this discrepancy is that the most reliable thermodynamic data available was generated at much lower temperatures and Cl^- concentrations than present in the fluid inclusions. Furthermore, the authors propose a mechanism for the observed decrease Zn−Cl bond length with temperature based on decreased dielectric con-

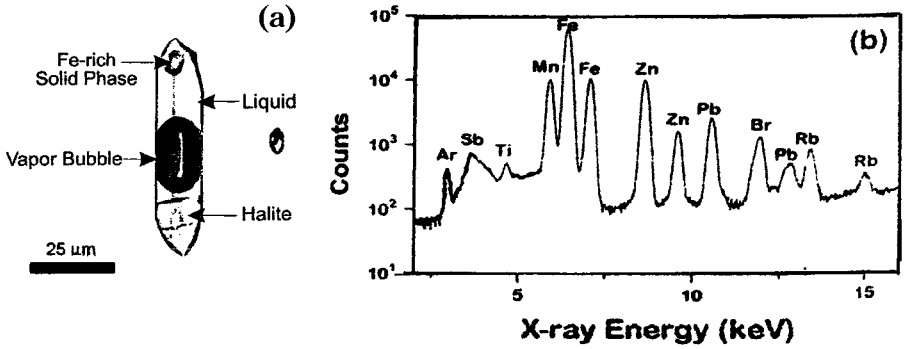

Figure 4. (a) Type-1 high-salinity fluid inclusion in quartz from the pegmatite. (b) Synchrotron X-ray fluorescence (SXRF) spectrum collected from a type-1 fluid inclusion such as in part A. (Reprinted with permission from ref 165. Copyright 1998 Canadian Mineralogist.)

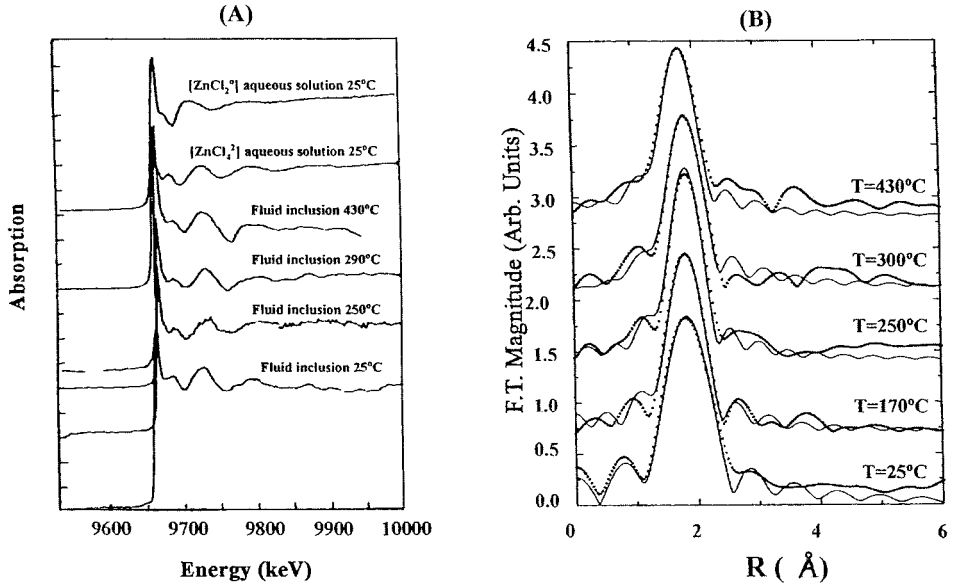

Figure 5. (A) Zn K-edge XAFS spectra collected in the fluorescence mode from the liquid phase of a type-1 fluid inclusion at temperatures ranging from 25 to 430 °C. Also shown are Zn K-edge XAFS spectra collected at room temperature from zinc chloride ($ZnC1_4^{2-}$ and $ZnC1_2^0$) aqueous solutions. (Reprinted with permission from ref 165. Copyright 1998 Canadian Mineralogist.) (B) Variation in the Zn−Cl bond length of the tetrahedral chlorozine complex as a function of temperature. The dashed line is the linear fit of the data. (Reprinted with permission from ref 165. Copyright 1998 Canadian Mineralogist.)

stant of the paleohydrothermal fluid with increasing temperature. These studies clearly demonstrate the potential of spatially resolved XAFS for determining the coordination environments of metals in highly localized regions of minerals previously identified by micro-SXRF imaging. The level of research activity utilizing spatially resolved SXRF and XAFS in geochemistry and cosmochemistry has increased dramatically over the past several years, and we anticipate that a number of important applications will appear in the literature over the next several years. As submicrometer spatial resolution at third-generation hard X-ray sources is becoming increasingly available to the geosciences community,[39,170] we expect that there will be an even more dramatic increase in research activities utilizing spatially resolved SXRF and XAFS spectroscopy in geochemistry and cosmochemistry.

A very exciting recent development involves the application of a soft X-ray microscopy, microspectroscopy, and spectromicroscopy to problems in mineralogy[171] and organic geochemistry.[172,173] Using secondary electron yield detection on a soft X-ray beamline at the Advanced Light Source (ALS), Droubay et al.[171] examined phase heterogeneity on a polished mineral specimen of ilmenite ($FeTiO_3$) by collecting images at both the Fe (~708 eV) and Ti (~465 eV) L edges. Chemically distinct compositional variations were evident in the energy-dependent contrast images, which arise from heterogeneous distribution of the Fe and Ti in the sample (Figure 6a). The Fe- and Ti-rich domains identified in the X-ray micrographs is consistent with the layered structures indicative of phase separation between ilmenite and the isostructural hematite (α-Fe_2O_3) and magnetite (Fe_3O_4), both of which commonly occur in mineral assemblages with ilmenite. On the basis of the multiple chemical compositions resolved in the X-ray images, Ti and Fe L-edge XAFS spectra were collected within each of the two major domains identified. Examination of multiple regions within each of the domains by Fe L-edge XAFS demonstrated chemical inhomogeneity at a <1 μm scale within the domains, albeit these variations were small compared to the large differences in the Fe L-edge XAFS spectra between the domains (Figure 6b). Differences in the Fe L-edge spectra arise from the presence of multiple Fe-bearing phases with varying Fe(II)/Fe(III) ratios. By

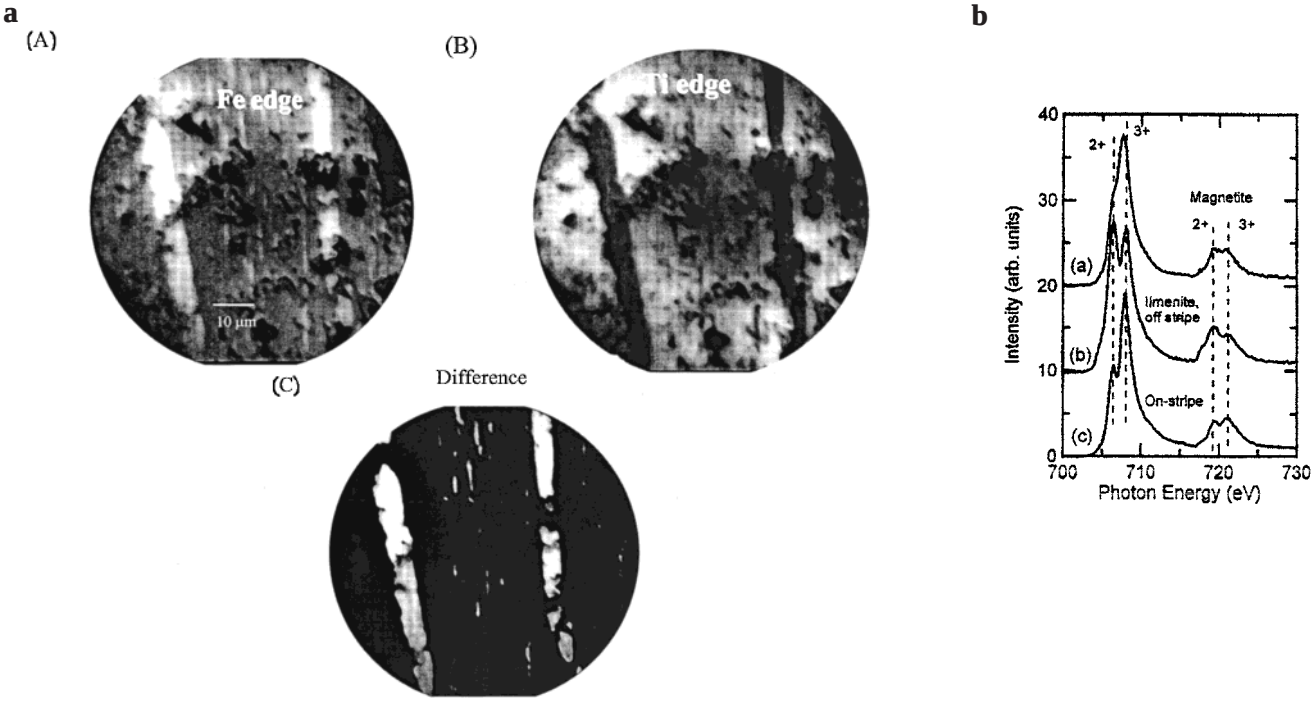

Figure 6. (a) XPEEM micrographs of the ilmenite surface at photon energies of (A) 708 eV, near the maximum of the FeL_3 edge, and (B) 465 eV, near the maximum of the TI L-edge structures. (C) Difference image of the first two to highlight the lamellar structure of chemical domains. For reference, the two types of domain are called "on-stripe" and "off-stripe." (Reprinted with permission from ref 171. Copyright 1997 Elsevier.). (b) X-ray absorption spectrum of the Fe L edge from the two types of domains seen in the micrograph of Figure 6a, called "on-strip" (c) and "off-stripe" (b). The spectra have been normalized to the same edge−jump ratio (peratom basis) to highlight the fine structure differences between the two regions. Also shown in part a is the spectrum from magnetite for comparison. The main L_3-edge peak in magnetite is at a slightly different energy from that of the ilmenite sample. The broken lines indicate the strongest features due to Fe in the 2+ and 3+ charge states. (Reprinted with permission of ref 171. Copyright 1997 Elsevier.)

assuming that the variations in the Fe L-edge spectra arose from a simple two-component system (ilmenite and hematite), theoretical models of component spectra were used to quantify the Fe valence states in the two mineral phases.[171] In contrast, the Ti L-edge spectra from each of the two domains were remarkably similar, suggesting that the Ti was exclusively associated with the ilmenite component of the mineral assemblage. This pioneering study demonstrates the utility of soft X-ray micro-XAFS for examining natural samples to provide surface-sensitive information on the structure of minerals and complex mineral assemblages as well as to study surface-facilitated reactions, such as sorption and oxidation−reduction phenomena.[123] The advantages of secondary electron yield detection for such measurements is that no special sample preparation is required beyond what is normally employed for optical microscopy and that, when desired, the measurement is near surface sensitive, having a sampling depth of ∼10 nm. The disadvantage is that the measurement must be conducted in a vacuum, which limits studies requiring in situ analysis. Soft X-ray microscopy and microspectroscopy of hydrated samples can be accomplished in the transmission mode, provided the sample thickness is ≤∼100 nm (vide infra).[123,174]

Scanning transmission X-ray microscopy (STXM) and spectromicroscopy has been employed to examine organic functional group microheterogeneity in coal samples and other organic-rich sediments and rocks.[172,175−178] Samples of geochemically important organic rich sediments and rocks were examined at the soft X-ray beamline X1A at the NSLS, an insertion device beamline which employs a Fresnel zone plate objective and an order sorting aperture capable of yielding an ∼55 nm beam. Spatial heterogeneity of aromatic and aliphatic C distributions in coal as well as physicochemical heterogeneity of macerals and submaceral domains have been probed with STXM and C K-edge micro-XANES.[175−177] These studies demonstrate that very detailed information on organic functionality can be extracted from C−XANES within compositionally discrete domains at submicrometer resolution. For example, Cody et al.[172] examined the structural evolution of the important biogeopolymer, sporopollenin, by STXM and C−XANES spectroscopy. The deconvoluted C−XANES spectra of sporopollenin samples revealed that both saturated and aromatic carbon are major constituents. Examination of a range of samples by C−XANES revealed an increase of aromatic character paralleled by loses of aliphatic and hydroxylated aliphatic C with increasing maturation. Structural changes in vitrinites have also been examined by C−XANES[178] and provided important insights into thermal maturity dependence of photochemical oxidation pathways and kinetics. These studies have demonstrated the tremendous potential of soft X-ray microscopy and spectroscopy at the C K edge to provide detailed structural information on organic-rich sediments of geochemical significance.

Utilizing the same soft X-ray beamline (X-1A at the NSLS), Jacobsen et al.[82] examined ultrathin sections

of the ALH84001 Martian meteorite[179] as well as interplanetary dust particles (IDPs) by STXM and C−XANES. The C−XANES analysis of the ALH84001 meteorite thin section demonstrated that the rims surrounding carbonate globules are enriched with organic-C relative to carbonate-C compared to regions within the globules. This result is important as it demonstrates that organic-C is localized in a region of the ALH84001 meteorite also containing magnetite and sulfide crystals, which have been speculated[179] to be of biogenic origin. Preliminary studies of the IDPs indicate that organic-C is a common component of IDPs and thus may have been an important source of prebiotic C on Earth.[82]

While there are a number of important applications of soft X-ray microscopy and spectromicroscopy to earth and environmental samples, there are a number of limitations. As discussed previously, the X-ray photoemission (surface) and secondary electron yield (near surface) modes of detection do not require special sample preparation but typically are analyzed in a high-vacuum environment. Even under these conditions, it is often difficult to avoid surface contamination of rock sections with organics, and thus, the surface cannot be readily probed by XPS detection through the contamination layer. Using the transmission mode of detection allows for fully hydrated samples to be examined but requires ultrathin samples having a thickness on the order 100−200 nm. It is typically quite challenging to produce thin sections of rocks and soils having a thickness of ca. $\leq 30\ \mu$m without dislodging individual mineral grains or otherwise compromising sample integrity. As with some experiments in the hard X-ray regime, there continue to be reports of radiation-induced reactivity, especially promotion of oxidation−reduction reactions, particularly at third-generation X-ray sources. Regardless of these limitations, soft X-ray microscopy and microspectroscopy provide opportunities to collect spatially resolved chemical information that is not available with other methods and will undoubtedly become a critical spectroscopic probe of interfacial phenomena of geochemical and environmental interest.

2. Soil and Environmental Sciences

It is now widely accepted that specific information on chemical speciation and chemical species transformations is prerequisite to the development of a comprehensive understanding of toxic element behavior in the environment. Furthermore, this information is required to properly predict contaminant fate, to develop effective and rational remediation strategies, or to provide realistic and accurate risk assessments. Unfortunately, our understanding of the importance of chemical speciation has advanced more rapidly than the analytical capabilities to determine it, particularly in complex systems such as soils, sediments, and waste forms. Conventional spectroscopic and analytical methods of investigating chemical speciation often lack the sensitivity required and usually prohibit investigation under environmentally relevant conditions, for example, on moist samples using minimal or no chemical pretreatment.

In contrast, synchrotron-based techniques have emerged as powerful tools for determining the chemical speciation of a wide variety of toxic elements in moist soil samples, waste forms, and biological specimens with little or no chemical pretreatment at detection limits that, on the average, exceed those of conventional methods by several orders of magnitude. The use of conventional XAFS techniques applied to the environmental sciences first appeared in the literature in the late 1980s, and since that time there has been an explosion in the application of XAFS to environmental problems.[21,170,180] XAFS spectroscopic investigations have provided unprecedented molecular-level information on reactive mineral phases in soils and sediments and have provided the framework for understanding a number of critical surface-controlled reactions in the environment. Additionally, critical mineral surface reactions involving adsorption- and surface-facilitated polynuclear/nucleation and oxidation−reduction phenomena of a range of contaminants have been investigated by XAFS, and these have been reviewed in detail.[21,170,180] While these bulk XAFS studies have and are continuing to produce important molecular-level information on a wide range of mineral sorbents and environmentally relevant sorbates, they have been primarily conducted on homogeneous model monomineralic systems. Recent developments and deployment of synchrotron-based microanalytical techniques over the past decade, especially in the past five years, are allowing earth and environmental scientists, working on a range of environmental problems, to provide fundamental molecular-level information on contaminants in natural samples. Spatially resolved SXRF and XAFS allow for the study of molecular-level processes occurring at critical boundaries in earth and environmental sciences, such as along mineral grain and mineral assemblage boundaries, along fractures and pore linings, at the plant root/soil interface, and at microbe/mineral assemblage interfaces.[21]

Use of SXRF to interrogate reactive mineral grains in soils and geological media and to probe environmentally relevant particulates were among the first applications for routine trace element mapping at dedicated synchrotron-based hard X-ray microprobes.[3,5,7,8,11,17,21,126] Early studies demonstrated the utility of SXRF for the nondestructive analysis of trace elements in atmospheric particulates[17] and particulates emitted from coal-fired power plants (fly ash)[3,7] at a spatial scale of $\sim 5\ \mu$m. These studies demonstrated that trace element concentrations in environmental particles could be readily determined by SXRF, whereas they were not detectable by electron microprobe analysis. They also revealed heterogeneous distributions of environmentally relevant trace elements, such as As, Pb, and Cr, within individual particles and that the concentrations of various metals and metalloids vary as a function of environmental particle diameter.[7] Distribution patterns of contaminants and elemental co-associations within individual fly ash particles provide important information on the mechanisms controlling contaminant solubility. The feasibility of micro-XANES col-

lected at the As, Fe, and Cr edges on individual fly ash particles was also demonstrated in these early studies.[7]

Kaplan et al.[181] employed a combination of micro-SXRF and SEM-EDX analysis of groundwater colloids collected in the vicinity of a contaminated aquifer to provide evidence for colloid facilitated transport of contaminants. SEM-EDX analysis of colloids deposited on a 0.05 μm filter was used to image the colloids and, along with elemental composition, provide information on the mineral phases present. The colloids were found to have a mean diameter of 440 nm and to be comprised of the minerals quartz, hydroxy-interlayered vermiculite, and kaolinite as well as a low abundance (<10%) Ti-rich Fe−oxide phase. Contaminant metals, including Cr, Pb, Cu, and Ni, were measured via micro-SXRF at a 10 μm spatial scale for colloidal aggregates collected from the contaminated aquifer but never for colloids collected from control wells. Contaminant metals were only measured in regions enriched with Ti and Fe, suggesting that the metals were co-associated with the low-abundance Ti-rich Fe−oxide phase identified by the SEM-EDX analyses. This study demonstrated the complementary nature of conventional electron microprobe and micro-SXRF techniques for providing specific information on environmental particles and particle aggregates and for defining important processes regulating contaminant transport.

Valence state is a critical parameter controlling contaminant mobility, bioavailability, and toxicity. For example, it is well recognized that Cr(VI) is the mobile and toxic form of Cr in the environment, while Cr(III) is both relatively insoluble and nontoxic. Likewise, U(VI) is the soluble form of U in the environment, while the low solubility of U(IV) limits its mobility and bioavailability. Other aspects of contaminant chemical speciation are also critical to defining mobility and bioavailability, such as structural incorporation of contaminants into soil minerals on aging leading to sequestration and long-term stability. Thus, to predict contaminant transport or to fully appreciate the risks associated with metal and metalloid contamination in the environment, information on chemical speciation of contaminants as well as on the biogeochemical mechanisms controlling chemical speciation dynamics must be known. Additionally, designing or implementing remedial strategies for contaminated sites also requires knowledge on the chemical speciation of contaminants in environmental media as well as on how various chemical or biological remediation strategies modify contaminant speciation. Synchrotron-based X-ray techniques are emerging as important tools for characterizing contaminant speciation in environmental media and for examining biogeochemical mechanisms involved in chemical species transformations.

Bajt et al.[182] employed micro-XANES at ~150 μm lateral spatial resolution to examine Cr valence states in chemically modified cementitious waste-form analogues. This study demonstrated that the addition of sulfides to the cement prior to reaction

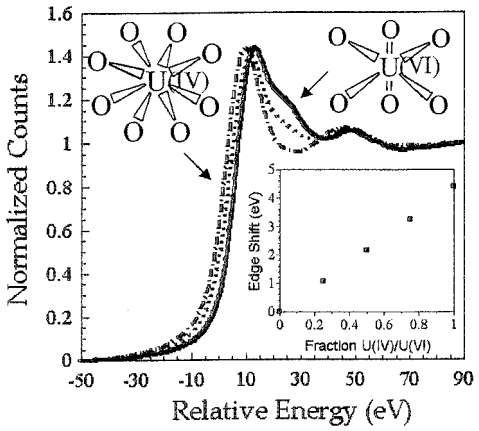

Figure 7. Uranium L_{111} XANES spectrum of U(IV) (—), U(VI) (- - -), and an equal admixture (· · ·). A linear relationship exists between the edge position and the proportion of U(VI)/U(IV) (inset). There are also differences in the postedge region attributed to the presence of O=U=O axial oxygens. (Reprinted with permission from ref 181. Copyright 1994 American Chemical Society.)

with a Cr(VI)-containing simulated waste stream stoichiometrically reduced Cr(VI) to Cr(III), thus enhancing chemical as well as physical immobilization of the Cr. While this study demonstrated the utility of micro-XANES for providing environmentally relevant information on Cr valence states to within ± 5% ($Cr(VI)/Cr_{total}$), it did not provide information on spatially variable chemical composition of the waste form.

Bertsch et al.[183] examined mineral grains and mineral aggregates from U-contaminated soils by SXRF and micro-XANES spectroscopy. Spatially variable U concentrations were delineated at a ~10 μm scale, and spatially variable elemental associations were used to infer distinct populations of U.[183] It was proposed that one population is comprised of highly localized regions ranging in size from ~50 to 200 μm, having elevated U concentration and being deplete in elements commonly associated with soil minerals, such as Fe and Mn.[184] The second major population was identified as regions having lower U concentrations and also containing high concentrations of other elements commonly associated with soil minerals. On the basis of the elemental associations delineated in the SXRF spectra, it was inferred that the first population is comprised of discrete U phases or significant secondary U precipitates on mineral grains while the second population represents U sorbed to soil minerals. Micro-XANES analysis was used to determine the valence state of U associated with the contaminated soil particles based on the energy of the absorption edge and on the diagnostic feature to the high-energy side of the main absorption peak attributed to multiple scattering in the direction of the O−U−O axial oxygen atoms of the uranyl moiety, representative of U(VI)[183] (Figure 7). Micro-XANES (50−200 μm scale) spectroscopic interrogation of the U-rich mineral grains and aggregates demonstrated that the former population was comprised of two distinct populations having U in primarily either the VI or IV valence state, while the latter population was exclusively U(VI). It was suggested that the presence of highly localized U(IV)

phases preserved in aerobic soils decades after introduction is consistent with the introduction of U(IV) particulates as part of the contaminant source term.[183,184] This interpretation was confirmed in a later study where individual (~50−200 nm) or aggregated (~10−100 μm) uraninite ($UO_{2(c)}$) grains were identified in these contaminated soils by electron microscopy and convergent beam electron diffraction analysis.[185] Additional analysis of mineral grains from these and other U-contaminated soils prior to and following extraction with carbonate solutions revealed that the more dispersed or 'sorbed' U(VI) phases were comprised of a soluble and insoluble fraction.[184,186] Transmission electron microscopy and selected area electron diffraction of the insoluble fraction indicated that it was predominately comprised of meta-autunite $Ca(UO_2)_2(PO_4)_2 \cdot 4H_2O$,[184,185] while microfluorescence spectroscopic interrogation of the readily soluble phase indicated that it was most likely comprised of a poorly ordered uranylhydroxide phase.[186] The formation of meta-autunite in the contaminated soils was also attributed to the contamination source term, since tributyl phosphate (TBP), a compound used to purify U, was believed to have been released to the environment as a co-contaminant.[185] Several other recent studies have also employed micro-SXRF and micro-XANES to examine the biogeochemical dynamics of U in environmental media or in environmentally relevant systems.[187−190]

Several recent studies have examined the distribution and chemical speciation of contaminants in soil and rock thin sections.[107,191,192] Duff et al.[107,191] used micro-SXRF and micro-XAFS to examine the distribution and chemical speciation of Pu on rock thin sections prepared from core materials collected from Yucca Mountain (YM), NV, the proposed high-level geological repository being commissioned by the U.S. Department of Energy. These experiments involved equilibrating simulated groundwater of low Pu(V) concentration (~10^{-6} M) with 30 μm thin sections of rock samples taken from ~446 m below YM, a subsurface unit proposed to be a reactive barrier to possible radionuclide migration. Elemental distribution maps generated via micro-SXRF with nominal beam sizes of 15 and 7 μm (NSLS and APS, respectively) revealed that Pu was heterogeneously distributed, being highly localized in ~100 μm regions associated with a mineral assemblage comprised of the 2:1 phyllosilicate mineral, smectite, and the Mn−oxide, ranciete [$(Ca, Mn^{2+})O \cdot 4Mn^{4+}O_2 \cdot 3H_2O$][107] (Figure 8). Extensive elemental mapping of several regions on the thin sections demonstrated that Pu was only detectable in these Mn−oxide and smectite-rich fracture fill materials, suggesting preferential sorption to low-abundance reactive mineral phases. This result is surprising as the more abundant Fe−oxide (hematite) and zeolite (clinoptilolite) phases were expected to be the predominant reactive minerals with respect to Pu sorption. This information is critical to the development of more accurate reactive transport models, which typically identify important reactive mineral phases based on surface area, relative abundance, and reactivity determined in batch sorption experiments using model monomineralic phases.

The environmental chemistry of Pu is complex, as Pu can exist in four oxidation states simultaneously with varying solubility and surface reactivity. The lower valence Pu(III) and Pu(IV) have low solubilities and predictably high surface reactivity due to their high charge. Conversely, Pu(V) and Pu(VI) exist as the dioxo cations PuO_2^+ and PuO_2^{2+}, which have greater solubilities and are less sorptive than the lower valence species. Micro-XAFS analysis of Pu (L_{III} edge 18.054 keV) rich regions on the rock thin sections demonstrated that Pu valence states were spatially variable between Mn−oxide/smectite-rich mineral bodies, being predominately Pu(V) in one region and Pu(VI) in a second region. While surface-facilitated oxidation of Pu(V) to Pu(VI) was evidenced in region 2, it is not clear if the Pu in region 1 remained in the Pu(V) form of the initial groundwater simulant or if it disproportionated to Pu(IV) and P(VI), having an identical average absorption edge energy as Pu(V), occurred on the mineral surfaces.[107] Preliminary Pu L_{III}-edge micro-EXAFS spectra of these same regions revealed an absence of first-shell splitting of the Pu−O bonds typically associated with axial and equatorial oxygen atoms.[191] This result was consistent with the lack of multiple scattering resonance to the high-energy side of the main absorption feature in the XANES spectra and suggests that the coordination environment of sorbed Pu (VI) results in a lengthening of the axial Pu−O bonds.[191] The other important result from the micro-EXAFS analysis was the lack of evidence for Pu backscattering in the second shell, suggesting that cluster formation or secondary precipitation of Pu on the mineral surfaces was not an important mechanism leading to the preferential sorption to the Mn−oxide/smectite mineral assemblage.

Manceau et al.[192] interrogated 30 μm thin sections of a Zn-contaminated soil collected in the vicinity of smelter with micro-SXRF and micro-XAFS spectroscopy. Employing a nominal beam size of 2 μm, elemental distribution maps were generated along mineral grain boundaries, within micropores, and within the clay matrix. On the basis of interelement relationships in the micro-SXRF spectra, it was concluded that the Zn was heterogeneously distributed, being present in three major populations. One population, characterized by highly localized regions of Zn, is co-associated with Fe-rich mineral grains. Another population, characterized by lower more diffuse Zn populations, is associated with Fe-rich regions in the clay matrix material. The third population, having the highest Zn concentrations in highly localized regions, is associated with Mn-rich spherule regions, approximately 250 μm in diameter. On the basis of bulk mineralogical, elemental, and Zn K-edge EXAFS analysis, it was concluded that ~50% of the total Zn was associated with a phyllosilicate mineral in the clay matrix and the remainder was present in the regions of localized elevated Zn in the populations identified above. Information on the mineral assemblages within the localized regions of elevated Zn concentration was inferred from Fe K-edge and Mn

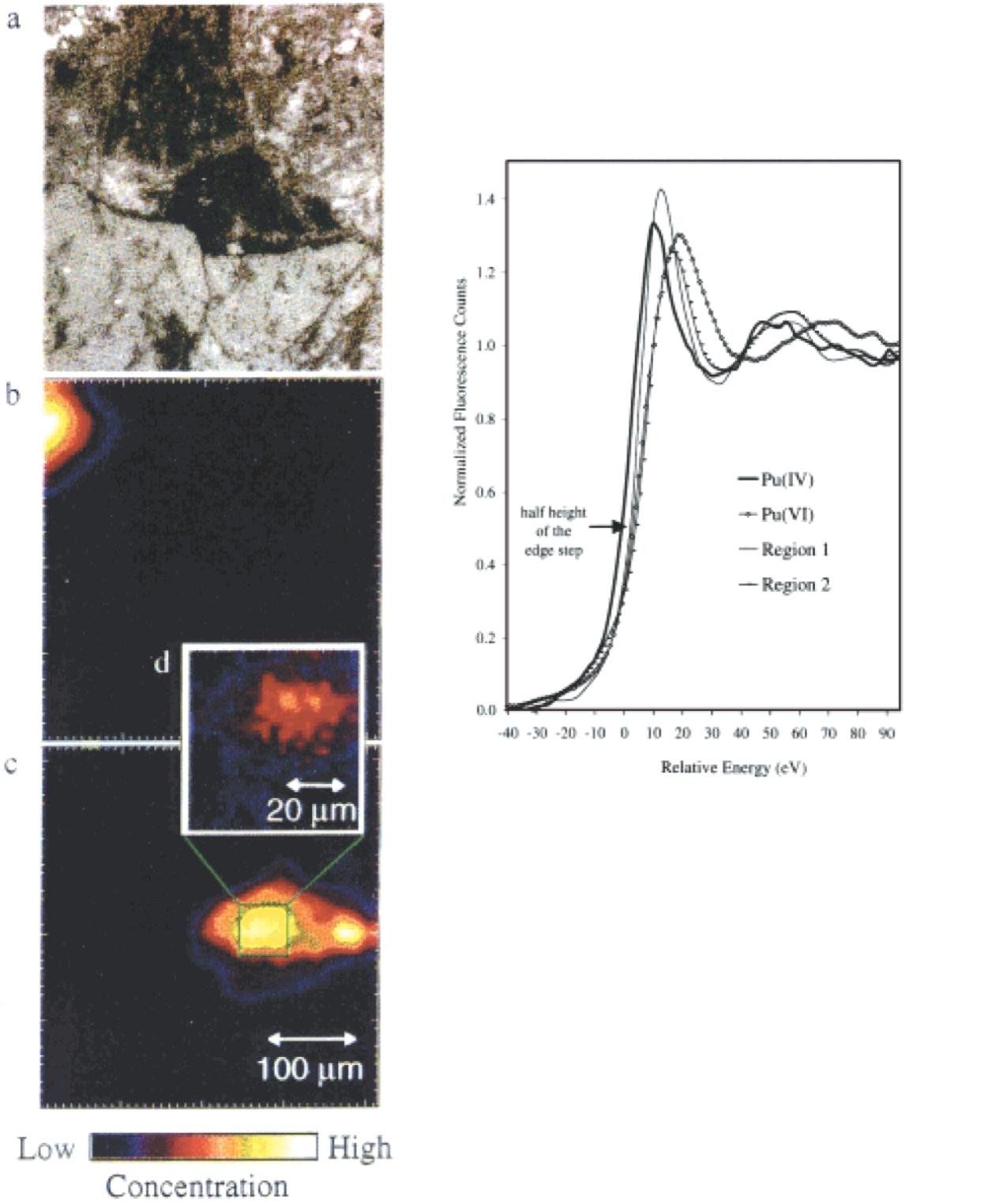

Figure 8. Photomicrograph of the manganese and iron oxides phases I area I (TS3) under reflected light (scale bar, 100 μm). The silver-colored structure in the upper left corner is hematite, the center area is a manganese oxide, and the surrounding features are highly zeolitic. Complementary micro-SXRF elemental map images of panel a showing spatially localized (b) Fe, (c) Mn, and (d) Pu. (e) Pu-Xanes spectra for the standards Pu(IV) and (VI) and regions 1 and 2 on the tuff demonstrating the edge energy shift with oxidation state at the half-height of the edge step as labeled with an arrow. The average edge energy for TS3 (region 1) is slightly more than midway between Pu(IV) and Pu(VI), which, based on relative edge energy, would be consistent with Pu(V) species. Small amounts (submicrograms) of Pu standards were encapsulated in polystyrene for ease of handling and safety during the analyses. (Reprinted with permission from ref 107. Copyright 1999 American Chemical Society.)

K-edge micro-EXAFS spectra collected in regions characteristic of the various populations.[192] The Fe micro-EXAFS spectra collected on the mineral grains and in the clay matrix material were similar and closely resembled the mineral feroxyhite (δ-FeOOH). However, it is unclear how unique this solution was since there was no discussion of what other model minerals or combination of minerals were used for

comparison.[192] For example, Zn−hydroxycarbonate$_{(c)}$ is a likely candidate phase given the geochemical environment and it was not included as a reference phase. The Mn K-edge micro-EXAFS spectra collected in Mn-rich nodules closely resembled hexagonal birnessite, although the same caution with this interpretation is warranted. The Zn K-edge micro-EXAFS spectra collected in localized regions characterized by the Mn-rich nodules resembled model spectra of Zn sorbed to birnessite at low surface coverage (Zn/Mn = 0.008) compared to higher surface coverages (Zn/Mn = 0.069−0.126). The Zn coordination environment at low surface coverage is characterized by decreased Zn−O and Zn−Mn bond lengths, compared to samples having higher Zn surface coverage. The decreased interatomic distances at low Zn surface coverage was attributed to the preferential sorption of Zn below/above vacant sites of the phyllomanganate layer in 4-fold coordination.[192] This study demonstrated the utility and complementary nature of micro-SXRF and micro-EXAFS for examining contaminant speciation in minimally disturbed environmental samples.

Several investigations have utilized X-ray microprobes to examine biogeochemical reactivity of metals and metalloids in the rhizosphere (soil−root−microbial consortia environment), within soil aggregates, and at the sediment−water boundary.[100,126,193−197] Schulze et al.[193] utilized micro-SXRF and micro-XANES to examine Mn concentrations and valence state distribution patterns in the vicinity of living plant roots to test the hypothesis that the pathogenic fungus *Gaeumannomyces graminis* (Ggt.) induces Mn deficiency in host plants by catalyzing Mn(II) oxidation. The elemental maps generated via micro-SXRF demonstrated elevated concentrations of Mn in the vicinity of the root surface, particularly those roots infected with Ggt.[193] Employing a method for quantifying Mn valence states from the Mn K-edge XANES spectra,[194] it was demonstrated that the Mn concentrated in localized regions of roots infected with Ggt. was predominantly in the sparingly soluble Mn(IV) oxidation state, present as discrete oxyhydroxide precipitates within the infected roots. The lower concentration of Mn in the surrounding media was found to remain in the soluble Mn(II) valence state throughout the course of the experiment. This study represents the first unambiguous test of the fungal-induced oxidation hypothesis and further demonstrates the utility of the X-ray microprobe to examine plant, soil, or other environmental samples in situ or with little manipulation or sample pretreatment.

A more recent experiment conducted at the third-generation APS demonstrated the utility of X-ray phase-contrast imaging coupled with micro-SXRF and micro-XANES for examining plant roots infected with the micorrhizal fungus *Glomus mosseae*.[100] Images generated at a 5 μm spatial resolution via monoenergetic (11.9 keV) X-ray phase contrast microscopy of wet mounted roots were far superior to optical images generated following traditional chemical fixation and staining protocol.[100] Furthermore, utilizing a zone plate focusing device, SXRF elemental mapping and micro-XANES was also conducted at a spatial scale of $1 \times 3\mu$m. The results demonstrated variable distribution patterns of Mn, Fe, Cu, and Zn within the infected roots and that the Mn was primarily in the Mn(II) valence state. This study was the first to demonstrate the capabilities of a third-generation synchrotron facility for examining environmentally relevant processes at environmentally relevant concentrations and demonstrates that the predictions of an order of magnitude or better increase in spatial resolution and sensitivity with the availability of third-generation synchrotron facilities are coming to fruition.[21,126] The rhizosphere represents a biogeochemically complex region having a wide range of chemical gradients (concentration and type of organic ligands, pH, Eh, etc.) that vary on a small spatial scale. Biogeochemical processes in the rhizosphere play a major role in regulating elemental solubility and bioavailability. Thus, the availability of synchrotron-based X-ray techniques that probe these processes in situ will undoubtedly lead to a greater understanding of these key processes, which can then be exploited for bioremediation applications.

Recent breakthroughs in understanding how microscale processes control reactive chemical transport in soils have also been facilitated by micro-SXRF and micro-XANES spectroscopy.[126,195−198] Elemental distribution maps of Se in soil aggregates generated with micro-SXRF (10 μm beam) revealed heterogeneous distribution of Se within soil aggregates following uniform addition of Se(VI) to the soils and after 17 days of reactivity.[196] The micro-SXRF results demonstrated highly localized accumulations of Se, as much as a 20-fold local enrichment with respect to total Se, in the vicinity of decomposing roots within the aggregates. This observation was interpreted as being consistent with localized reduction of Se(VI) to the less mobile Se(IV) and insoluble Se(0) in the vicinity of the decomposing roots represented by high microbial activity.[196] This assertion was confirmed in a later study where micro-XANES and spectromicroscopy were used to examine Se valence state distributions in the soil aggregates[126] using previously developed methods for estimating multiple Se valence states.[199] Valence state maps generated at the Se K-edge (12.66 keV) and with a nominal beam size of 100 μm clearly reveal that the localized regions of elevated Se concentration measured in the vicinity of the decaying plant roots were dominated by the less mobile Se(IV) and especially the insoluble Se(0) species (Figure 9).[126] While it has long been recognized that reduced microsites in soils play an important role in chemical cycling, it has heretofore been difficult or impossible to make measurements on elemental concentrations and especially valence states free of artifacts. Heterogeneous elemental concentrations within individual soil aggregates have important implications for reactivity, and the quantification of such heterogeneities is required for any detailed mechanistic model of chemical cycling.

Another critical process controlling trace element and contaminant cycling involves mass transport and diffusion across critical interfaces, such as the water−sediment boundary. Tokunaga et al.[195,197] utilized

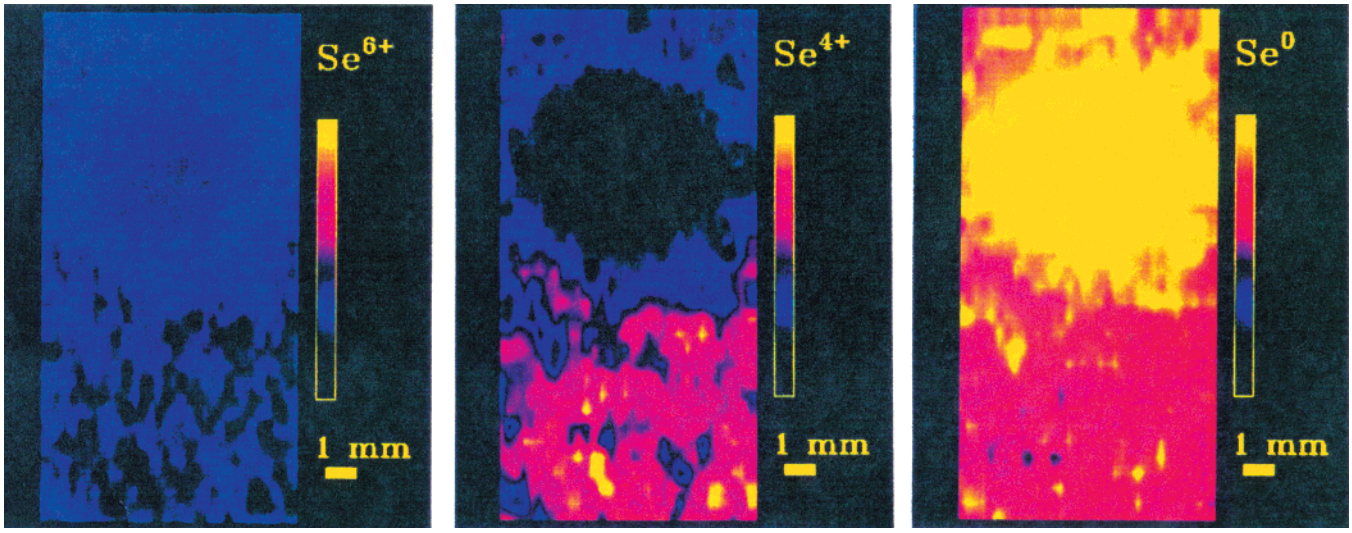

Figure 9. Micro-XANES of selenium oxidation state distributions provides direct experimental support for microsite Se(VI) diffusion and reduction to Se(0). The left, middle, and right map show relative abundance of selenium in the VI, IV, and 0 oxidation states in sediment and decomposing plant root tissue. The circular zone in the upper half of each frame is concentric with 4 mm diameter cross-section of root tissue. (Reprinted with permission from ref 126. Copyright 1995 American Institute of Physics.)

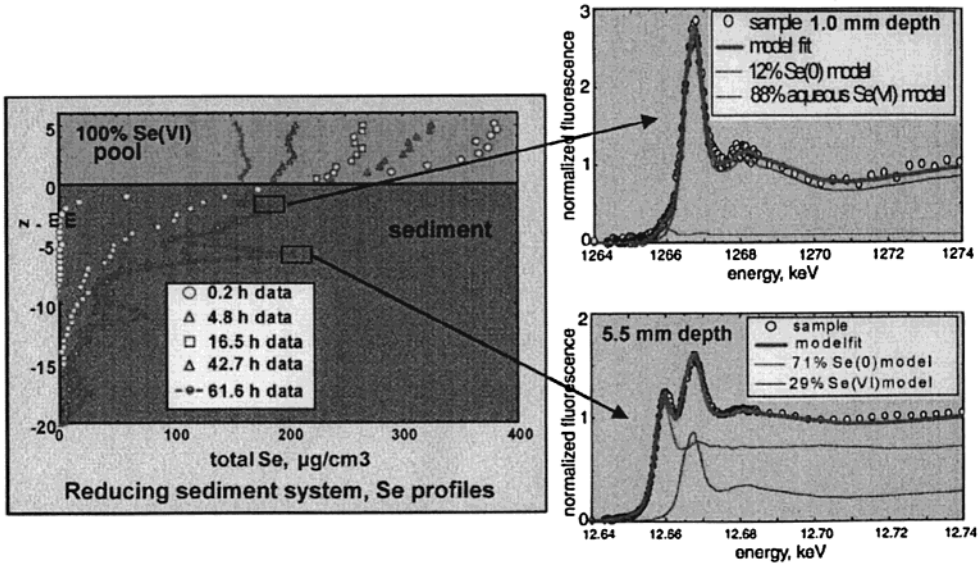

Figure 10. Significant Se(VI) reduction to Se(0) occurs within 5 mm of the pool−sediment boundary. (Reprinted with permission from ref 197. Copyright 1998 American Chemical Society.)

micro-SXRF and micro-XANES to demonstrate the importance of localized reactions within millimeters of the sediment−water interface for controlling Se concentration gradients. Utilizing a novel experimental cell design, real time, in situ vertical Se concentration and valence state profiles across the water−sediment boundary were measured by micro-SXRF and micro-XANES spectroscopy.[197] Following the introduction Se(VI) to ponded water above the soil columns, localized regions of Se accumulation were detectable by micro-SXRF and followed as a function of time (Figure 10).[197] Of particular interest was the observed development of several localized maxima within the soil column at presumably random depth intervals. Micro-XANES analysis of these heterogeneously distributed zones of Se accumulation provided direct evidence that Se(VI) was being reduced to insoluble Se(0) over the course of the experiment (Figure 10),[197] suggesting that there are numerous zones of higher than average Se reduction rates in the soil column. An important finding was that rates of Se reduction in these heterogeneously distributed regions of Se accumulation were up to 10 times greater than the average reduction rates calculated by volume averaging over the entire depth interval.[197]

This observation is intriguing as, unlike the previous study where reduced microsites associated with decomposing plant roots were anticipated, there is no a priori identifiable microsites for Se reduction in the soil columns examined in this study.[197] Regardless of the exact mechanism involved in the evolution of spatially heterogeneous zones of Se reduction, this study demonstrates the power of synchrotron-based X-ray microprobe techniques for providing concentration and chemical speciation information in complex dynamic environmental systems. Such information has major implications to accurate mass transfer calculations and for identifying the mechanisms

controlling Se partitioning between the water column and underlying sediments.

Biological samples collected from contaminated environments have also been examined using a combination of micro-SXRF and micro-EXAFS spectroscopies.[200] Thin sections of shell fragments from turtles collected in a wetland contaminated with Ni, U, Cr, Cu, Cd, and Pb from a former nuclear materials production facility were examined by micro-SXRF at a 10 μm scale. The micro-SXRF analysis revealed that major contaminant metals were bioaccumulated and deposited in the bone, whereas no evidence for these metals was evident for the control samples. All metals were localized in the bone tissue to varying degrees, suggesting some time-dependent pattern in metal uptake and deposition since the apatite shell is deposited in discrete annuli. Regions resembling inclusions $\sim$100 μm in diameter could be observed visually by a petrographic microscope assembly, and these regions were always found to be highly enriched in Ni. Other localized regions of contaminant deposition could be delineated at smaller spatial scales of between $\sim$10$-$50 μm by micro-SXRF analysis. Contaminant metals were also found localized in the $\sim$50$-$100 μm bands associated with the keratin-based epithelial layer of the shells, which are also deposited in discrete annuli.

Shell fragments from turtles collected in a wetland receiving outfall from a coal combustion byproduct (fly ash) basin were also examined by micro-SXRF analysis. A number of metals and metalloids (As, Se, Pb, and Cu) typically associated with coal and its waste products were detected in the bone tissue; however, particularly high concentrations of Se were measured.[200] Similar to the samples described previously, the shell fragments demonstrated a localization of metals and metalloids in distinct regions within the bone and in the bands associated with the keratin coating. Contaminant association with the keratin could conceivably result from surface sorption to functional groups associated with the protein or via physiological incorporation of bioaccumulated metals and metalloids. Micro-XANES spectra generated in regions of elevated Se concentration within the keratin of a bone fragment demonstrate a coordination environment similar to a Se$-$methionine standard, suggesting that the Se exists predominantly in a coordination environment resembling Se-substituted methionine Se($-$II), a functional group generally associated with S-containing structural proteins. These data demonstrate that the Se associated with the epithelial layer has been bioaccumulated and metabolically incorporated into the protein structures.[200]

Two-dimensional XRF scans of hyperaccumulating aquatic plants exposed to selenate and chromate revealed >1000-fold increase in concentration of the contaminants in localized regions within the roots and leaves of *Lemna* and *Salvinia* compared to the exposure solution, consistent with previous findings for bulk tissue concentrations. The Se accumulated in roots of *Lemna* was localized in $\sim$50 μm regions corresponding to cell nuclei, whereas the Cr accumulated in localized $\sim$50$-$75 μm aggregates in *Salvinia* roots that were distinctly nonnuclear in nature. The Cr-rich aggregates in the cytoplasm resembled distinct structures, such as vacuoles, which are thought to be common storage sites for toxic metals in plants.[200] Spatially resolved Se K-edge micro-XANES spectra collected on these regions revealed that the Se accumulated in the nuclei of the *Lemna* root cells was predominantly in the Se(VI) valence state, although a slight decrease in the white line intensity suggests partial reduction of Se.

The Cr K-edge micro-XANES collected on the Cr-rich aggregates within the cytoplasm of the *Salvinia* root cells revealed nearly complete loss of the preedge feature associated with the localized 1s $\rightarrow$ 3d electron transition which is diagnostic of four-coordinate Cr(VI) species (Figure 11). The micro-XANES analysis revealed nearly complete reduction of the toxic chromate species to Cr(III), a relatively nontoxic form of Cr, suggesting a metabolically controlled detoxification mechanism.[200,201] Another recent study has also provided micro-SXRF and micro-XANES evidence for the biochemical reduction of Cr(VI) to Cr(III) in basalt rock sections by the microorganism *Arthrobacter oxidans* concomitant with toluene degradation.[202] These studies further demonstrate the utility of micro-SXRF combined with micro-XANES for examining the localization and chemical speciation of contaminants in complex samples of environmental relevance, including living biota or fresh tissue.

Soft X-ray microscopy, spectroscopy, and spectromicroscopy have only recently been applied to problems in the environmental sciences.[21,32,123,174,203$-$206] An early application involved the imaging of clay mineral aggregates in aqueous suspensions by X-ray microscopy.[203] While this[203] and a later related study[206] provided little insight into mechanisms controlling clay mineral aggregate formation, they did provide a demonstration of how amplitude and phase contrast soft X-ray microscopy could be used to examine environmentally important mineral phases directly in an aqueous media. A novel application of soft X-ray microscopy to complex environmental samples involved the imaging of aquatic and soil humic substances.[204] Humic substances (HS) are natural organic polyelectrolytes formed from the biochemical processing of plant and animal remains that play an important role in biogeochemical C cycles and in nutrient and contaminant behavior in the environment. While it has long been recognized that the macromolecular structure of HS is dependent on solution chemistry, it has been difficult to quantify dynamic macromolecular structure free of artifacts.[204] Understanding the macromolecular structure is important since it influences HS interactions with mineral and colloid surfaces, the stability of complex mineral$-$organic aggregates, the partitioning or complexation with contaminants, and C-cycling behavior in soils and sediments. Contrast images were collected in the water window (516.6 eV) and at the Fe and Cu L edges (697$-$706 and 933$-$936 eV, respectively), representing 2p $\rightarrow$ 3d electron transitions. The images collected at the water window are dominated by contrast in mass absorption of C and N

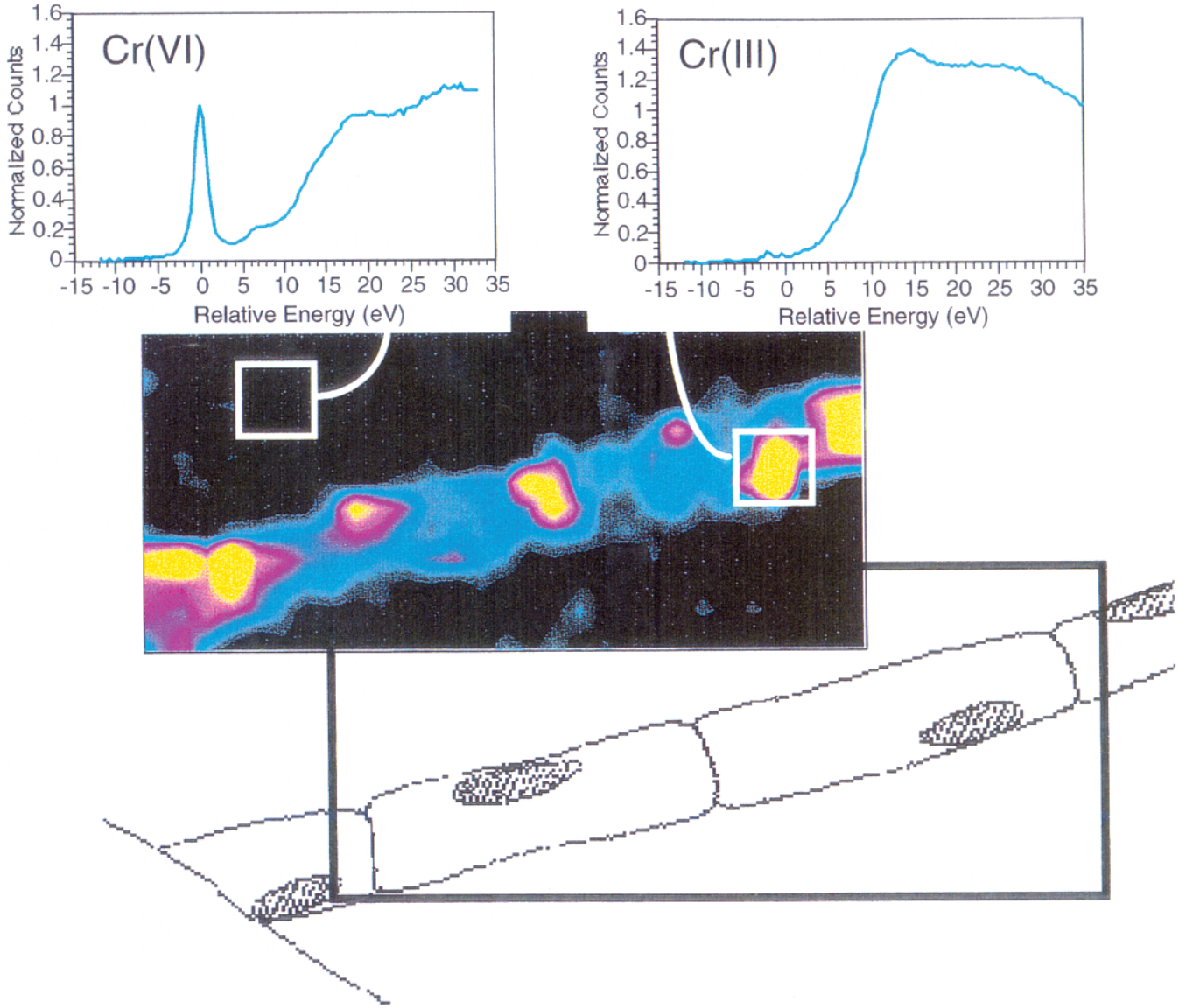

Figure 11. Micro-XRF image (1.5 × 0.2 mm) of the chromium distribution within rootlets of the hyperaccumulating aquatic plant, *Salvinia rotundifolia*. Plants were exposed to dilute levels of Cr(VI), a toxic form of Cr, and they had accumulated in the excess of 10 000 times the solution Cr in localized areas in single cells. Micro-Xanes demonstrated that Cr accumulated in the plant rootlet had been reduced to Cr(III), a less toxic form of Cr, which suggests a detoxification mechanism (Reprinted with permission from ref 200. Copyright 1997.)

atoms in the sample, which is used to determine the macromolecular structure of the HS as a function of solution chemistry, whereas the images collected at the Fe and Cu L edges provide information on HS−cation and −mineral associations.

The major findings of this study were that the macromolecular structure of HS is highly dependent on the source (terrestrial vs aquatic), HS concentration, pH, electrolyte identity and concentration, and the presence or absence of mineral phases.[204] The results indicate that HS exhibit a range of macromolecular structures in aqueous solution, not just coils (at high ionic strength and low pH) or elongated structures (low ionic strength and high pH) as previously believed. The macromolecular structures visible in acidic solutions with varying electrolyte concentration and identity ranged from globular structures in the 0.2−0.45 μm size range, ringlike structures in the 0.3−1.2 μm size range, sheetlike structures in the 2−8 μm size range, to threadlike structures in the 2−6 μm size range. For higher pH solutions and low DOC concentration, uniform aggregates having an average size of <0.1 μm predominated, whereas at higher DOC concentrations globular (0.2−0.5 μm) and sheetlike (1−5 μm) structures were also evident.[204] The ability to examine the macromolecular structure of HS as a function of solution chemistry and in the presence of mineral phases in a fully hydrated state is important, as differences in HS macromolecular structure modify the magnitude and rates of sorption processes, biotransformation of humic-bound contaminants, and the availability of organic C for biooxidation or biotransformation. Furthermore, there is little known concerning organic matter−mineral interactions at a molecular level, yet these clearly modify the surface chemistry of reactive mineral phases and influence important biogeochemical processes. This study demonstrates the power of soft X-ray imaging and spectromicroscopy to examine these important

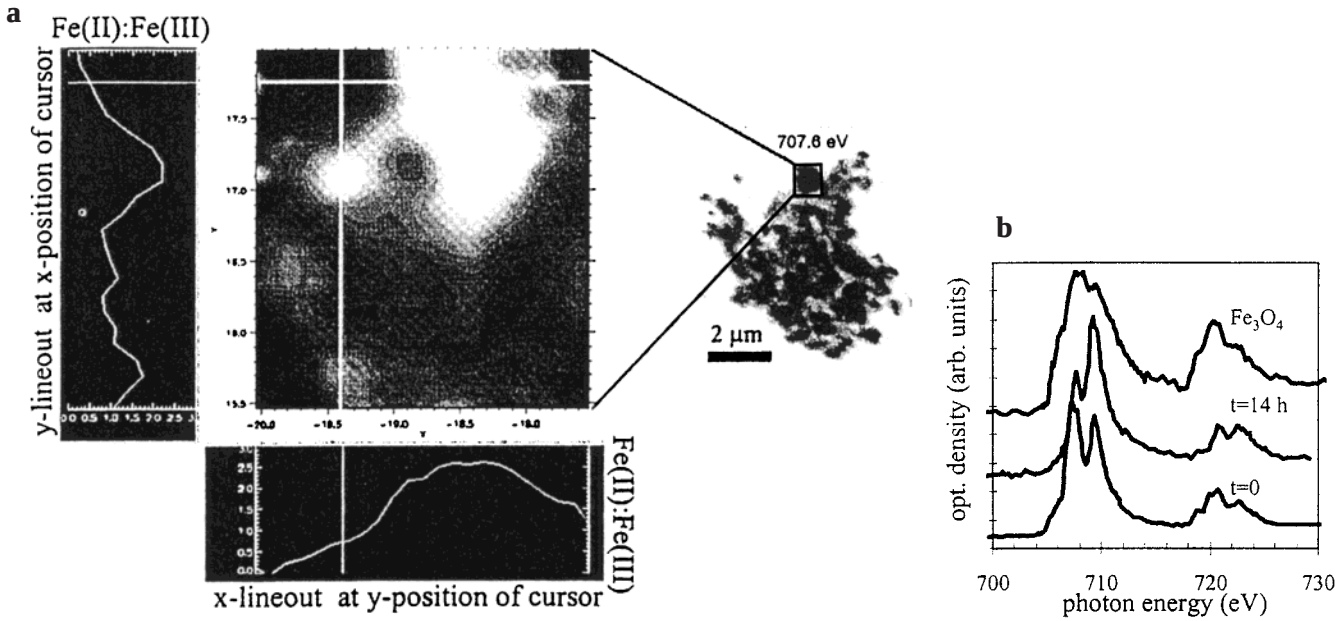

Figure 12. (a) Spatial distribution of the Fe(II):Fe(III) ratio in a single particle of SO_4-green rust. (b) Sample-averaged XANES spectra of SO_4-green rust before ($t = 0$) and after $t = 14$ h) reaction with CCl_4. A spectrum (STXM stack mode) of Fe_3O_4 is shown for comparison. (Reprinted with permission from ref 174. Copyright 2000 American Institute of Physics.)

processes in situ, and ongoing studies should continue to provide insights not available by other techniques.[21,204]

Recent interest in environmental microbiology and geomicrobiology has arisen in the past decade because of the importance of microbial−mineral interactions at controlling critical biogeochemical processes and because of the growing interest in bioremediation of contaminated sites. Soft X-ray microscopy and spectromicroscopy have recently been applied to examine mineral surfaces and microbial−mineral interactions.[123,171,174,204,207] Initial groundbreaking studies examining important biomineralized mixed valence Fe− and Mn−oxide phases formed by bacteria that either oxidize Mn and/or Fe to higher valence states or dissimilatory metal-reducing bacteria that reduce Mn and/or Fe to lower valence states by scanning transmission X-ray microscopy (STXM) and spectromicroscopy have recently been reported.[123,174,207,208] These studies demonstrate the ability of soft X-ray imaging, microspectroscopy, and spectromicroscopy to examine valence state distributions within single grains of these important phases.[174]

The mixed Fe(II)−Fe(III) green rust (GR) phase takes its name from its intense green to bluegreen color arising from intervalence charge-transfer transitions between crystallographically adjacent octahedrally coordinated Fe(II) and Fe(III) cationic centers. It is present in many suboxic sediments and soils, presumably resulting from microbially mediated processes, and has been found to be involved in several environmentally relevant abiotic redox transformation reactions, including the reduction of Se(VI) to Se(0)[208] and the reductive dechlorination of contaminant organics.[174] The distribution of Fe(II) and Fe(III) in a single grain of a GR phase was found by STXM at the Fe L edge to vary heterogeneously within a single grain and, in certain localized regions, to vary significantly around the expected ratio of 2:1 based on bulk analysis (Figure 12).[174] The heterogeneous distribution of valence state domains within a single grain is expected to have implications relative to the reactivity of redox-sensitive inorganic and organic contaminants. This study[174] also demonstrated the ability to conduct time-resolved experiments, where Fe valence states were followed with time following the introduction of the redox-sensitive contaminant CCl_4.

In another exciting application of STXM and spectromicroscopy, Rothe et al.[207] examined Mn−oxide micronodules, an important biomineralized phase commonly occurring in sediments. Initial spectromicroscopic images collected at the Mn L edge suggested heterogeneously distributed Mn(II) and Mn(IV) with no evidence for the existence of Mn(III) in the micronodules.[207] Another exciting aspect to this study was an image generated within the water window (516 eV), which demonstrated the ability to examine a bacterium attached to a Mn−micronodule, where some internal structure of the bacterium was visible.[207] In an extension of this initial study, Pecher et al.[174] generated valence state maps of Mn−micronodules demonstrating that Mn(II) was present throughout the micronodule but highly concentrated around the periphery compared to the Mn(IV) distribution (Figure 13). The authors were still unsure about the relative amount of Mn(III) present. While the contribution to the overall spectral intensity was minimal, it is possible that the Mn(III) could be only present as a surface-sorbed species and be masked by the bulk transmission measurements.[207] It is clear from these initial studies that the spatial and energy resolution of soft X-ray microscopy and spectromicrosopy, coupled with the ability to examine hydrated samples, provide unprecedented opportunities for future research efforts dealing with environmentally relevant mineral surfaces and their biogeochemical reactivity.

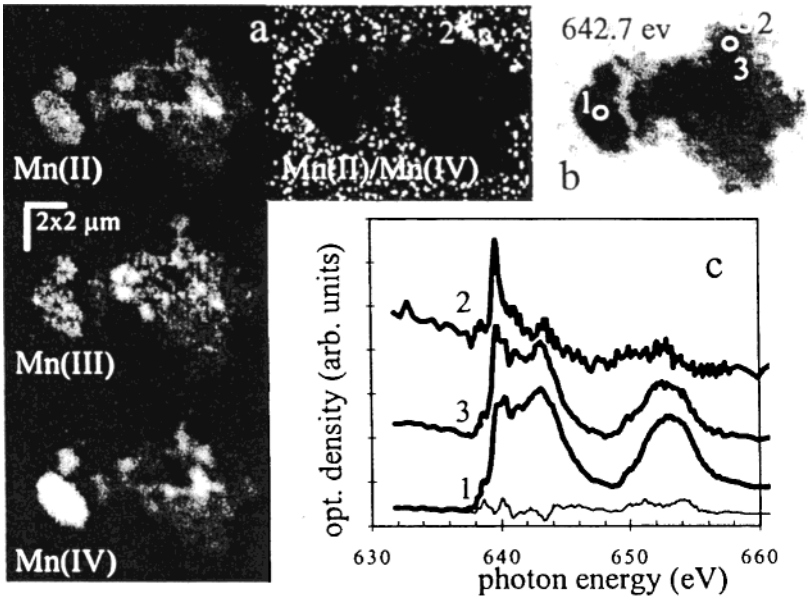

Figure 13. Charge state maps of Mn in a sample of Mc-micronodules (a), STXM image (b), and XANES spectra averaged over three different areas (c). The numbers correspond to the labeled areas in part b. (Reprinted with permission from ref 174. Copyright 2000 American Institute of Physics.)

B. Biosciences

The earliest applications of synchrotron-based X-ray microprobes in both the hard and soft energy ranges included studies on biological specimens[1,2,29,32,124,209−212] and applications using soft X-ray microscopes have been extensively reviewed.[96] Elemental distribution maps have been generated by micro-SXRF using hard X-ray microprobes in a wide variety of biological tissues and specimens, including bone,[2,209,213] cartilage,[37,212] teeth,[1,214−216] hair,[217,218] brain,[211] kidney,[219−221] heart,[222] and plant.[223−225]

Carvalho et al.[215] examined the distribution of trace elements in human molar teeth samples representing both healthy and caries (dental decay) restored with metallic amalgam. Trace element concentrations were found to be heterogeneously distributed with high concentrations of Zn, Ag,Sn, Hg, and Pb observed in teeth restored with metallic amalgam. The distribution patterns of these elements varied spatially between individual teeth, and this was attributed to different mineralization processes in teeth as well as from inhomogeneity of dentine and enamel materials. It was also concluded that the distribution patterns are suggestive of diffusion of these elements into the teeth from the amalgam constituents. Anderson et al.[214] also examined trace elemental distributions in dental tissues with micro-SXRF but also conducted real-time measurement of transport processes relevant to caries during demineralization using bromoacetic acid. The results of this study demonstrated the potential to examine both short- and long-term elemental distribution patterns and diffusion processes occurring in teeth.

The examination of Hg distributions in rat kidney following subcutaneous introduction of $HgCl_2$ by micro-SXRF demonstrated heterogeneous Hg distributions, with higher concentrations being evident for damaged proximal tubules compared with fine undamaged proximal tubules.[221] An altered distribution pattern of Zn and S was also evident in kidney tissue from exposed rats.[221] Determination of the concentrations and distribution patterns of trace metals in hair samples have also demonstrated the utility of micro-SXRF for evaluating the influence of metal exposure and on the mechanisms of incorporation of trace elements from the body into hair.[217,218]

An interesting application of micro-SXRF to understanding important biological processes involved the evaluation of myocardial blood flow in small contiguous regions by 2D mapping of heart tissue slices following the injection of Br-, Y-, Zr-, Nb-, Ba-, and I-doped microspheres into dogs.[222] The study confirmed the fractal nature of myocardial blood flow distribution, and it was suggested that local flow may become more homogeneous in smaller regions. This observation is important as micro-SXRF allowed for the measurements to be made on regions significantly smaller than previously reported. Using the micro-SXRF mapping approach also allowed for the measurements to be made on larger tissue samples compared to previous methods, which can induce artifacts since they require the tissue to be cut into very small samples.[222]

Micro-SXRF has been employed to examine elemental distribution patterns in plant tissues, including wood.[223,225] Berglund et al.[225] demonstrated the utility of micro-SXRF for the nondestructive analysis of wood, where 2D maps of 200 μm thin sections revealed heterogeneous distribution patterns of Fe, Cu, Ba, and Zn. Differential extraction and regions of localization could also be examined with the technique, and cell wall bound and precipitated metals associated with the hemicellulose/lignin matrix were discernible.[225] The nondestructive nature of the technique was a key feature that allowed for samples to be examined prior to and following extraction with chelation agents. It was suggested that this capability could be exploited in future studies focused on understanding the role of transi-

tion metals in catalyzing the decomposition of bleaching agents used in commercial preparation of pulp.[225] Compared to earth or material sciences, for example, far fewer studies utilizing hard X-ray microprobes to examine biological tissues have utilized the micro-XAFS capability to examine heterogeneous chemical state distributions. Most of the applications that have appeared were discussed in the previous section on soil and environmental sciences.[126,193,200,202] Illman and Bajt[223] did use micro-SXRF coupled with micro-XAFS to examine the distribution patterns and oxidation states of Mn, Fe, and Cr in wood tissue infected with wood-deteriorating fungi and wood treated with the preservative chromated copper arsenate (CCA). The study demonstrated that that fungi accumulates Fe into decaying wood and that the Fe(II)/Fe(III) ratio was higher in the decaying wood than in control regions, lending support to the hypothesis that Fe is involved in the fungal deterioration.[223]

As a result of both superior spatial resolution and the ability to examine lighter elements, soft X-ray microscopy has been utilized in studies of biological specimens and tissues to a far greater extent than hard X-ray microprobes and the applications have expanded dramatically over the past five years.[29,32,50,56,72,77,82,83,96,97,210,212,226−240,241−248] It is not possible to review the voluminous literature in detail herein. Rather, we will select a range of examples that illustrate the versatility and power of soft X-ray microscopy and spectromicroscopy as a tool for examining biological specimens, tissues, and molecules.

Early applications of STXM demonstrated the ability to examine a range of biological specimens, tissues, and biomolecules in a hydrated state, in some instances without the need for fixatives or staining, using absorption contrast working in the "water window" or at the C K edge.[29,50,210] The classic images of metaphase chromosomes of the bean *V. faba* generated by STXM demonstrated the ability to use chemical contrast to produce high-quality images of subcellular components and to use features in the C−XANES spectra to map DNA distribution in chromosomes.[29] In another study,[32] it was demonstrated that freeze-drying similar chromosomes by three different procedures all introduced significant structural artifacts when compared to a wet unsectioned chromosome. Several subsequent investigations[51,56,97,229,233,242] demonstrated the ability of chemical contrast STXM to map proteins, DNA, and inorganic constituents in various specimens, including fibroblasts,[56] sperm,[97,235] and human HeLa cells.[238] The images were generated by exploiting specific spectral features in the C K-edge XANES spectra based on relative concentrations and chemical environment of C═C, C═N, and C═O bonds that give rise to different π^* resonance intensities and energies (Figure 14). An example of STXM images of individual bull sperm cells along with DNA and protein distribution maps based on features in the C K-edge XANES spectra are illustrated in Figure 15. The images reveal no detectable DNA in the acrosomal cap and trace levels of DNA in the tail.[235] Furthermore, mitochondria in the midsection of the tail contain low levels of DNA relative to concentrations in the nucleus, and only trace levels of DNA are detectable in the tails. Also, the equatorial segment located near the center of the bull sperm head contains predominately protein, and there is a higher DNA concentration near the posterior end of the nucleus.[235] This and other studies have demonstrated species-dependent differences in DNA and protein distributions in sperm cells from a range of mammals. While the complexity of C K-edge XANES spectra may limit quantitative analysis of such spectra for chemically complex samples, the studies to date have demonstrated the usefulness of qualitative and semiquantitative approaches for producing chemical contrast images, which are related to relative concentrations and heterogeneous distribution of key biomolecules.

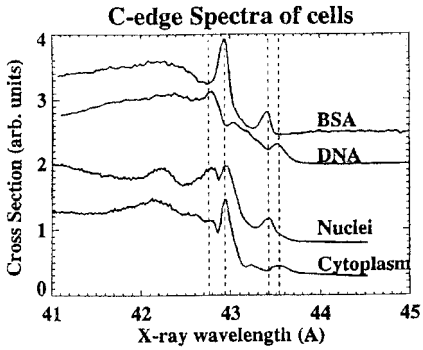

Figure 14. (Top) Spectra of DNA and bovine serum albumin (BSA). Due to the different concentration and environment of the bonds in DNA and BSA, the peaks from C═C, C═N, and C═O have different intensities as well as difference energies. (Bottom) Spectra of nucleus and cytoplasm of critical point dried CHO cell. The ratio between the DNA peak (4.275 nm) and BSA peak (4.294 nm) is higher in the spectrum from the nucleus than that from cytoplasm, indicating more DNA in nucleus than in cytoplasm. (Reprinted with permission from ref 235. Copyright 1996 Academic Press.)

Very exciting applications of soft X-ray microscopy for examining individual cells are continually emerging.[241,243−247] Of particular interest are applications involving the imaging of hydrated cells. Larabell et al.[241] examined both cyro-fixed cells and cells treated with siver-enhanced, immunogold labeling techniques by soft X-ray microscopy. Remarkable images revealing excellent ultrastructural detail of the nucleus and cytoplasm of fully hydrated single cells at ∼36 nm resolution were achieved in this investigation. Following cryo-fixation, hydrated mouse 3T3 fibroblast cells up to 10 μm thick were examined, revealing several nucleoli in the nucleus and numerous cytoplasmic organelles. The investigators reported no evidence for radiation damage in the X-ray microscope even after repeated imaging of the same cells.[241,243]

Using standard immunocytochemical methods involving silver enhancement of gold-tagged antibodies, the subcellular location of proteins in fully hydrated cells has been examined by soft X-ray microscopy.[241] Phase contrast images of ∼25 nm diameter microtubules arranged in a network within the cytoplasm of mouse mammary cells were readily apparent. In

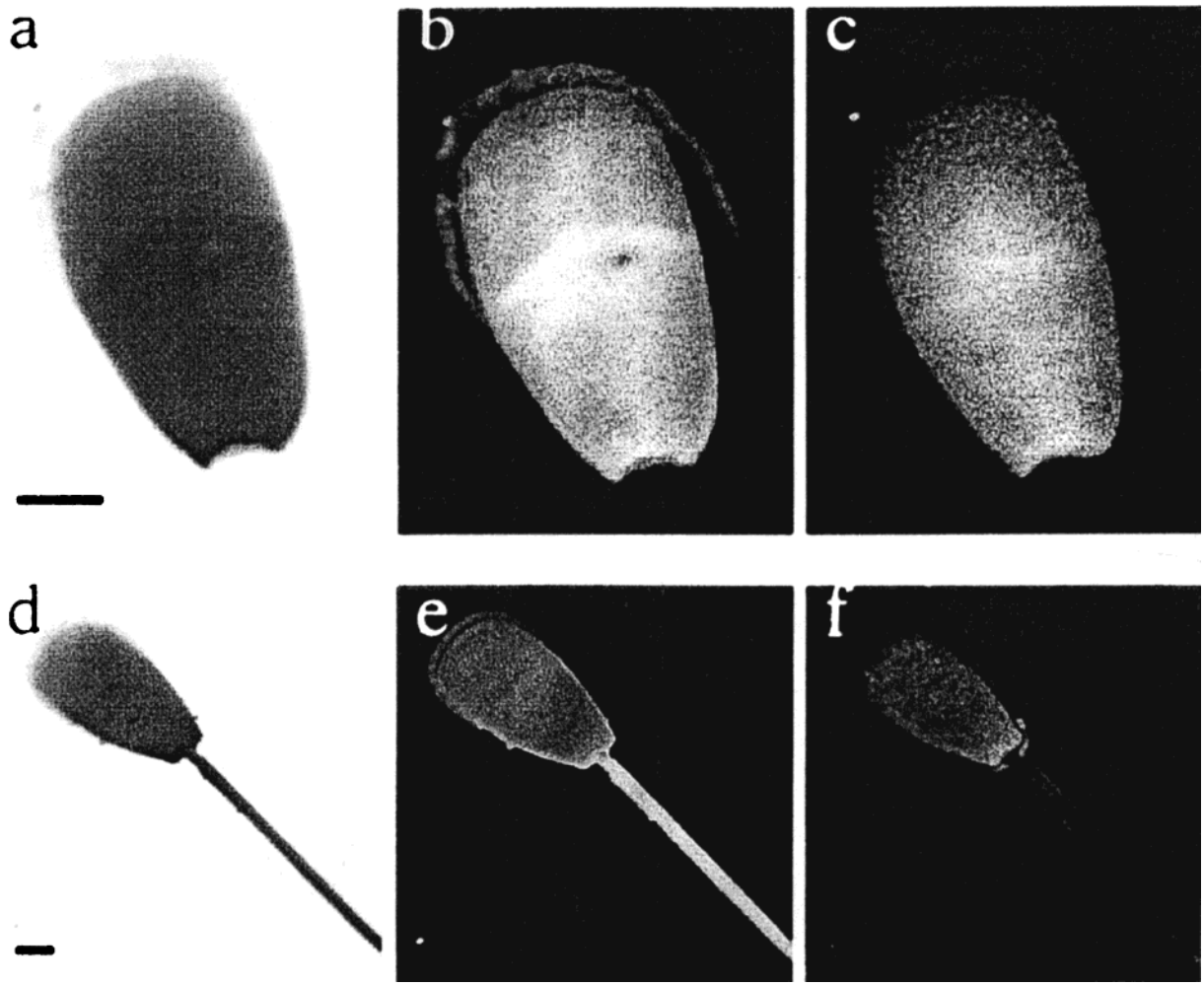

Figure 15. (a) STXM image of a bull sperm head at one of the wavelengths indicated in Figure 17 (4.279 nm). (b) Protein map of the sperm head. (c) DNA map of the sperm head. (d) STXM image of a bull sperm at one of the wavelengths indicated in Figure 17 (4.279 nm). (e) Protein map of this sperm. (F) DNA map of this sperm. The protein and DNA maps were obtained using the XANES imates. Bar: 2 μm. (Reprinted with permission from ref 235. Copyright 1996 Academic Press.)

another application,[243] frozen single algae cells were imaged by X-ray microscopy. The images revealed generally similar microstructure as revealed by TEM, although the X-ray microscopy revealed X-ray-dense spheres within the cell that were very sensitive to radiation damage. Fixation of the cells with glutaraldhyde also caused significant damage to the spheres, even following very short exposure periods. This study suggests that important ultrastructural features in cells that have not been visible in TEM images as a result of sample preparation or beam damage can be revealed by a carefully planned and executed X-ray microscopic study. The ability to image hydrated cells with sufficient resolution to reveal subcellular structures via X-ray microscopy will undoubtedly lead to future revelations regarding cellular function that have not been possible previously.

The distribution of structural biopolymers within cell membrane regions of wood samples was determined by soft X-ray microscopy.[249] Spatially resolved C−XANES was used to characterize the organic chemistry within structurally differentiated regions of membranes of tracheid cells of two wood samples. It was demonstrated that the cell membrane structure of oak cells was distinctly different from that of cedar.[249] This study also revealed evidence for beam damage of cellulosic components, as evidenced by hydroxyl eliminations and structural rearrangement of pyranose rings in α-cellulose to hydroxyl-substituted γ-pyrones. It was demonstrated that beam damage could be mitigated by defocusing the beam to 2 μm.

A series of studies have utilized STXM, Ca L-edge, and C K-edge XANES to examine Ca distribution maps in human cartilage,[212] biological calcium phosphates,[232] and calcified human tendon.[230] It was demonstrated that differences in absorption cross section at Ca L-edge preionization and postionization energies along with differences arising from features in the XANES spectra could be combined with pre- and post-C K-edge images to provide a quantitative method for mapping Ca locations in mineralized tissues with a detection limit of 0.1 μg cm^{-2}.[230] A recent study has demonstrated the potential of hard X-ray microscopy and spectromicroscopy for imaging, determining major element (Ca and P) distribution patterns, and collecting Ca chemical state information on bone samples.[250] The study revealed the potential to examine bone mineralization processes

on samples without the need for more traditional staining methods or decalcification.

Spectromicroscopic studies of neural specimens utilizing X-ray secondary-electron emission microscopy (XSEM) examined differential metal partitioning between different types of neurons.[227,228,234,236] These studies reveal localization of metals in rat cerebellar neural culture exposed to Al, Co, and Ni. SXEM conducted at the Al, Ni, and Co L edges revealed that Al does not associate with granule cells, the most common type of neurons, but is selectively accumulated in GABAergic neurons and glial cells. Conversely, Ni and Co are not selectively accumulated, being found equally in glial and granule cells.[227,228,234] A spectromicroscopic study of B distributions in rat brain tumor and healthy tissue conducted at the B K edge provided information relative to the optimization of B neutron capture therapy.[239] Not surprisingly, B was more highly localized in tumor compared to healthy tissue; however, the distribution of B in the tumor was found to be inhomogeneous, with significant fluctuations in B concentrations visible between regions separated by only tens of micrometers.[239]

Hard X-ray microprobe analysis of biological samples is becoming quite common for trace element analysis as well as for collecting spatially resolved chemical state information. One major obstacle to widespread application of hard X-ray microprobes to biosciences has been the limitations in lateral resolution. While 0.8−1 μm resolution is becoming commonly achieved at third-generation synchrotron X-ray sources, many applications in the biosciences require much greater spatial resolution for which hard X-ray microprobes offer unique complementary capabilities. Soft X-ray microscopy and spectromicroscopic studies conducted on biological samples to date have demonstrated the capabilities of these techniques for providing high-resolution images and, especially, images based on heterogeneously distributed chemical state differences at a lateral spatial resolution of 100 nm or better. The ability to examine hydrated samples, often without harsh pretreatments, along with the potential to conduct dynamic experiments with such high element and chemical state specificity suggests that these techniques will continue to gain popularity as important research tools in the biosciences.

C. Material and Polymer Sciences

Knowledge on the chemical composition and chemical as well as topological heterogeneity of interfaces is critical in a wide range of material science applications such as optics, catalysis, and microelectronics. Additionally, compositional heterogeneity is a critical parameter controlling bulk and surface properties of polymers, ceramics, and other composite materials.

Important early applications of hard X-ray microprobes included the determination of trace element contamination on the surface of and distribution of doping materials within semiconductors,[54] and this remains an important industrial application of hard X-ray microprobes.[18] A recent study utilized micro-XAFS along with elemental mapping by micro-SXRF

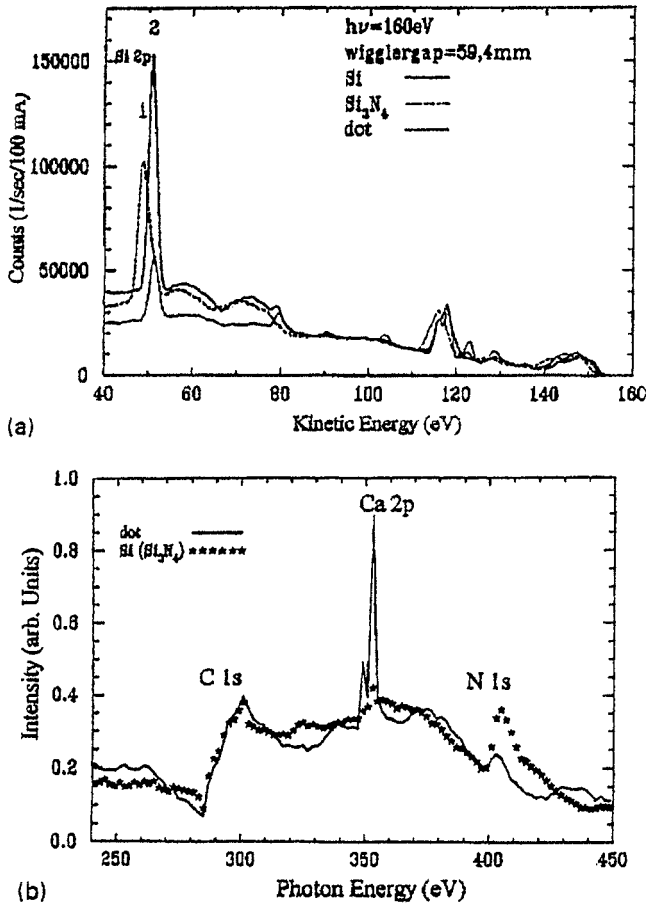

Figure 16. (a) Photoelectron energy distribution curves ($h\nu = 160$ eV) and (b) total electron yield excitations spectra of Si, Si_3N_4, and impurity.[75] (Reprinted with permission from ref 70. Copyright 1997 Elsevier.)

to determine the distribution and chemical state of impurities in silicon that were correlated to poor solar cell performance.[251] Elemental mapping of B-doped polycrystalline silicon revealed preferential incorporation of submicrometer Cu, Ni, Fe, and Cr precipitates along structural defects identified as dislocations.[251] Using the elemental maps, regions of metal precipitates were located and examined by micro-XANES. The Fe K-edge XANES spectra reveal that the Fe associated with the defects is oxidized, having an average valence state between +2 and +3. The presence of a predominant preedge feature also reveals that the local environment of Fe in the precipitate is characterized by high symmetry, similar to an oxide or silicate phase.[251] Future studies involving Fe micro-EXAFS could resolve unambiguously the nature of the impurity phase.

One of the major limitations of hard X-ray microprobes to many material science applications has been the lack of surface sensitivity. While grazing incidence (GI) SXRF (total-reflection XRF (TXRF) has been successfully employed to greatly enhance surface sensitivity and significantly lower detection limits in SXRF measurements,[18,252] the advantage of high lateral spatial resolution is sacrificed. Recent studies have demonstrated that hard X-ray microprobes operating with a grazing-exit geometry (GE SXRF) for detection of fluorescent X-rays from the sample surface can provide both high lateral spatial

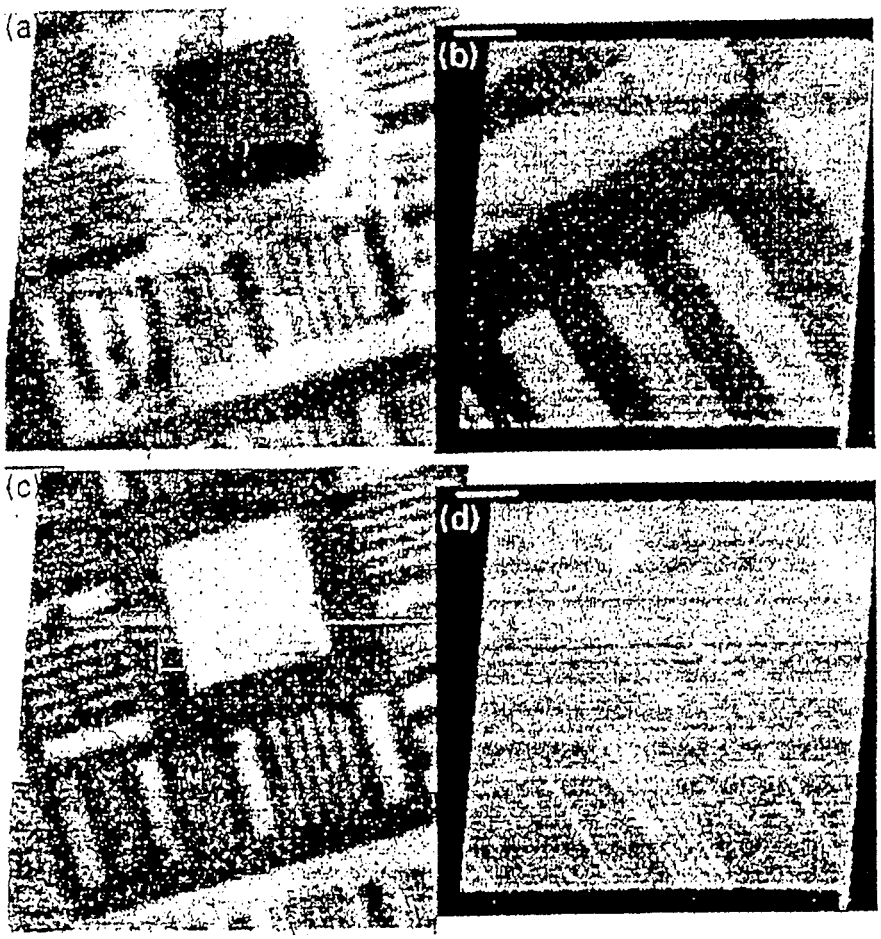

Figure 17. Micrographs of an artificial structure of Si_3N_4 on Si: (a) Si 2p electrons of silicon nitride (peak 1 in Figure 19), $h\nu = 160$ eV. Scale bar: 50 μm.[75] (b) Total electron yield micrograph, $h\nu = 23$ eV. Scale bar: 20 μm. (c) Si 2p electrons of silicon (peak 2 in Figure 19), $h\nu = 160$ eV. Scale bar: 50 μm. (d) Reflected and scattered VUV light, $h\nu = 23$ eV. Scale bar: 20 μm. (Reprinted with permission from ref 70. Copyright 1997 Elsevier.)

resolution with the surface sensitivity achieved with GI SXRF.[87,253,254] The attractiveness of this approach is that spatially resolved surface-sensitive XRD and XAFS can also be conducted using this configuration.[254] This will undoubtedly be an important development in future applications of hard X-ray microprobes that will not be limited to just material and polymer science applications but very useful in the earth, environmental, and biosciences as well.

Other applications of hard X-ray microprobes to material and polymer sciences have included the characterization of polyethelyne polymerization particles to understand catalyst fragmentation and polymerizing particle agglomeration during polymerization.[255] Additionally, characterization of the physicochemical composition of salt layers formed during anodic dissolution of stainless steel,[256] characterization of the orientation distribution of crystal grains in polycrystalline metal alloys,[257] the composition and microstructure of metal oxide films,[12] and the location of trace impurities in synthetic diamonds have been examined with hard X-ray microprobes.[258] Elemental mapping of synthetic diamonds by micro-SXRF reveal that Co and Ni are preferentially accumulated into the {111} growth sector and that Ni is much more highly preferred in the lattice of the {111} growth sector compared to Co.[241] Micro-XANES at the Co and Ni K edges reveal predominant preedge features for both transition metals, features not present in for these metals in the original solvent. The preedge peak results from forbidden 1s $\rightarrow$ 3d electron transitions which derive allowed character from p and d orbital mixing, suggesting a symmetrical 4-fold coordination environment. The high symmetry of the bonding environments for both Co and Ni was attributed to occupancy of interstitial or substitutional tetrahedral sites in the diamond lattice.[258]

Since the pioneering studies demonstrating the feasibility of soft X-ray microscopy and spectromicroscopy for imaging and providing chemical state information on various bulk materials and associated surfaces,[29,45−47,49,50,65] there has been an explosion in applications in the material[41,49,70,85,116,117,121,218,259−271] and in the polymer[51,56,76,82,229,272−294] sciences. Many applications in material and polymer sciences do not require that samples be examined in a hydrated state; thus, UHV conditions are often conducive, allowing surface-sensitive XPS and electron yield detection for imaging (XSEM) and XAFS spectroscopy. The advantage of using a soft X-ray microscope for examining heterogeneous surfaces compared to more conventional electron microprobe techniques is the greatly reduced beam damage[295] and the elemental and molecular specificity achieved. Additionally, the highly polarized nature of synchrotron radiation

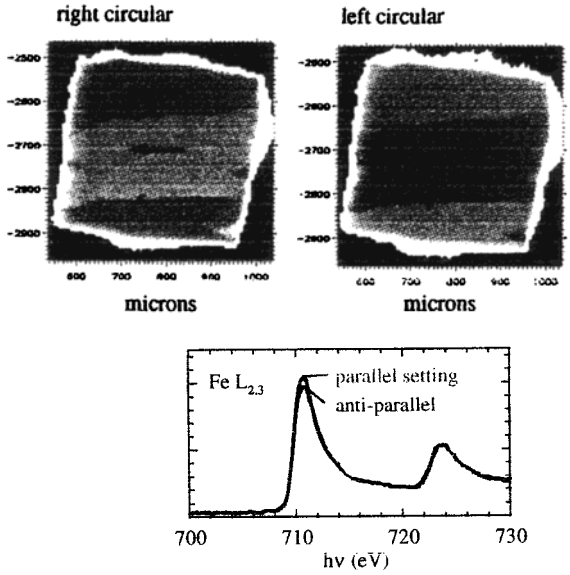

Figure 18. Magnetic contrast has been achieved using transmission Fe films as a resonant circular polarizers in the incident beam at the L3 white line (708 eV) where magnetic circular dichroism is maximum. The polarizer can be flipped parallel or antiparallel to the longitudinal magnetization vector of the sample. Domains are observed in demagnetized Fe films mounted in STXM with normal at 35° to the incident photons. (Reprinted with permission from ref 85. Copyright 1998 American Institute of Physics.)

has been exploited to provide contrast based on molecular orientation[51,76,273,277,279] and also to probe magnetic domains in magnetic materials.[41,85,121,261,268]

Using the chemical shift (~2 eV) of the Si 2p binding energy in the photoelectron spectra of Si_3N_4 relative to Si (Figure 16), a distribution map of Si_3N_4 on a Si chip was generated by the difference in TEY at 23 eV (Figure 17).[70] The TEY excitation spectra of dark regions appearing in parts a−c of Figure 17 revealed the presence of Ca and Na impurities (Figures 16 and 17). An example of an image generated using magnetic circular dichroism (MCD) for absorption contrast is presented in Figure 18.[85] The image of demagnetized Fe films generated with circular polarizers placed parallel and antiparallel in the incident beam at the Fe L edge reveals specific magnetic domains on the order of 26 nm in thickness.[85] Characterization of a number of surfaces relevant to catalysis, microelectronics, optics, etc., by soft X-ray microscopy and spectromicroscopy have been reported and demonstrated the ability to characterize thin films, supports, impurities, and defect structures at high spatial resolution with chemical and magnetic specificity[41,49,70,85,116,117,121,218,259−267,269−271] not possible using other techniques.

Recently, soft X-ray spectromicroscopy has been applied to solid-stabilized emulsions.[266] STXM of hydrated oil−water emulsions containing negatively charged clay minerals and positively charged Ca/Al layered double-hydroxide (LDH) particles collected at the C K and Ca L edges revealed that the emulsions were stabilized by particle heterocoagulate cages surrounding the oil droplets.[266] This study demonstrates the utility of STXM for examining coloidal

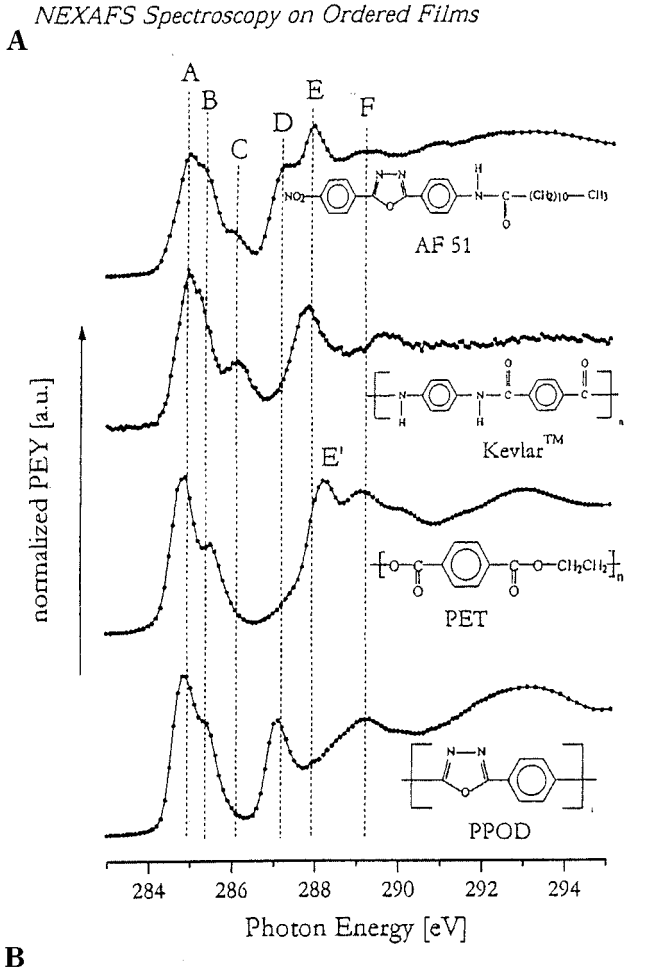

resonance	energy (eV)	assignment
A	285.0	$\pi^*_{C=C}$, phenyl
B	285.3	$\pi^*_{C=C}$, phenyl
C	286.1	$\pi^*_{C=C}$, phenyl, NO_2 or NH ligand related
D	287.3	$\pi^*_{C=N}$, oxadiazole
E	288.0	$\pi^*_{C=O}$, carbonyl

Figure 19. (A) C K-edge X-ray absorption spectra of AF51, Kevlat, PET, PPOD for fingerprinting. (B) Assignment of the resonant features for the C K-edge NEXAFS spectra of the oxadiazole molecule. (Reprinted with permission from ref 285. Copyright 1999 American Chemical Society.)

systems needing to remain fully hydrated. Other interesting applications of soft X-ray microscopy have included studies examining heteroepitaxial growth of thin films and the role of coabsorbed surfactants on controlling or directing epitaxial growth modes,[267] imaging the initial steps of the spreading process on MoO_3 cyrstals on an alumina support surface which is a model catalyst used in petrochemistry,[269] and the determination of the coherently diffracting volume, local dislocation density, residual stress, local fluctuation of residual stress, and intragranular misorientation from single grains of steel.[270]

From the initial commissioning, it was clear that soft X-ray microscopes would emerge as an indispensable tool in polymer science.[29,273] Carbon K-edge XANES is particularly useful in differentiating saturated from unsaturated bonding. Unsaturated C bonding involves π bonds and thus electron excitation from core levels into unoccupied π^* orbitals that

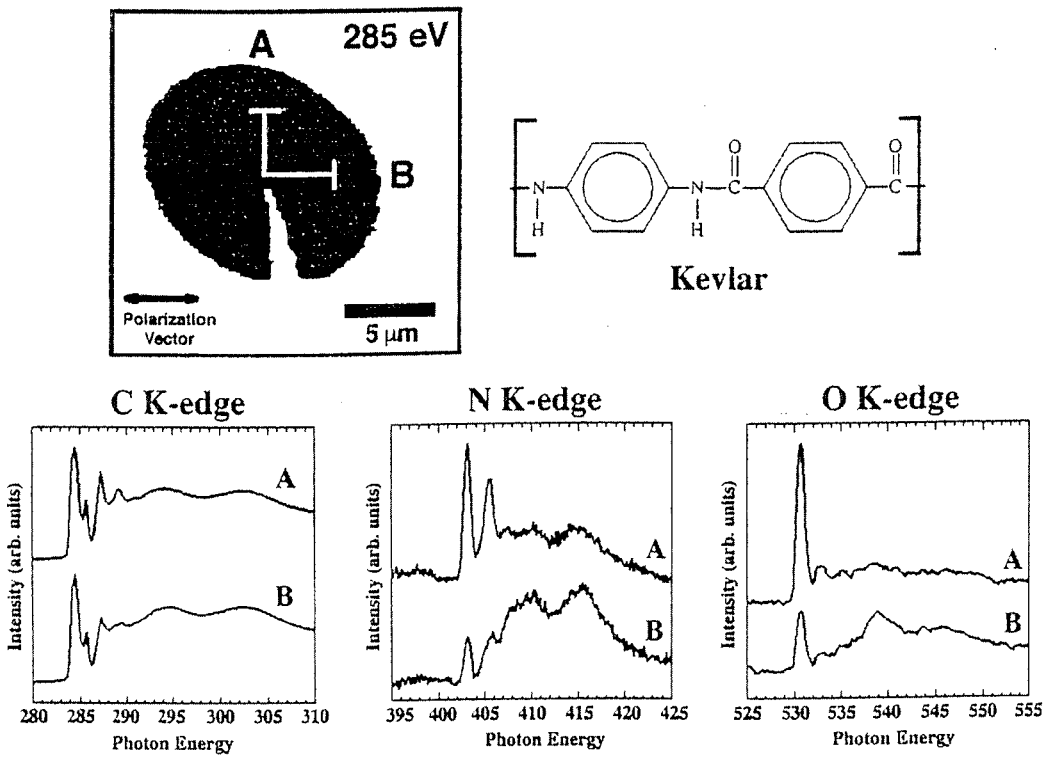

Figure 20. Sectioned Kevlar fibers have been imaged to demonstrate the polarization sensitivity of STXM. The photon *E* vector is horizontal. The π^* orbitals are oriented preferentially radially, and this is reflected in the changing ratio of π to 0 absorption, especially in the case of nitrogen, which occupies unique sites. (Reprinted with permission from ref 85. Copyright 1998 American Institute of Physics.)

produce narrow and intense features in the XANES spectra. Fingerprint C K-edge XANES spectra are generated for individual polymers based on specific resonant features as illustrated in Figure 19.[285] Using weighted linear combination of the XANES spectra for each component, it is then possible to generate high spatial resolution maps of multicomponent polymer blends used to examine morphological features, spatially variable composition, and phase separation phenomena.[29,274−276,280−283,285−291,293,294] The information generated by soft X-ray microscopy and spectromicroscopy is allowing for the identification of the critical factors controlling miscibility of polymers in blends and for optimizing strategies to improve the compatibility of polymers and minimize the degree of phase separation.[288] In addition to utilizing chemical contrast in C K-edge XANES spectra for generating images, preferred orientation of polymer chains has also been used to provide contrast in images of polymer fibers.[76] An example is illustrated in Figure 20, where sectioned Kevlar fibers are imaged at the O and N K edges with the polarization vector horizontal. The fibers display a butterfly pattern when imaged with linearly polarized photons. The polymer chains point along the fibers, and thus, the aromatic rings and carbonyl groups are preferentially oriented in the radial direction with the result that π^* orbitals are all preferentially tangential. Thus, C, O, and N 1s electrons can be excited preferentially in this direction, consistent with the absorption intensities for perpendicular (A) vs parallel (B) orientation of the O and N K-edge XANES spectra in Figure 20.[76,85] Using this approach, Smith and Ade[76] were able to quantify the degree of orientation for the O and N atoms in the Kevlar fibers due to their unique sites in the molecule.

Another interesting application of soft X-ray microscopy to the study of polymers involved the in situ collection of C K-edge XANES spectra of polymethyl methacrylate (PMMA) samples prepared via different methods during exposure to X-rays.[272] The chemical changes in PMMA on exposure included the loss of ester group (C═O) functional groups corresponding to chain scission with the concomitant formation of C═C bonds associated with cross linking. These structural rearrangements were followed quantitatively from changes in respective π^* resonant peaks as a function of radiation dose over time. On the basis of the dose dependence of scission and linking, quantitative prediction of resist performance at different doses for differentially prepared samples is possible, thus enabling the determination of optimum exposure and polymer preparation conditions.[272]

A polarized C K-edge and O K-edge XANES spectroscopic investigation of the polymers PBT and PET and their model compounds was used to reexamine previous spectral assignments.[279] On the basis of the polarization dependence, the peaks previously assigned to a C 1s $\rightarrow$ π^* (ring) or π^* (ring/C═O) excitation at 289.8 eV and an O 1s $\rightarrow$ 3p/Ryberg or π^* (C═O) transition at 536.4 eV were reassigned to a C 1s $\rightarrow \sigma^*$(O−CH_x) transition and an O 1s $\rightarrow \sigma^*$(O−CH_x) transition, respectively. While C XANES spectra are extremely complex, a number of recent studies[274,279,286] have demonstrated significant progress in peak assignments for model compounds and polymers which should help interpretation and aid

in the quantitative analysis of spectra from complex polymer blends.

It is clear that soft X-ray microscopy and spectromicroscopy are powerful tools for characterizing polymers and polymer blends for a variety of applications and that these techniques will continue to gain popularity in the future. A number of recent studies have demonstrated that these techniques are becoming commonly employed in the field of polymer science.[274,279,281,285−288,290]

D. Miscellaneous Applications

There are a number of interesting applications of X-ray microprobes that do not fit well into the disciplinary categories discussed above (or that are relevant to all), although the experimental approaches and the nature of the samples are quite similar. Anderson et al.[296] measured diffusion coefficients in multicomponent solutions with and without HBr using micro-SXRF. While there a number of methods available to measure diffusion coefficients, it is difficult to measure them in solutions containing multiple ions, where concentrations of all components must be measured simultaneously and where there is also a need for spatial resolution. Using micro-SXRF, the concentrations of Cu, Co, and Zn were measured every 300 s over a 3 h period in an aqueous gel in a 35 μm region, 1.45 mm from an interface with a solution of constant composition. Following this, measurements were made at 100 μm intervals from the interface to a 6 mm depth to generate Co, Cu, and Zn distribution maps. In the absence of HBr, the diffusion coefficients of the three transition metals compare well with other measurements, e.g., 1.05×10^{-5} cm^2 s^{-1} for Co.[296] In the presence of HBr, however, the diffusion of the transition metals was observed to be retarded as a result of the simultaneous diffusion of the proton, which because of its high mobility establishes an electrostatic diffusion field that retards the diffusion of the other metals.

Various methods for de-acidifying high acid paper as a means of conserving important paper documents were evaluated by measuring elemental distributions which can serve as an indicator of the efficacy of individual processes.[297] Micro-SXRF measurements were used to reconstruct Ca, Ti, Fe, Cu, and Zn concentration profiles in paper de-acidified by a variety of methods. Calcium distributions within the paper were found to vary significantly as a function of treatment, and the heterogeneous distributions were attributed to the relative effectiveness of the various treatments. For example, higher concentrations and less variation in a distribution of Ca within the paper was observed for an alcohol wash solution compared to a water wash solution. This suggests that the alcohol wash treatment is more effective at delivering more $Ca(OH)_2$ and more uniformly within the paper to more effectively neutralize the acid levels.[297]

Another important application of micro-SXRF that has only begun to emerge in the past five years is the examination of historical artifacts, art, fossils, and other samples of archaeological significance.[10,14,298−302] Micro-SXRF is an ideal method for examining such samples because of the nondestructive nature, because it is fast and multielemental and extremely sensitive, and because there is often the need to examine very small samples or to examine spatial heterogeneity within samples.[301] A wide range of samples have been examined by micro-SXRF in recent years, including dental calculi from an archaeological site,[298] 1900 year old Roman glass fragments,[299,302] Chinese porcelain,[10] Petrified wood,[14] fossilized bone,[300] corroded coins,[301] statues,[301] and ink on historical documents.[301] These studies have demonstrated that trace element analysis and elemental distributions determined by micro-SXRF can provide important complementary information on such topics as palaeonutrition, mechanisms involved in Petrification of wood, palaeoenvironments during fossilization, and dating and authentication of art and artifacts. We anticipate that micro-SXRF will continue to gain popularity as an analytical tool in archaeology and for forensic studies requiring high sensitivity and spatial resolution.

IV. Summary and Future Outlook

Advances in optics and detectors coupled to the commissioning of high-brilliance third-generation hard and soft X-ray sources worldwide have resulted in major advances in the capabilities of X-ray microprobes and microscopes. Submicrometer lateral resolution is becoming routine for hard X-ray microprobes with unprecedented photon fluxes. Likewise, sub-100 nm lateral resolution is becoming routine for soft X-ray microscopes, and various measurement strategies and specialized sample chambers are expanding the range of samples that can be examined. Over the past decade, especially in the past five years, synchrotron-based X-ray microprobes and microscopes have moved from being exotic techniques to techniques that are commonly employed for the characterization of complex natural and synthesized materials. These techniques are also providing unprecedented opportunities to examine samples and follow reactions under ambient conditions that are not accessible with more traditional imaging and spectroscopic methods. We expect that this trend will continue, particularly as more beamlines are commissioned at third-generation sources.

There are a number of techniques that were not covered in this review that are greatly enhancing the capabilities of X-ray microprobes for the characterization of complex heterogeneous materials. Micro-X-ray diffraction (XRD) capabilities are becoming common on many X-ray microprobes,[80,240,303−310] allowing for SXRF imaging, micro-XAFS, spectromicroscopy, and micro-XRD in the same micrometer-sized regions within a sample. Micro-XRD maps can also be constructed from two-dimensional intensity contours.[306] Such an approach has also been used with a STXM to obtain phase and amplitude images of objects with a spatial resolution of $\sim$45 nm.[69]

Another very powerful technique that is developing rapidly, especially at third-generation synchrotron radiation sources, is X-ray tomography.[11,311] The technique expands on the normal X-ray microprobe where a sample, in addition to being rastered in the

X and *Y* directions, is also rotated 360°. This enables three-dimensional microscopic images to be obtained nondestructively on relatively large samples, with similar spatial resolution achieved on the X-ray microprobe. Imaging can be conducted with white light as well as with monochromatic radiation. In principle, spectromicroscopy can be conducted in three dimensions using this approach. This capability will greatly enhance the ability to study complex samples to examine interior pore structures, inclusions, secondary phases, and other features within the sample without the need for sectioning.

Diffraction anomalous fine structure (DAFS) spectroscopy which provides site-selective XAFS-like data through resonant X-ray scattering or diffraction also provides significant potential for characterizing microregions in complex samples.[21,312] Finally, a recent development that may hold potential for future X-ray microprobes involves collection of XRF images using microchannel plate (MCP) relay optics.[84] In this application, the whole sample is irradiated and the fluorescent X-rays are focused onto a CCD by a MCP. This would allow for rapid generation of SXRF images of large samples. If the system could be used with a monochromator, it could provide for full XAFS spectra to be collected at each pixel simultaneously. While there are certainly a number of challenges with collecting high-quality XAFS data in this manner, the possibilities for characterizing complex heterogeneous samples are intriguing.

The ability to examine complex samples with high spatial resolution and chemical specificity with minimal sample manipulation is critical to detailed materials characterization. While X-ray microprobes and microscopes are not appropriate for every application, they do provide the ability to characterize many samples in a way not possible using more conventional microprobe methods. For the most demanding samples that need to be examined wet and under ambient pressure, few methods provide the versatility, the spatial resolution, and the molecular-level information provided by X-ray microscopy, micro-SXRF, micro-XAFS, and spectromicroscopy. We anticipate that these techniques will become mainstream analytical, imaging, and spectroscopic tools in a number of scientific fields over the next decade.

V. Acknowledgments

This research was partially supported by Financial Assistance Award DF-FC09-96SR 18546 from the U.S. Department of Energy to the University of Georgia Research Foundation. We thank Jessica Coughlin, Louise Zweifel, Laura Janecek, and Jennifer Derrick for their assistance and Dr. Carl Strojan for reviewing an earlier version of this manuscript as well as four anonymous reviewers whose critical suggestions greatly improved the organization and clarity of the manuscript.

VI. References

(1) Gordon, B. M.; Hanson, A. L.; Jones, K. W.; Pounds, J. G.; Rivers, M. L.; Schidlovshy, G.; Spanne, P.; Sutton, S. R. *Nucl. Instrum. Methods Phys. Res., Sect. B* **1990**, 527−531.
(2) Jones, K. W.; Gordon, B. M. *Anal. Chem.* **1989**, *61*, 341−358.
(3) Tuniz, C.; Zanini, F.; Jones, K. W. In *Nuclear Instruments and Methods in Physics Research*; Elsevier Science Publishers B.V.: North Holland, 1991; Vol. B56/57.
(4) Sutton, S. R.; Rivers, M. L.; Bajt, S.; Jones, K. W. In *Nuclear Instruments and Methods in Physics Research*; Elsevier Science Publishers B.V.: North Holland, 1993; Vol. B75.
(5) Sutton, S. R.; Rivers, M. L.; Bajt, S.; Jones, K. W.; Smith, J. V. In *Nuclear Instruments and Methods in Physics Research*; Elsevier Science Publishers B.V.: North Holland, 1994; Vol. A, p 347.
(6) Janssens, K.; Vincze, L.; Rubio, J.; F., A. *J. Anal. At. Spectrom.* **1994**, *9*, 151−157.
(7) Torok, S.; Faigel, G.; Jones, K. W.; Rivers, M. L.; Sutton, S. R.; Bajt, S. *X-Ray Spectrom.* **1994**, *23*, 3−6.
(8) Smith, J. V. *Analyst* **1995**, *120*, 1231−1245.
(9) Haller, M.; Knochel, A. *J. Trace Microprobe Tech.* **1996**, *14*, 461−488.
(10) Janssens, K.; Vincze, L.; Vekemans, B.; Aerts, A.; Adams, F.; Jones, K. W.; Knochel, A. *Mikrochim. Acta* **1996**, *13*, 87−115.
(11) Smith, J. V.; Rivers, M. L. In *Microprobe techniques in the Earth Sciences*; Potts, P. J., Bowles, J. F. W., Reed, S. J. B., Cave, M. R., Eds.; Chapman and Hall: London, 1994.
(12) Perry, D. L.; Thompson, A. C.; Russo, R. E.; Mao, X. L.; Chapman, K. L. *Appl. Spectrosc.* **1997**, *51*, 1781−1783.
(13) Hinton, R. W. *Analyst* **1997**, *122*, 1187−1192.
(14) Kuczumow, A.; Vekemans, B.; Schalm, O.; Dorrine, W.; Chevallier, P.; Dillmann, P.; Ro, C.-U.; Kanssens, K.; Grieken, R. V. *J. Anal. At. Spectrom. 1999*, **14**, 435−446.
(15) Ortner, H. M.; Hoffman, P.; Stadermann, F. J.; Weinbruch, S.; Wentzel, M. *Analyst* **1998**, *123*, 833−842.
(16) Ellis, A. T.; Potts, P. J.; Holmes, M.; Oliver, G. J.; Streli, C.; Wobrauschek, P. *J. Anal. At. Spectrom.* **1997**, *12*, 461R−490R.
(17) Janssens, K.; Vincze, L.; Adams, F.; Jones, K. W. *Anal. Chim. Acta* **1993**, *283*, 98−119.
(18) Torok, S. B.; Labar, J.; Schmeling, M.; Grieken, R. E. V. *Anal. Chem.* **1998**, *70*, 495R−517R.
(19) Vekemans, B.; Janssens, K.; Vincze, L.; Aerts, A.; Adams, F.; Hertogen, J. *X-Ray Spectrom.* **1997**, *26*, 333−346.
(20) Lu, F.-Q.; Smith, J. V.; Sutton, S. R.; Rivers, M. L.; Davis, A. M. *Chem. Geol.* **1989**, *75*, 123−143.
(21) Schulze, D. G.; Bertsch, P. M. In *Advances in Agronomy*; Academic Press Inc.: San Diego, 1995; Vol. 55.
(22) Vekemans, B.; Janssens, K.; Vinczw, L.; Adams, F.; Van Espen, P. *X-Ray Spectrosc.* **1994**, *23*, 278−285.
(23) Vincze, L.; Janssens, K.; Adams, F. *Spectrochim. Acta* **1995**, *50B*, 127−147.
(24) Vekemans, B.; Janssens, K.; Vincze, L.; Adams, F.; Van Espen, P. *Spectrochim. Acta* **1995**, *50B*, 149−169.
(25) Vincze, L.; Janssens, K.; Adams, F.; Jones, K. W. *Spectrochim. Acta* **1995**, *50B*, 1481−1500.
(26) Vincze, L.; Janssens, K.; Vekemans, B.; Adams, F. *Spectrochim. Acta* **1999**, *54* (12), 1711−1722.
(27) Somogyi, A.; Vincze, L.; Janssens, K.; Vekemans, B.; Rindby, A.; Adams, F. *Spectrochim. Acta* **2000**, *55B* (1), 75−89.
(28) Figueiredo, M. O.; Ramos, M. T.; Pereira da Silva, T.; Basto, M. J.; Chevallier, P. *X-Ray Spectrosc.* **1999**, *28*, 251−254.
(29) Ade, H.; Zhang, X.; Cameron, S.; Costello, C.; Kirz, J.; Williams, S. *Science* **1992**, *258*, 972−974.
(30) Chevallier, P.; Dhez, P.; Erko, A.; Firsov, A.; Legrand, F.; Populus, P. *Nucl. Instrum. Methods Phys. Res. B* **1996**, *113*, 122−127.
(31) Sie, S. H. *Nucl. Instrum. Methods Phys. Res. B* **1997**, *130*, 592−607.
(32) Jacobsen, C.; Ade, H.; Kirz, J.; Ko, C.-H.; Williams, S.; Zhang, X.; Anderson, E.; Kern, D. *Inst. Phys. Conf. Ser.* **1992**, *130*, 571−576.
(33) Vincze, L.; Janssens, K.; Adams, F.; Rindby, A. *X-Ray Spectrom.* **1995**, 24, 27−37.
(34) Sanchez, H. J.; Perez, C. A. J. *Trace Microprobe Tech.* **1998**, *16*, 501−512.
(35) Jindong, X.; Yejun, H.; Xunliang, D.; Qiuli, P.; Yiming, Y. J. *Anal. At. Spectrom.* **1999**, *14*, 391−394.
(36) Schoonover, J. R.; Havrilla, G. J. *Appl. Spectrosc.* **1998**, *53*, 257−265.
(37) Buckley, C. J.; Burge, R. E.; Foster, G. F.; Rivers, M. L.; Ali, S. y.; Scotchford, C. A. *Inst. Phys. Conf.* **1992**, *130*.
(38) Wegrzynek, D.; Hloynska, B.; Ostacchowicz, J. *X-Ray Spectrosc.* **1999**, *28*, 209−214.
(39) Bertsch, P. M.; Schulze, D. G. In *Synchrotron X-ray Methods in Clay Science*; Schulze, D. G., J. W. S., Bertsch, P. M., Eds.; The Clay Minerals Society: Boulder, CO, 1999.
(40) Sayre, D.; Chapman, H. N. *Acta Crystallogr., Sect. A* **1995**, *A51*, 237−252.
(41) Swiech, W.; Fecher, G. H.; Ziethen, C.; Schmidt, O.; Schonhense, G.; Grzelakowski, K.; Schneider, C. M.; Fromter, R.; Oepen, H. P.; Kirschner, *J. Electron Spectrosc. Relat. Phenom.* **1997**, *84*, 171−188.

(42) Chapman, H. N.; Jacobsen, C.; Williams, S. *Ultramicroscopy* **1996**, *62*, 191−213.
(43) Buckley, C.; Rarback, R.; Alforque, R.; Shu, D.; Ade, H.; Hellman, S.; Iskander, N.; Kirz, J.; Lindaas, S.; McNulty, I.; Oversluizen, M.; Tang, E.; Attwood, D.; DiGennaro, R.; Howells, M.; Jacobsen, C.; Y., V.; Rothman, S.; Kern, D.; Sayre, D. *Rev. Sci. Instrum.* **1989**, *60*, 2444−2447.
(44) Tonner, B. P. a. D. D. In *Nuclear Instruments & Methods in Physics Research*; Elsevier Science B.V.: North Holland, 1994; Vol. A, p 347.
(45) Ade, H.; Kirz, J.; Hulbert, S. L.; Johnson, E. D.; Anderson, E.; Kern, D. *Appl. Phys. Lett.* **1990**, *56*, 1841−1843.
(46) Tonner, B. P.; Harp, G. R. *J. Vac. Sci. Technol.* **1989**, *A71*, 1−4.
(47) Ade, H. W. *Nucl. Instrum. Methods Phys. Res.* **1992**, *A319*, 311−319.
(48) Iida, A.; Noma, T.; Hayakawa, S.; Takahashi, M.; Gohshi, Y. *Appl. Phys.* **1992**, *32*, 160−164.
(49) Ade, H.; Ko, C.-H.; Johnson, E. D.; Anderson, E. In *Surface and Interface Analysis*; Ade, H., C. H. K., Johnson., E. D., Eds.; John Wiley & Sons Ltd.: West Sussex, 1992; Vol. 19, pp 1−12.
(50) Kirz, J.; Ade, H.; Jacobsen, C.; Ko, C.-H.; Lindaas, S.; McNulty, I.; Sayre, D.; Williams, S.; Zhang, X.; Howells, M. *Rev. Sci. Instrum.* **1992**, *63*, 557−563.
(51) Williams, S.; Jacobsen, C.; Kirz, J.; Maser, J.; Sue Wirick; Zhang, X.; Ade, H.; Rivers, M. *Rev. Sci. Instrum.* **1995**, *66*, 1271−1275.
(52) Bilderback, D. H.; Thiel, D. J. *Rev. Sci. Instrum.* **1995**, *66*, 2059−2063.
(53) Aristov, V. V.; Basov, Y. A.; Hartman, Y. M.; Riekel, C.; Snigirev, A. A. Inst. Phys. **1992**, *130*, 523−526.
(54) Thompson, A. C.; Chpamna, K. L.; Ice, G. E.; Sparks, C. J.; Yun, W.; Lai, B.; Legnini, D.; Vicarro, P. J.; Rivers, M. L.; Bilderback, D. H.; Thiel, D. J. *Nucl. Instrum. Methods Phys. Res.* **1992**, *A319*, 320−325.
(55) Tuniz, C.; Devoti, R.; Santoro, G.; Zanini, F. *Nucl. Instrum. Methods Phys. Res.* **1990**, *B50*, 338−342.
(56) Kirz, J.; Ade, H.; Anderson, E.; Buckley, C.; Chapman, H.; Howells, M.; Jacobsen, C.; Ko, C.-H.; Lindaas, S.; Sayre, D.; Williams, S.; Wirick, S.; Zhang, X. *Nucl. Instrum. Methods Phys. Res.* **1994**, *B87*, 92−97.
(57) Hwu, Y.; Tung, C. Y.; Pieh, J. Y.; Lee, S. D.; Almeras, P.; Gozzo, F.; Berger, H.; Margaritondo, G.; De Stasio, G.; Mercanti, D.; Ciotti, M. T. *Nucl. Instrum. Methods Phys. Res.* **1995**, *A361*, 349−353.
(58) Chevallier, P.; Dhez, P.; Legrand, F.; Erko, A.; Agafonov, Y.; Panchenko, L. A.; Yakshin, A. *Trace Microprobe Tech.* **1996**, *14*, 517−539.
(59) Ice, G. E. *X-Ray Spectrom.* **1996**, *26*, 315−326.
(60) Fink, R.; Weiss, M. R.; Umbach, E.; Preikszas, D.; Rose, H.; Spehr, R.; Hartel, P.; Engel, W.; Degenhardt, R.; Wichtendahl, R.; Kuhlenbeck, H.; Erlebach, W.; Ihmann, K.; Schlogel, R.; Freund, H. J.; Bradshaw, A. M.; Lilienkamp, G.; Schmidt, T.; Bauer, E.; Bener, G. *J. Electron Spectrosc. Relat. Phenom.* **1997**, *84*, 231−250.
(61) Hoffman, S. A.; Thiel, D. J.; Bilderback, D. H. *Opt. Eng.* **1994**, *33*, 303−306.
(62) Hoffman, S. A.; Thiel, D. J.; Bilderback, D. H. In *Nuclear Instruments & Methods in Physics Research*; Elsevier: North Holland, 1994; Vol. A.
(63) Xiao, Q. F.; Ponomarev, I. Y.; Kolomitsev, A. I.; Gibson, D. M.; Dilmanian, F. A.; Nachaliel, E. In *Nuclear Instruments & Methods in Physics Research*; Elsevier Science B.V.: North Holland, 1994; Vol. A, p 347.
(64) Janssens, K.; Vincze, L.; Vekemans, B.; Adams, F.; Haller, M.; Knochel, A. *J. Anal. At. Spectrom.* **1998**, *13*, 339−350.
(65) Tonner, B. P.; Harp, G. R.; Koranda, S. F.; Zhang, J. *Rev. Sci. Instrum.* **1992**, *63*, 564−568.
(66) Snigirev, A. *Rev. Sci. Instrum.* **1995**, *66*, 2053−2058.
(67) Chevallier, P.; Dhez, P.; Legrand, F.; Idir, M.; Soullie, G.; Mirone, A.; Erko, A.; Snigirev, A.; Snigireva, I.; Suvorov, A.; Freund, A.; Engstrom, P.; Nielsen, J. A.; Grubel, A. *Nucl. Instrum. Methods Phys. Res.* **1995**, *A354*, 584−587.
(68) Ko, C.-H.; Janos, K. *Rev. Sci. Instrum.* **1995**, *66*, 1416−1418.
(69) Chapman, H. N. *Ultramicroscopy* **1996**, *66*, 153−172.
(70) Voss, J. *J. Electron Spectrosc. Relat. Phenom.* **1997**, *84*, 29−44.
(71) Chen, C. T. *J. Electron Spectrosc. Relat. Phenom.* **1998**, *92*, 289−299.
(72) Schmal, G.; Rudolph, D.; Guttman, P.; Schneider, G.; Thieme, J.; Niemann, B. *Rev. Sci. Instrum.* **1995**, *66*, 1282−1286.
(73) Denlinger, J. D.; Rotenberg, E.; Warwick, T.; Visser, G.; Nordgren, J.; Guo, J. H.; Shytt, P.; Kevan, S. D.; McCutcheon, K. S.; Shuh, D.; Bucher, J.; Edelstein, N.; Tobin, J. G.; Tonner, B. P. *Rev. Sci. Instrum.* **1995**, *66*, 1342−1345.
(74) Wang, J. D.; Kagoshima, Y.; Miyahara, T.; Ando, M. *Rev. Sci. Instrum.* **1995**, *66*, 1401−1403.
(75) Suzuki, Y.; Uchida, F. *Rev. Sci. Instrum.* **1995**, *66*, 1468−1470.
(76) Smith, A. P.; Ade, H. *Appl. Phys. Lett.* **1996**, *69*, 3833−3835.
(77) Hirsch, G. *Rev. Sci. Instrum.* **1995**, *66*, 1367−1369.
(78) Hayakawa, S.; Goto, S.; Shoji, T.; Yamada, E.; Gohshi, Y. *J. Synchrotron Radiat.* **1998**, *5*, 1114−1116.
(79) Umbach, E. *Physica B* **1995**, *208/209*, 193−198.
(80) Chevallier, P.; Populus, P. *X-Ray Spectrom.* **1999**, *28*, 348−351.
(81) van Langevelde, F.; Tros, G. H. J.; Bowen, D. K.; Vis, R. D. *Nucl. Instrum. Methods Phys. Res.* **1990**, *B49*, 544−550.
(82) Jacobsen, C.; Wirick, S.; Flynn, G.; Zimba, C. *Microscopy* **2000**, *197*, 173−184.
(83) Kirz, J.; Jacobsen, C.; Lindaas, S.; Williams, S.; Zhang, X.; Anderson, E.; Howells, M. In *Synchrotron Radiation in Biosciences*; Chance, B., D. D., Ebashi, S., Goodhead, D. T., Helliwell, J. R., Huxley, H. E., Iizuka, T., Kirz, J., Mitsui, T., Rubenstein, E., Sakabe, N., Sasaki, T., Schmahl, G., Sturhmann, H., Wuthrich, K., Zaccai, G., Eds.; Oxford University Press: New York, 1994.
(84) Martin, A. P.; Brunton, A. N.; Fraser, G. W.; Holland, A. D.; Keay, A.; Hill, J.; Nelms, N.; Turcu, I. C. E.; Allott, R.; Lisi, N.; Spencer, N. *X-Ray Spectrom.* **1999**, *28*, 64−70.
(85) Warwick, T.; Franck, K.; Kortright, J. B.; Meigs, G.; Moronne, M.; S., M.; Rotenberg, E.; Seal, S.; Steele, W. F. *Rev. Sci. Instrum.* **1998**, *69*, 2964−2973.
(86) Warwick, T.; Ade, H.; Cerasari, S.; Denlinger, J.; Franck, K.; Garcia, A.; Hayakawa, S.; Hitchcock, A.; Kikuma, J.; Klinger, S.; Kortright, J.; Morisson, G.; Moronne, M.; Rightor, E.; Rotenberg, E.; Seal, S.; Shin, H.-J.; Steele, W. F.; Tonner, B. P. *J. Synchrotron Radiat.* **1998**, *5*, 1090−1092.
(87) Iida, A. *X-Ray Spectrom.* **1997**, *26*, 359−363.
(88) Ding, X.; He, Y.; Yan, Y. *X-Ray Spectrom.* **1997**, *23*, 374−379.
(89) Weiss, M. R.; Follath, R.; Senf, F.; Gudat, W. *J. Electron Spectrosc. Relat. Phenom.* **1999**, *101−103*, 1003−1012.
(90) Shin, H.-J.; Chung, Y.; Kim, B. *J. Electron Spectrosc. Relat. Phenom.* **1999**, *101−103*, 985−989.
(91) Barbo, F.; Bertolo, M.; Bianco, A.; Cautero, G.; Fontana, S.; Johal, T. K.; La Rosa, S.; Margaritondo, G. *Rev. Sci. Instrum.* **2000**, *71*, 5−10.
(92) *X-Ray Microscopy*; Werner Meyer-Ilse, T. W., Attwood, D., Eds.; American Institute of Physics: Berkeley, 2000; Vol. 507.
(93) Manceau, A. *Geochim. Cosmochim.* **1995**, *59*, 3647−3653.
(94) Dhez, P.; Chevallier, P.; Lucatorto, T. B.; Tarrio, C. *Rev. Sci. Instrum.* **1999**, *70*, 1907−1920.
(95) Anderson, E.; Kern, D. In *X-ray Microscopy*; Michette, A., G. M., Buckley, C., Eds.; Springer-Verlag: Berlin, 1991; Vol. III.
(96) Kirz, J.; Jacobsen, C.; Howell, M. *Q. Rev. Biophys.* **1995**, *28*, 33−130.
(97) Kirz, J.; Matsushita, T. *Rev. Sci. Instrum.* **1995**, *66*, 1271−1275.
(98) Levine, Z. H. *Appl. Phys. Lett.* **1999**, *74*, 150.
(99) Lai, B.; Yun, W. B.; Legnini, D.; Xiao, Y.; Chrzas, J.; Viccaro, J.; White, P. J.; Bajikar, V.; Denton, S.; Cerrine, F.; DiFabrizio, E.; Gentili, M.; Grella, L.; M., B. *Appl. Phys. Lett.* **1992**, *61*, 1877−1879.
(100) Yun, W.; Pratt, S. T.; Miller, R. M.; Cai, Z.; Hunter, D. B.; Jarstfer, A. G.; Kemner, K. M.; Lai, B.; Lee, H.-R.; Legnini, D. G.; Rodrigues, W.; Smith, C. I. *J. Synchrotron Radiat.* **1998**, *5*, 1390−1395.
(101) Wolter, H. *Ann. Phys.* **1952**, *10*, 94.
(102) Aoki, S.; Takeuchi, A.; Ando, M. *J. Synchrotron Radiat.* **1998**, *5*, 1117−1118.
(103) Hayakawa, S.; Iida, A.; Aoki, S.; Gohshi, Y. *Rev. Sci. Instrum.* **1989**, *60*, 2452.
(104) Spiller, E.; Feder, R.; Topalian, J.; Eastman, D.; Gudat, W.; Sayre, D. *Science* **1976**, *191*, 1172−1174.
(105) Underwood, J. H.; Thompson, A. C.; Kortright, J. B.; Chapman, K. C.; Lundt, D. *Rev. Sci. Instrum.* **1996**, *67*, 3358.
(106) Yang, B. X.; Rivers, M.; Schildkamp, W.; Eng, P. J. *Rev. Sci. Instrum.* **1995**, *66*, 2278−2280.
(107) Duff, M. C.; Hunter, D. B.; Triay, I. R.; Bertsch, P. M.; Reed, D. T.; Sutton, S. R.; Shea-McCarthy, G.; Kitten, J.; Eng, P.; Chipera, S. J.; Vaniman, D. T. *Environ. Sci. Technol.* **1999**, *33*, 2163−2169.
(108) Eng, P. J.; Newville, M.; Rivers, M. L.; Sutton, S. R. In *X-Ray Microfocusing: Applications and Techniques*; Bellingham, WA, 1998; p 145.
(109) Erko, A.; Agafonov, Y.; Panchenko, L. A.; Yakshin, A. *Opt. Commun.* **1994**, *106*, 146−150.
(110) Idir, M.; Mirone, A.; Soullie, G.; Guerin, P.; Ladan, F.; Dhez, P. *Opt. Commun.* **1995**, *119*, 633.
(111) Dhez, P.; Erko, A.; Khzmalian, E.; Vidal, B.; Zinenko, V. *Appl. Opt.* **1992**, *31*, 6662.
(112) Bonse, U.; Riekel, C.; Snigirev, A. A. *Rev. Sci. Instrum.* **1992**, *63*, 622−624.
(113) Heald, S. *J. Phys. IV Fr.* **1997**, C2-297−C2-301.
(114) Bilderback, D. H.; Thiel, D. J.; Pahl, R.; Brister, K. E. *J. Synchrotron Radiat.* **1994**, *1*, 37−42.
(115) Snigireva, I.; Snigirev, A. VI International Conference on X-Ray Microscopy, Berkeley, CA, 1999; pp 76−83.
(116) Margaritondo, G.; Bernstorff, S.; Kiskinova, M.; Prince, K. C.; Santaniello, A.; Tromba, G.; Savoia, A. *Appl. Surf. Sci.* **1998**, *130−132*, 629−638.
(117) Warwick, T.; Ade, H.; Hitchcock, A. P.; Padmore, H.; Rightor, E. G.; Tonner, B. P. *J. Electron Spectrosc. Relat. Phenom.* **1997**, *84*, 85−98.

(118) Marsi, M.; Casalis, L.; Gregoratti, L.; Sunther, S.; Kolmakov, A.; Kovac, J.; Lonza, D.; Kiskinova, M. *J. Electron Spectrosc. Relat. Phenom.* **1997**, *84*, 73−83.
(119) Kunz, C. *Phys. Scr.* **1996**, *T61*, 19−25.
(120) Yamada, T.; Yuri, M.; Onuki, H.; Ishizaka, S. *Rev. Sci. Instrum.* **1995**, *66*, 1493−1495.
(121) Kagoshima, Y.; Miyahara, T.; Ando, M.; Wang, J. D.; Aoki, S. *Rev. Sci. Instrum.* **1995**, *66*, 1534−1536.
(122) Neuhausler, U.; Jacobsen, C.; Schulze, D.; Stott, D.; Abend, S. *J. Synchrotron Radiat.* **2000**, *7*, 110−112.
(123) Tonner, B. P.; Drouby, T.; Dealinger, J.; Ilse-Meyer, W.; Warwick, T.; Rothe, J.; Kneedler, E.; Pecher, K.; Nealson, K.; Grundl, T. *Surf. Interface Anal.* **1999**, *27*, 247−258.
(124) Giauque, R. D.; Thompson, A. C.; Underwood, J. H.; Wu, Y.; Jones, K. W.; Rivers, M. L. *Anal. Chem.* **1988**, *60*, 855−858.
(125) Kuznetsor, S. M.; Snigireva, I. I.; Snigirev, A. A.; Engstrom, P.; Riekel, C. *Appl. Phys. Lett.* **1994**, *65*, 827−829.
(126) Sutton, S. R.; Bajt, S.; Delaney, J.; Schulze, D.; Tokunaga, T. *Rev. Sci. Instrum.* **1995**, *66*, 1464−1467.
(127) Snigirev, A.; Snigireva, I.; Kohn, V.; Kuznetsov, S.; Schelokov, I. *Rev. Sci. Instrum.* **1995**, *66*, 5486−5492.
(128) Iida, A.; Hirano, K. *Nucl. Instrum. Methods Phys. Res.* **1996**, *B114*, 149−153.
(129) Li, Y.; Wong, G. C. L.; Safinya, C. R.; Caine, E.; Hu, E. L.; Haeffner, D.; Fernandez, P.; Yun, W. *Rev. Sci. Instrum.* **1998**, *69*, 2844−2848.
(130) Tamura, S.; Ohtani, K.; Kamijo, N.; Suzuki, Y.; Kihara, H. *Thin Solid Films* **1996**, *281/282*, 243−245.
(131) Kopp, O. C.; Reeves, D. K.; Rivers, M. L.; Smith, J. V. *Chem. Geol.* **1990**, *81*, 337−347.
(132) Lowenstern, J. B.; Mahood, G. A.; Rivers, M. L.; Sutton, S. R. *Science* **1991**, *252*, 1405−1409.
(133) Treiman, A. H.; Sutton, S. R. *Geochim. Cosmochim. Acta* **1992**, *56*, 4059−4074.
(134) Vanko, D. A.; Sutton, S. R.; Rivers, M. L.; Bodnar, R. J. *Chem. Geol.* **1993**, *109*, 125−134.
(135) Skulski, T.; Minarik, W.; Watson, E. B. *Chem. Geol.* **1994**, *117*, 127−147.
(136) Rakovan, J.; Reeder, R. J. *Am. Mineral.* **1994**, *79*, 892−903.
(137) Northrup, P. A.; Reeder, R. J. *Am. Mineral.* **1994**, *79*, 1167−1175.
(138) Mavrogenes, J. A.; Bodnar, R. J.; Anderson, A. J.; Bajt, S.; Sutton, S. R.; Rivers, M. L. *Geochim. Cosmochim. Acta* **1995**, *59*, 3987−3995.
(139) Dalphe, C.; Baker, D. R. *Can. Mineral.* **1995**, *33*, 481−498.
(140) Lanzirotti, A. *Geochim. Cosmochim. Acta* **1995**, *59*, 4105−4110.
(141) Brearley, A. J.; Bajt, S.; Sutton, S. R. *Geochim. Cosmochim. Acta* **1995**, *59*, 4307−4316.
(142) Reeder, R. J. *Geochim. Cosmochim. Acta* **1996**, *60*, 1543−1522.
(143) Mayanovic, R. A.; Anderson, A. J.; Bajt, S. *Physica B* **1995**, *208/209*, 239−240.
(144) Rakovan, J.; Reeder, R. J. *Geochim. Cosmochim. Acta* **1996**, *60*, 4435−4445.
(145) Philippot, P.; Menez, B.; P., C.; Gibert, F.; Legrand, F.; Populus, P. *Chem. Geol.* **1998**, *144*, 121−136.
(146) Figueiredo, M. O.; Silva, T. P.; Basto, M. J.; Ramos, M. T.; Chevallier, P. *J. Anal. At. Spectrom.* **1999**, *14*, 505−507.
(147) Buhn, B.; Rankin, A. H.; Radtke, M.; Haller, M.; Knochel, A. *Am. Mineral.* **1999**, *84*, 1117−1125.
(148) Thomas, K. L.; Blanford, G. E.; Clemett, S. J.; Flynn, G. J.; Keller, L. P.; Klock, W.; Maechling, C. R.; McKay, D. S.; Messenger, S.; Nier, A. O.; Schlutter, D. J.; Sutton, S. R.; Warren, J. L.; Zare, R. N. *Geochim. Cosmochim. Acta* **1995**, *59*, 2797−2815.
(149) Flynn, G. J.; Sutton, S. R. *Meteoritics* **1991**, *26*, 334.
(150) Flynn, G. J.; Keller, L. P.; Jacobsen, C.; Wirick, S. *Meteorit. Planet. Sci.* **1998**, *33*, A50.
(151) Flynn, G. J.; Sutton, S. R.; Kehm, K.; Hoenberg, C. M. *Meteorit. Planet. Sci.* **1998**, *33*, A51.
(152) Flynn, G. J.; Keller, L. P.; Jacobsen, C.; Wirick, S. *Abstract Pap. Am. Chem.* **2000**, S220.
(153) Flynn, G. J.; Keller, L. P.; Jacobsen, C.; Wirick, S.; Bajt, S.; Chapman, H. N. *Meteor. Planet. Sci.* **1997**, *32*, A42.
(154) Flynn, G. J.; Sutton, S. R.; Kehm, K.; Hohenberg, C. M. Meteorites & Planetary Dust Particles from the L2036 Stratospheric Collector; 1997; Vol. 32, A42−A43.
(155) Flynn, G. J.; Sutton, S. R.; Lanzirotti, A. *Meteorit. Planet. Sci.* **2000**, *35*, A54.
(156) Flynn, G. J.; Sutton, S. R. *Meteorit. Planet. Sci.* **1998**, *33*, A49−A50.
(157) Flynn, G. J. *Meteoritics* **1995**, *30*, 505.
(158) Flynn, G. J.; Bajt, S.; Sutton, S. R.; Klock, W. *Meteoritics* **1995**, *30*, 505.
(159) Flynn, G. J.; Sutton, S. R.; Bajt, S.; Klock, W.; Thomas, K. L. *Meteoritics* **1994**, *29*, 4666.
(160) Hayakawa, S.; Gohshi, Y.; Atsuo, I.; Sadao, A.; Sato, K. *Rev. Sci. Instrum.* **1991**, *62*, 2545−2549.
(161) Henderson, C. M. B.; Cressey, G.; Redfern, S. A. T. *Radiat. Phys. Chem.* **1995**, *45*, 459−481.
(162) Morra, M. J.; Fendorf, S. E.; Brown, P. D. *Elsevier Science Ltd.* **1996**, 683−688.
(163) Bajt, S.; Sutton, S. R.; Delaney, J. S. *Geochim. Cosmochim. Acta* **1994**, *58*, 5209−5214.
(164) Bajt, S.; Sutton, S. R.; Delaney, J. S. *Physica B* **1995**, *208/209*, 243−244.
(165) Anderson, A.; Mayanovic, R.; Bajt, S. *Can. Mineral.* **1998**, *33*, 499−508.
(166) Delaney, J. S.; Dyar, M. D.; Sutton, S. R.; Bajt, S. *Geology* **1998**, *26*, 139−142.
(167) Dyar, M. D.; Delaney, J. S.; Sutton, S. R.; Schaeffer, M. W. *Am. Mineral.* **1998**, *83*, 1361−1365.
(168) Bajt, S.; Hanson, A. L. *Rev. Sci. Instrum.* **1995**, *66*, 1502−1504.
(169) Anderson, A. J.; Mayanovic, R. A.; Bajt, S. *Can. Mineral.* **1998**, *36*, 511−524.
(170) Brown, G. E., Jr. In *Mineral-Water Interface Geochemistry*; Hochella, M. F., Jr., White, A. F., Eds.; Mineralogical Society of America: Washington, D.C., 1990; Vol. 23.
(171) Droubay, T.; Mursky, G.; Tonner, B. P. *J. Electron Spectrosc. Relat. Phenom.* **1997**, *84*, 159−169.
(172) Cody, G. D.; Botto, R. E.; Ade, H.; Wirick, S. *Int. J. Coal Geol.* **1996**, *32*, 69−86.
(173) De Stasio, M. D.; Ciotti, M. T.; Droubay, T. C.; Perfetti, P.; Margaritonda, G.; Tonner, B. P. *J. Phys. D: Appl. Phys.* **1996**, *29*, 259−262.
(174) Pecher, K.; Kneedler, E.; Rothe, J.; Meigs, G.; Warwick, T.; Nealson, K.; Tonner, B. X-Ray Microscopy: Proceeding of the Sixth Internation Conference, 2000; pp 291−300.
(175) Botto, R. E.; Cody, G. D.; Ade, H.; Behal, S.; Disko, M.; Wirick, S. *Energy Fuels* **1994**, *8*, 152−154.
(176) Cody, G. D.; Botto, R. E.; Ade, H.; Behal, S.; Disko, M.; Wirick, S. *Energy Fuels* **1995**, *9*, 75−84.
(177) Cody, G. D.; Botto, R. E.; Ade, H.; Behal, S.; Disko, M.; Wirick, S. *Energy Fuels* **1995**, *9*, 525−533.
(178) Cody, G. D.; Ade, H.; Wirik, S.; Mitchell, G. D.; Davis, A. *Org. Geochem.* **1998**, *28*, 441−455.
(179) McKay, D. S.; Gibson, E. K.; Thomaskeprta, K. I.; Vali, H.; Romancek, C. S.; Clemett, S. J.; Chillier, X. D. F.; Maechling, C. R.; Zare, R. N. *Science* **1996**, *273*, 924−930.
(180) Allen, P. G.; Bucher, J. G.; Denecke, M. A.; Edelstein, N. M.; Kaltsoyannis, N.; Nitsche, H.; Reich, T.; Shuh, D. K. In *Synchrotron Radiation Techniques in Industrial, Chemical, and Materials Science*; D'Amico, K. L., Terminello, L. J., Shuh, D. K., Eds.; Plenum Press: New York, 1996.
(181) Kaplan, D. I.; Hunter, D. B., Bertsch; P. M.; Bajt, S.; Adriano, D. C. *Environ. Sci. Technol.* **1994**, *28*, 1186−1189.
(182) Bajt, S.; Clark, S. B.; Sutton, S. R.; Rivers, M. L.; Smith, J. V. *Anal. Chem.* **1993**, *65*, 1800−1804.
(183) Bertsch, P. M.; Hunter, D. B.; Stephen R.; Bajt, S.; Rivers, M. L. *Environ. Sci. Technol.* **1994**, *28*, 980−984.
(184) Bertsch, P. M.; Hunter, D. B.; Nuessle, P. R.; Clark, S. B. *J. Phys. IV Fr.* **1997**, *7*, C2-817−C2-818.
(185) Buck, E. C.; Brown, N. R.; Dietz, N. L. *Environ. Sci. Technol.* **1996**, *30*, 81−88.
(186) Hunter, D. B.; Bertsch, P. M. *Radioanal. Nucl. Chem.* **1998**, *234*, 237−242.
(187) Duff, M. C.; Amrhein, C.; Bertsch, P. M.; Hunter, D. B. *Geochim. Cosmochim. Acta* **1997**, *61*, 73−81.
(188) Duff, M. C.; Hunter, D. B.; Bertsch, P. M.; Amrhein, C. *Biogeochemistry* **1999**, 45, 95−114.
(189) Bender, J.; Duff, M. C.; Phillips, P.; Hill, M. *Environ. Sci. Technol.* **2000**, *34*, 3235−3241.
(190) Fredrickson, J. K.; Zachara, J. M.; Kennedy, D. W.; Duff, M. C.; Gorby, Y. A.; Li, S.-m. W.; Krupa, K. M. In Press.
(191) Duff, M. C.; Newville, M.; Hunter, D. B.; Bertsch, P. M.; Sutton, S. R.; Triay, I. R.; Vaniman, D. T.; Eng, P.; Rivers, M. L. *J. Synchrotron Radiat.* **1999**, *6*, 350−352.
(192) Manceau, A.; Lanson, B.; L., S. M.; Harge, J. C.; Musso, M.; Eybert-Berard, L.; Hazemann, J.-L.; Chateigner, D.; Lamble, G., M. *Am. J. Sci.* **2000**, *300*, 289−343.
(193) Schulze, D. G.; McCay-Buis, T.; Sutton, S. R.; Huber, D. M. *Phytopathology* **1994**.
(194) Schulze, D. G.; Sutton, S. R.; Bajt, S. *Soil Sci. Soc. Am. J.* **1995**, *59*, 1540−1548.
(195) Tokunaga, T. K.; G. E.; Brown, G. E., Jr.; Pickering, I. J.; Sutton, S. R.; Bajt, S. *Environ. Sci. Technol.* **1997**, *31*, 1419−1425.
(196) Tokunaga, T. K.; Sutton, S. R.; Bajt, S. *Soil Sci.* **1994**, *158*, 421−434.
(197) Tokunga, T.; Bajt, S.; Neussle, P.; Shea-McCarthy, G. *Environ. Sci. Technol.* **1998**, **32**, 1092−1098.
(198) Tokunaga, T. K.; Pickering, I. J.; Brown, J., Gordon E. *Soil Sci. Soc. Am. J.* **1996**, *60*, 781−790.
(199) Pickering, I. J.; Brown, J., G.E.; Tokunaga, T. K. *Environ. Sci. Technol.* **1995**, *29*, 2456−2459.
(200) Hunter, D. B.; Bertsch, P. M.; Kemner, K. M.; Clark, S. B. *J. Phys. IV Fr.* **1997**, *7*, C2-767−C2-771.
(201) Newman, A. *Anal. Chem. News & Features* **1996**, *68*, 255A.

(202) Holman, H.-Y.; Perry, D. L.; Martin, M. C.; Lamble, G. M.; McKinney, W. R.; Hunter-Cevera, J. *Geomicrobiol. J.* **1999**, *16*, 307−324.

(203) Niemeyer, J.; Thieme, J.; Guttman, P.; Wilhein, T.; Rudolph, D.; Schmahl, G. *Prog. Colloid Polym Sci.* **1994**, *95*, 139−142.

(204) Myneni, S. C. B.; Brown, J. T.; Martinez, G. A.; Meyer-Ilse, W. *Science* **1999**, *286*.

(205) Jacobsen, C.; Neuhausler, U. In *Synchrotron X-ray Methods in Clay Science*; Schulze, D. G., J. W. S., Bertsch, P. M., Eds.; The Clay Minerals Society: Boulder, CO, 1999; Vol. 9.

(206) Niemeyer, J.; Thieme, J. In *Synchrotron X-ray Methods in Clay Science*; Schulze, D. G., J. W. S., Bertsch, P. M., Eds.; The Clay Minerals Society: Boulder, CO, 1999; Vol. 9.

(207) Rothe, J.; Kneedler, E. M.; Pecher, K. H.; Tonner, B. P.; Nealson, K. H.; Grundl, T.; Meyer-lise, W.; Warwick, T. *J. Synchrotron Radiat.* **1999**, *6*, 359−361.

(208) Myneni, S. C. B.; Tokunaga, T. K.; Brown, G. E., Jr. *Science* **1997**, *278*, 1106−1109.

(209) Bockman, R. S.; Repo, M. A.; Warrell R.P., J.; Pounds, J. G.; Schidlovsky, G.; Gordon, B. M.; Jones, K. W. *Proc. Natl. Acad. Sci.* **1990**, **87**, 4149−4153.

(210) Rothman, S.; Anderson, E.; Attwood, D.; Batson, P.; Buckley, C.; Goncz, K.; Howells, M.; Jacobsen, C.; Kern, D.; Kirz, J.; Rarback, H.; Rivers, M.; Shu, D.; Tackaberry, R.; Turek, S. *Phys. Scr.* **1990**, *T31*, 18−22.

(211) van Langevelde, F.; Vis, R. D. *Anal. Chem.* **1991**, *63*, 2253−2259.

(212) Buckley, C. J.; Foster, G. F.; Burge, R. E.; Ali, S. Y.; Scotchford, C. A.; Kirz, J.; Rivers, M. L. *Rev. Sci. Instrum.* **1992**, *63*, 588−590.

(213) Gomez, S.; Rizzo, R.; Pozzi-Mucelli, M.; Bonucci, E.; Vittur, F. *Bone* **1999**, *25*, 33−38.

(214) Anderson, P.; Dowker, S. E. P.; Elliott, J. C.; Thomas, C. R. *Trace Microprobe Tech.* **1996**, *14*, 541−560.

(215) Carvalho, M. L.; Pinheiro, T.; Barreiros, M. A.; Casaca, C.; Cunha, A. S.; Chevallier, P. *Nucl. Instrum. Methods Phys. Res.* **1998**, *B138*, 913−918.

(216) Pinheiro, T.; Carvalho, M. L.; Casaca, C.; Barreiros, M. A.; Cunha, A. S.; Chevallier, P. *Nucl. Instrum. Methods Phys. Res. B* **1999**, *158*, 393−398.

(217) Iida, A.; Noma, T. *Nucl. Instrum. Methods Phys. Res.* **1993**, *B82*, 129−138.

(218) Shimojo, N.; Matsuzaki, I.; Homma-Takeda, S.; Tabata, K.; Shinyashiki, M.; Sun, G. G.; Iida, A.; Kumagai, Y. *J. Occup. Health* **1997**, 39, 64−65.

(219) Takeda-Homma, S.; Sasaki, A.; Nakai, I.; Sagai, M.; Koiso, K.; Shimojo, N. *J. Trace Elem. Exp. Me*d. **1993**, 6.

(220) Takeda-Homma, S.; Nakai, I.; S., M.; N., S. *Nucl. Instrum. Methods B* **1995**, *103*, 229−232.

(221) Takeda-Homma, S.; Kumagal, Y.; Shinyashiki, M.; Shimojo, N. *J. Synchrotron Radiat.* **1998**, *5*, 57−59.

(222) Mori, H.; Chujo, M.; Haruyama, S.; Skamoto, H.; Shinozaki, Y.; Uddin-Mohammed, M.; Iida, A.; Nakazawa, H. *Circulation Res.* **1995**, *76*, 1088−1100.

(223) Illman, B. L.; Bajt, S. *Int. Biodeterior. Biodegrad.* **1997**, *39*, 235−243.

(224) Fukumoto, N.; Kobayashi, Y.; Kurahashi, M.; Kojima, I. *Spectrochim. Acta* **1999**, *54B*, 91−98.

(225) Berglund, A.; Brelid, H.; Rindby, A.; Engstrom, P. *Holzforschyng* **1999**, 53, 474−480.

(226) Williams, S.; Jacobsen, C.; Kirtz, J.; Zhang, X.; T'hof, J. V.; Lamm, S. *Soft X-ray Microsc.* **1992**, *1741*, 318−324.

(227) De Stasio, G. D. *J. Phys. IV* **1994**, *4*, C9-287−C9292.

(228) De Stasio, G.; Mercanti, D.; Ciotti, M. T.; Droubay, T. C.; Perfetti, P.; Margaritondo, G.; Tonner, B. P. *Europhys. Lett.* **1994**, *28*, 283−287.

(229) Zhang, X.; Ade, H.; Jacobsen, C.; Kirz, J.; Lindaas, S.; Williams, S.; Wirick, S. In *Nuclear Instruments & Methods in Physics Research*; Elsevier Science B.V.: North Holland, 1994; Vol. A, p 347.

(230) Buckley, C. J. *Rev. Sci. Instrum.* **1995**, 66, 1318−1321.

(231) Hirai, M.; Takizawa, T.; Yabuki, S.; Nakata, Y.; Mitomo, H.; Hirai, T.; Shimizu, S.; Furusaka, M.; Kobayashi, K.; Hayashi, K. *Physica B* **1995**, *213/214*, 751−753.

(232) Buckley, C. J.; Bellamy, S. J.; Zhang, X.; Dermody, G.; Hulbert, S. *Rev. Sci. Instrum.* **1995**, *66*, 1322−1324.

(233) Jacobsen, C.; Chapman, H. N.; Fu, J.; Kalinovsky, A.; Kirz, J.; Maser, J.; Osanna, A.; Spector, S.; Tennant, D.; Wang, S.; Wirick, S.; Zhang, X. *J. Electron Spectrosc. Relat. Phenom.* **1996**, *80*, 337−341.

(234) De Stasio, G.; Mercanti, D.; Clotti, M. T.; Droubay, T. C.; Perfetti, P.; Margaritonda, G.; Tonner, B. P. *J. Appl. Phys.* **1996**, 259−262.

(235) Zhang, X.; Balhorn, R.; Mazrimas, J.; Kirz, J. *J. Struct. Biol.* **1996**, *116*, 335−344.

(236) De Stasio, G.; Margaritondo, G. *J. Electron Spectrosc. Relat. Phenom.* **1997**, *84*, 137−147.

(237) Margaritondo, G.; De Stasio, G. *Int. J. Imaging Syst. Technol.* **1997**, *8* (2), 188−203.

(238) Ito, A.; Shinohara, K.; Mizukami, Y.; Nakano, H.; Yada, K.; Uehara, T.; Honda, T. *J. Synchrotron Radiat.* **1998**, *5*, 1099−1101.

(239) Gilbert, B.; Redondo, J.; Baudat, P.-A.; Lorusso, G. F.; Andres, R.; Van Meir, E. G.; Brunet, J. F.; Hamou, M. F.; Suda, T.; Mercanti, D.; Clotti, M. T.; Droubay, T. C.; Tonner, B. P.; Perfetti, P.; Margaritondo, M.; De Stasio, G. *J. Phys. D: Appl. Phys.* **1998**, *31*, 2642−2647.

(240) Buleon, A.; Gerard, C.; Riekel, C.; Vuong, R.; Chanzy, H. *Macromolecules* **1998**, *31*, 6605−6610.

(241) Larabell, C. A.; Yager, D.; Meyer-Ilse VI International Conference on X-Ray Microscopy, Berkeley, CA, 1999; pp 107−112.

(242) Abraham-Peskir, J. V.; Chantler, E.; Guttmann, P.; Hjort, T.; Medenwaldt, R.; McCann, C.; Uggerhoj, E.; Vorup-Jensen, T. VI International Conference on X-Ray Microscopy, Berkeley, CA, 1999; pp 113−118.

(243) Ford, T. W.; Meyer-Ilse, W.; Stead, A. D. VI International Conference on X-Ray Microscopy, Berkeley, CA, 1999; pp 119−122.

(244) Weib, D.; Schneider, G.; Niemann, B.; Guttman, P.; Rudolph, D.; Schmahl, G. VI International Conference on X-Ray Microscopy, Berkeley, CA, 1999; pp 123−128.

(245) Kiyozuka, Y.; Takemoto, K.; Yamamoto, A.; Guttmann, P.; Tsubura, A.; Kihara, H. VI International Conference on X-Ray Microscopy, Berkeley, CA, 1999; pp 153−162.

(246) Stead, A. D.; Ford, T. W.; Page, A. M.; Majima, T.; Shimizu, H.; Tomie, T. VI International Conference on X-Ray Microscopy, Berkeley, CA, 1999; pp 163−167.

(247) Moronne, M. M.; Hamamoto, D. J.; Meigs, G.; Johnson, L. E.; Denbeaux, G. P.; Meyer-Ilse, W. VI International Conference on X-Ray Microscopy, Berkeley, CA, 1999; pp 184−189.

(248) Gilbert, B.; Neumann, M.; Steen, S.; Gabel, D.; Andres, R.; Perfetti, P.; Margaritondo, G.; De Stasio, G. VI International conference on X-Ray Microscopy, Berkeley, CA, 1999; pp 190−194.

(249) Cody, G. D. VI International Conference on X-Ray Microscopy, Berkeley, CA, 1999; pp 307−313.

(250) Salome, M.; Lafage-Proust, M. H.; Vico, L.; Amblard, D.; Kaulich, B.; Oestreich, S.; Susini, J.; Barrett, R. VI International Conference on X-Ray Microscopy, Berkeley, CA, 1999; pp 178−183.

(251) McHugo, S. A.; Thompson, A. C.; Flink, C.; Weber, E. R.; Lamble, G.; Gunion, B.; MacDowell, A.; Celestre, R.; Padmore, H. A.; Hussain, Z. *J. Cryst. Growth* **2000**, *210*, 395−400.

(252) Brennan, S.; Tompkins, W.; Takaura, N.; Pianetta, P.; Laderman, S.; Fischer-Colbrie, A.; J.B. Kortright; Madden, M. C.; Wherry, D. C. In *Nuclear Instruments & Methods in Physics Research*; North Holland, 1994; Vol. A.

(253) Noma, T.; A., I. *Rev. Sci. Instrum.* **1994**, *65*, 837−844.

(254) Noma, T.; Takada, K.; Iida, A. X-Ray *Spectrom.* **1999**, *28*, 433−439.

(255) Conner, W. C.; Webb, S. W.; Spanne, P.; Jones, K. W. *Macromolecules* **1990**, *23*, 4742−4747.

(256) Isaacs, H. S.; Cho, J. H.; Rivers, M. L.; Sutton, S. R. *J. Electrochem. Soc.* **1995**, *142*, 1111−1118.

(257) Kawasaki, K.; Iwasaki, H. *J. Synchrotron Radiat.* **1995**, *2*, 49−55.

(258) Hayakawa, S.; Jia, X.-P.; Wakatsuki, M.; Gohshi, Y.; Hirokawa, T. *J. Cryst. Growth* **2000**, *210*, 388−394.

(259) von Bohlen, A.; Klockenkamper, R.; Garbe, S.; Gaul, G.; Knochel, A.; Lechtenberg, F.; Palmetshofer, L. *Spectrochim. Acta* **1995**, *50B*, 1769−1777.

(260) Hwu, Y.; Cheng, N. F.; Lee, S. D.; Tung, C. Y. *Appl. Phys. Lett.* **1996**, *69*, 2924−2926.

(261) Kagoshima, Y.; Miyahara, T.; Ando, M.; Wang, J.; Aoki, S. *J. Appl. Phys.* **1996**, *80*, 3124−3126.

(262) Rossberg, A.; Piechotka, M.; Wetzel, G.; Gastaldi, J.; Magerl, A.; Kaldis, E. *J. Cryst. Growth* **1996**, *166*, 354−360.

(263) Besenbacher, F.; Chorkendorff, I.; Clausen, B. S.; Hammer, B.; Molenbroek, A. M.; Norskov, J. K.; Stensgaard, I. *Science* **1998**, *279*, 1913−1915.

(264) Nelson, A. J.; Gregoratti, L.; Chagarov, E.; Lonza, D.; Marsi, M.; Kiskinova, M. *J. Electron Spectrosc. Relat. Phenom.* **1999**, *105*, 51−61.

(265) Kinoshita, A.; Hirai, M.; Kusaka, M.; Iwami, M. *J. Appl. Phys.* **1999**, 38, 6544−6548.

(266) Neuhausler, U.; Abend, S.; Jacobsen, C.; Lagaly, G. *Colloid Polym. Sci.* **1999**, *277*, 719−726.

(267) Schmidt, T.; Ressel, B.; Huen, S.; Prince, K. C.; Bauer, E. VI International Conference on X-Ray Microscopy, Berkeley, CA, 1999; pp 27−32.

(268) Fischer, P.; Eimuller, T.; Schutz, G.; Guttmann, P.; Schmahl, G.; Bayreuther, G. VI International Conference on X-Ray Microscopy, Berkeley, CA, 1999; pp 205−212.

(269) Gunther, S.; Esch, F.; Gregoratti, L.; Marsi, M.; Kiskinova, M.; Schubert, U. A.; Grotz, P.; Knozinger, H.; Taglauer, E.; Schutz, E.; Schaak, A.; Imbihl, R. VI International Conference on X-Ray Microscopy, Berkeley, CA, 1999; pp 219−224.

(270) Drakopoulous, M.; Snigireva, I.; Snigirev, A.; Castelnau, O.; Chauveau, T.; Bacroix, B.; Schroer, C.; Ungar, T. VI International conference on X-Ray Microscopy, Berkeley, CA, 1999; pp 263−268.
(271) Chang, C.-H.; Valek, B. C.; Padmore, H. A.; MacDowell, A. A.; Celestre, R.; Marieb, T.; Bravman, J. C.; Koo, Y. M.; Patel, J. R. VI International Conference on X-Ray Microscopy, Berkeley, CA, 1999; pp 284−285.
(272) Zhang, X.; Jacobsen, C.; Lindaas, S.; Willimas, S. *J. Vac. Sci. Technol.* **1995**, 1477−1483.
(273) Ade, H.; Smith, A. P.; Cameron, S.; Cieslinski, R.; Mitchell, G.; Hsiao, B.; Rightor, E. *Polymer* **1995**, *36*, 1843−1848.
(274) Urquhart, S. G.; Hitchcock, A. P.; Smith, A. P.; Ade, H.; Rightor, E. G. *J. Phys. Chem. B* **1997**, *101*, 2267−2276.
(275) Smith, A. P.; Laurer, J. H.; Ade, H. W.; Smith, S. D.; Ashraf, A.; Spontak, R. J. *Macromolecules* **1997**, *30*, 663−666.
(276) Ade, H.; Smith, A. P.; Zhang, H.; Zhuang, G. R.; Kirz, J.; Rightor, E.; Hitchcock, A. *J. Electron Spectrosc. Relat. Phenom.* **1997**, *84*, 53−72.
(277) Ade, H. TRIP **1997**, 5, 58−66.
(278) Ade, H.; Winesett, D. A.; Smith, A. P. *Appl. Phys. Lett.* **1998**, *73*, 3775−3777.
(279) Okajima, T.; Teramoto, K.; Mitsumoto, R.; Oji, H.; Yamamoto, Y.; Mori, I.; Ishii, H.; Ouchi, Y.; Seki, K. *J. Phys. Chem. A* **1998**, *102*, 7093−7099.
(280) Smith, A. P.; Bai, C.; Ade, A.; Spontak, R. J.; Balik, C. M.; Koch, C. C. *Macromol. Rapid Commun.* **1998**, *19*, 557−561.
(281) Slep, D.; Asselta, J.; Rafailovich, M. H.; Sokolov, J.; Winesett, D. A.; Smith, A. P.; Ade, H.; Strzhemechny, Y.; Schwarz, S. A.; Sauer, B. B. *Langmuir* **1998**, *14*, 4860−4864.
(282) Kikuma, J.; Warwick, T.; Shin, H.-J.; Zhang, J.; Tonner, B. P. *J. Electron Spectrosc. Relat. Phenom.* **1998**, *94*.
(283) Ade, H.; Winesett, D. A.; Smith, A. P.; Qu, S.; Ge, S.; Sokolov, J.; Rafailovich, M. *Europhys. Lett.* **1999**, *45*, 526−532.
(284) Urquhart, S. G.; Hitchcock, A. P.; Smith, A. P.; Ade, H. W.; Lidy, W.; Rightor, E. G.; Mitchell, G. E. *J. Electron Spectrosc.* **1999**, *100*, 119−135.
(285) Giebler, R.; Schulz, B.; Reiche, J.; Brehmer, L.; Wuhn, M.; Woll, C.; Smith, A. P.; Urquhart, S. G.; Ade, H. W.; Unger, W. E. S. *Langmuir* **1999**, *15*, 1291−1298.
(286) Urquhart, S. G.; Smith, A. P.; Ade, H. W.; Hitchcock, A. P. *J. Phys. Chem. B* **1999**, *103*, 4603−4610.
(287) Zhu, S.; Liu, Y.; Rafailovich, M. H.; Sokolov, J.; Gersappe, D.; Winesett, D. A.; Ade, H. *Nature* **1999**, *400*, 49−51.
(288) Smith, A. P.; Ade, H.; Balik, C. M.; Koch, C. C.; Smith, S. D.; Spontak, R. J. *Macromolecules* **2000**, *33*, 2595−2604.
(289) Smith, A. P.; Spontak, R. J.; Koch, C. C.; Ade, H. Vi International Conference on X-Ray Microscopy, Berkeley, CA, 1999; pp 60−65.
(290) Ade, H. VI International Conference on X-Ray Microscopy, Berkeley, CA, 1999; pp 197−204.
(291) Hitchcock, A. P.; Tyliszczak, T.; Koprinarov, I.; Stover, H.; Li, W. H.; Heng, Y. M.; Murti, K.; Gerroir, P.; Dutcher, J. R.; Dalnoki-Veress, K.; Ade, H. W. VI International Conference on X-Ray Microscopy, Berkeley, CA, 1999; pp 231−234.
(292) Hitchcock, A. P.; Tyliszczak, T.; Heng, Y. M.; Cornelius, R.; Brash, J. L.; Ade, H.; Anders, S.; Scholl, A.; Nolting, F. VI International conference on X-Ray Microscopy, Berkeley, CA, 1999; pp 235−238.
(293) Schmitt, T.; Guttmann, P.; Schmidt, O.; Muller-Buschbaum, P.; Stamm, M.; Schonhense, G.; Schmahl, G. VI International Conference on X-Ray Microscopy, Berkeley, CA, 1999; pp 245−249.
(294) Winsett, D. A.; Gersappe, D.; Rafailovich, M.; Sokolov, J.; Zhu, S.; Ade, H. VI International Conference on X-Ray Microscopy, Berkeley, CA, 1999; pp 275−278.
(295) Rightor, E. G.; Hitchcock, A. P.; Ade, H.; Leapman, R. D.; Urquhart, S. G.; Smith, A. P.; Mitchell, G.; Fischer, D.; Shin, H. J.; Warwick, T. *J. Phys. Chem. B* **1997**, *101*, 1950−1960.
(296) Anderson, P.; Elliot, J. C.; Thomas, C. R.; Van Langevelde, F. *X-Ray Spectrom.* **1993**, *22*, 265−271.
(297) Zappala, A.; Bajt, S.; Gigante, G. E.; Hanson, A. L. *Nucl. Instrum. Methods Phys. Res. B* **1996**, *117*, 145−150.
(298) Capasso, L.; Tota, G. D.; Jones, K. W.; Tuniz, C. *Int. J. Osteoarchaeol.* **1995**, *5*, 282−288.
(299) Janssens, K.; Aerts, A.; Vincze, L.; Adams, F.; Yang, C.; Utui, R.; Malmqvist, K.; Jones, K. W.; Radtke, M.; Garbe, S.; Lechtenberg, F.; Knochel, A.; Wouters, H. *Nucl. Instrum. Methods Phys. Res. B* **1996**, *109/110*, 690−695.
(300) Janssens, K.; Vincze, L.; Vekemans, B.; Williams, C. T.; Radtke, M.; Haller, M.; Knochel, A. *Fresenius J. Anal. Chem.* **1999**, *363*, 413−420.
(301) Janssens, K.; Vittiglio, G.; Deraedt, I.; Aerts, A.; Vekemans, B.; Vincze, L.; Wei, F.; Deryck, I.; Schalm, O.; Adams, F.; Rindby, A.; Knochel, A.; Simionovici, B.; Snigriev, A. *X-Ray Spectrom.* **1999**, *29*, 73−91.
(302) Simionovici, A.; Janssens, K.; Rindby, A.; Snigireva, I.; Snigirev, A. *VI* International Conference on X-ray Microscopy; Berkeley, CA, 1999; pp 279−283.
(303) Elmer, J. W.; Wong, J.; Froba, M.; Waide, P. A.; Larson, E. M. *Metall. Mater. Trans.* **1996**, *27A*, 775−783.
(304) Rindby, A.; Engstrom, P.; Janssens, K. *J. Synchrotron Radiat.* **1997**, *4*, 228−235.
(305) Wenk, H. R.; Heidelbach, F.; Chateigner, D.; Zontone, F. *J. Synchrotron Radiat.* **1997**, *4*, 95−101.
(306) Ungar, T.; Langford, J. I.; Cernik, R. J.; Voros, G.; Pflaumer, R.; Oszlanyi, G.; Kovacs, I. *Mater. Sci. Eng.* **1997**, 81−87.
(307) Guvenilir, A.; Butler, G. C.; J.D., H.; McDowell, D. L.; Stock, S. R. *Acta Metall. Inc.* **1998**, *46*, 6599−6604.
(308) Chevallier, P.; Firsov, A.; P., P.; F., L. *J. Phys. IV Fr.* **1998**, *8*, 407−412.
(309) Rindby, A.; Voglis, P.; Engstrom, P. *Biomaterials* **1998**, *19*, 2083−2090.
(310) Dillman, P.; Regad, B.; Moulin, G. *J. Mater. Sci. Lett.* **2000**, *19*, 907−910.
(311) Kinney, J. H.; Haupt, D. L.; Nichols, M. C.; Breunig, T. M.; Jr., G. W. M.; Marshall, S. J. In *Nuclear Instruments & Methods in Physics Research*; Elsevier, North Holland, 1994; Vol. A.
(312) Renevier, H.; Hodeau, J. L.; Dalakas, V.; Wolfers, P.; Berar, J. F.; Andrieu, S.; Weigelt, J.; Frahm, R. *Phys. IV Fr.* **1997**, C2-741−C2-743.

CR990070S